University of Cyprus

Department of Mechanical and Manufacturing Engineering

Organic-inorganic hybrid materials combining metal nanoparticles and functional amphiphilic diblock copolymers. Synthesis, characterization and experimental investigation of their nonlinear optical properties.

by

Maria Demetriou

A dissertation submitted in partial fulfillment of the requirements for the degree of Doctor of Philosophy in Mechanical and Manufacturing Engineering

October 2011

Maria Demetriou

Organic-inorganic hybrid materials combining metal nanoparticles and functional amphiphilic diblock copolymers. Synthesis, characterization and experimental investigation of their nonlinear optical properties.

This Ph.D. Thesis has been carried out in partial fulfillment of the requirements for the degree of Doctor of Philosophy at the Department of Mechanical and Manufacturing Engineering and approved on the 27th of October 2011 by the Doctoral Committee.

Doctoral Committee

Research Advisor: Theodora Krasia-Christoforou ……..

Other Members:

George Fytas

Andreas Othonos

Andreas Kyprianou

Matthew Zervos

Dedicated with love to my father & mother.....

CONTENTS

ABSTRACT

The present work mainly focuses on the synthesis and characterization together with the experimental investigation of the non linear optical (NLO) properties of novel organic-inorganic hybrid materials based on functional amphiphilic block copolymers and palladium nanoparticles. More precisely, three families of novel, well-defined block copolymers were synthesized employing Reversible Addition-Fragmentation Chain-Transfer (RAFT) controlled radical polymerization, in which the ligating block segment (2-acetoacetoxy ethyl methacrylate (AEMA)), capable of binding and stabilizing inorganic metal ions and metal nanoparticles in selective organic media, remained unchanged in terms of chemical structure. Therefore, the differentiation of the three families has been provided by changing the chemical nature of the second block segment. In the first family, a long-alkyl chain monomer (Lauryl methacrylate (LauMA)) has been used. In the second family, a photoconductive monomer (2-(N-carbazolyl) ethyl ethacrylate (CbzEMA)) was introduced in the second block. Finally, in the third family, a fluorescent monomer (9-anthrylmethyl methacrylate (AnMMA)) was incorporated. All polymers were characterized by Size Exclusion Chromatography (SEC) and ^{1}H NMR (molecular characterization), Differential Scanning Calorimetry (DSC) and Thermal Gravimetric Analysis (TGA) (thermal characterization) and Dynamic Light Scattering (DLS) (self-assembly behavior). For the first time, micellar nanostructures constructed by the above-mentioned functional block copolymers were used as a nano-environment for the complexation and solubilization of palladium salts and palladium nanoparticles in organic media towards the fabrication of organic-inorganic hybrid materials. The hybrid systems were characterized by UV-vis (demonstration of the successful formation of the polymer-metal ion complex before reduction, as well as the transformation of Pd(II) to Pd(^{0}) after reduction), DLS, Atomic Force Microscopy (AFM) and Transmission Electron Microscopy (TEM) (determination of the hydrodynamic sizes and the morphology). The Z-scan technique was then employed for the measurement of the NLO absorption and refraction of the hybrid systems as well as the determination of the third-order nonlinear susceptibility $\chi^{(3)}$. Furthermore, the effect of different parameters characterizing the hybrid systems (e.g. the size of the macromolecular aggregates, the chemical structure and molecular characteristics of the block copolymers) on the NLO response is discussed.

Moreover, the anthracene-containing polymers were evaluated toward their ability to act as effective dual chemosensors (i.e. amino- and metal ion sensors) in organic media. More precisely, the fluorescence intensity of both, the AnMMA$_x$ homopolymers and the AnMMA$_x$-*b*-AEMA$_y$ diblock copolymers in solution exhibited a significant decrease in the presence of triethylamine. Moreover, the presence of iron (III) cations were also found to significantly affect the fluorescence signal of the anthracene moieties when those were combined in a block copolymer structure with the AEMA units, due to complex formation occuring between the *β*-ketoester groups of the AEMA$_x$ segment and the cations.

The LauMA$_x$-*b*-AEMA$_y$ block copolymers were also used for the encapsulation of Au nanoparticles. The resulting micellar nonohybrids were characterized by UV-*vis*. In an effort to demonstrate the potential applicability of these hybrid polymer-based nanosystems in the nanowire technologies, the LauMA$_x$-*b*-AEMA$_y$/Pd(^{0}) and LauMA$_x$-*b*-AEMA$_y$/Au micellar nanohybrids were employed as nanocatalysts for the growth of semiconducting metal oxide nanowires.

ΠΕΡΙΛΗΨΗ

Η παρούσα εργασία στοχεύει κυρίως στη σύνθεση, στο χαρακτηρισμό και στην πειραματική μελέτη των μη-γραμμικών οπτικών ιδιοτήτων καινοτόμων οργανικών-ανόργανων υβριδικών υλικών βασισμένων σε λειτουργικά αδρομερή συμπολυμερή και νανοσωματίδια παλλαδίου. Συγκεκριμένα, τρεις οικογένειες καινούργιων αδρομερών συμπολυμερών έχουν παρασκευαστεί, με χρήση της μεθόδου πολυμερισμού αντιστρεπτής προσθήκης απόσπασης με μεταφορά αλυσίδας (Reversible Addition-Fragmentation Chain Transfer, RAFT). Το ένα τμήμα των αδρομερών συμπολυμερών παραμένει σταθερό όσο αφορά τη χημική δομή και αποτελείται από μονάδες 2-acetoacetoxy ethyl methacrylate (AEMA), οι οποίες έχουν την ικανότητα να δεσμεύουν και να σταθεροποιούν ανόργανα μεταλλοϊόντα και μεταλλικά νανοσωματίδια σε εκλεκτικούς οργανικούς διαλύτες εξαιτίας της παρουσίας ομάδων *β*-κετοεστέρα στις δομές τους. Συνεπώς, η διαφοροποίηση μεταξύ των τριών οικογενειών έγκειται στην αλλαγή της χημικής φύσης του δεύτερου τμήματος του πολυμερούς. Το Lauryl methacrylate (LauMA), ένα μονομερές που φέρει μακριά, υδρόφοβη υδρογονανθρακική αλυσίδα χρησιμοποιήθηκε για τη σύνθεση της πρώτης οικογένειας πολυμερών. Για την δεύτερη οικογένεια, ένα φωτοαγώγιμο μονομερές ((N-carbazolyl) ethyl ethacrylate (CbzEMA)), εισήχθη ως δεύτερο τμήμα και τέλος για την τρίτη οικογένεια ένα φθορίζον μονομερές (9-anthrylmethyl methacrylate (AnMMA)) ενσωματώθηκε. Όλα τα πολυμερή έχουν χαρακτηριστεί με διάφορες τεχνικές συμπεριλαμβανομένων της χρωματογραφίας αποκλεισμού μεγέθους (SEC) και φασματοσκοπίας πυρηνικού μαγνητικού συντονισμού (^{1}H NMR) για το μοριακό χαρακτηρισμός, τη διαφορική θερμιδομετρία σάρωσης (DSC) και θερμοβαρυμετρική ανάλυσης (TGA) για το θερμικό χαρακτηρισμό, καθώς και τη δυναμική σκέδαση φωτός (DLS) για τη μελέτη της συμπεριφοράς συσσωμάτωσης. Για πρώτη φορά μικύλια βασισμένα στα προαναφερθέντα λειτουργικά αδρομερή συμπολυμερή έχουν χρησιμοποιηθεί ως νανο-συστήματα για τη συμπλοκοποίηση και τη διαλυτοποίηση αλάτων παλλαδίου και νανοσωματιδίων παλλαδίου σε οργανικό μέσο με απώτερο στόχο τη παρασκευή οργανικών-ανόργανων υβριδικών υλικών. Τα υβριδικά συστήματα έχουν χαρακτηρισθεί με τις εξής μεθόδους: φασματοσκοπία υπεριώδους-ορατού (UV-*vis*) για επιβεβαίωση του σχηματισμού του συμπλόκου πουλυμερούς-μεταλλοϊόντος καθώς και της μετατροπής των Pd(II) σε Pd(^{0}), DLS, μικροσκοπία ατομικής δύναμης (AFM) και ηλεκτρονική μικροσκοπία διέλευσης (TEM) για το προσδιορισμό των υδροδυναμικών διαμέτρων των μικυλίων καθώς και των μεγεθών των μεταλλικών νανοσωματιδίων). Η τεχνική Z-scan έχει χρησιμοποιηθεί για τη μέτρηση της μη-γραμμικής απορρόφησης και διάθλασης των υβριδικών συστημάτων, καθώς και για τον προσδιορισμό της μη-γραμμικής τους επιδεκτικότητας τρίτης τάξης.

Επιπλέον, τα πολυμερή βασισμένα σε ανθρακένιο έχουν αξιολογηθεί ως προς την ικανότητα τους να δρουν ως διπλοί χημικοί αισθητήρες (αισθητήρες αμινών και μεταλλοϊόντων) σε οργανικό μέσο. Πιο

συγκεκριμένα, η ένταση φθορισμού των $AnMMA_x$ ομοπολυμερών καθώς και των $AEMA_x$-*b*-$AnMMA_y$ αδρομερών συμπολυμερών παρουσιάζει σημαντική μείωση στην παρουσία τριαιθυλαμίνης. Επίσης η παρουσία ιόντων σιδήρου επηρεάζει αισθητά το φθορισμό των ομάδων ανθρακενίου όταν αυτές συνδυαστούν με μονάδες *β*-κετοεστέρα σε αδρομερή συμπολυμερή του τύπου $AEMA_x$-*b*-$AnMMA_y$.

Τα αδρομερή συμπολυμερή $LauMA_x$-*b*-$AEMA_y$ έχουν χρησιμοποιηθεί και για τη σταθεροποίηση νανοσωματιδίων Au. Τα νανοϋβριδικά μικύλια έχουν χαρακτηρισθεί με UV-*vis*, DLS και TEM. Σε μια προσπάθεια να αποδειχθεί η δυνατότητα εφαρμογής των συγκεκριμένων υβριδικών συστημάτων σε τεχνολογίες νανονημάτων, τα υβριδικά συστήματα $LauMA_x$-*b*-$AEMA_y$/$Pd(^0)$ και $LauMA_x$-*b*-$AEMA_y$/Au έχουν χρησιμοποιηθεί ως νανοκαταλύτες για την ανάπτυξη ημιαγώγιμων νανονημάτων από μεταλλικά οξείδια.

ACKNOWLEDGEMENTS

It is hard to overstate my gratitude to my PhD supervisor, Dr. Theodora Krasia-Christoforou. Without her inspirational guidance, enthusiasm, encouragement, unselfish help and limitless patience, I could never finish my doctoral work. For me, she is not only an advisor, but also a lifetime friend. She is the one who motivated me to further continue my post-graduate studies and she has been there every step in the way.
She has supported me in a number of ways during the experimental work and the hard writing-up period.

During my time as a PhD student, I have been lucky enough to have been surrounded by wonderful colleagues. Firstly I would like to thank the past and current members of my lab group, for the impeccable collaboration both inside and outside of the campus surroundings. It has been a pleasure to meet them all and work alongside them.

There is also a special group of graduate students and very good friends; these are Maria Ioannou and Chrysi Papageorgiou, whom without their support and understanding I would not have made it.

Completing a PhD is not an individual work. It is based on the support and co-operation of colleagues not only from Cyprus but also from Greece. My colleagues in Patras, Prof. S. Couris and his group have contributed enormously in the process of this dissertation since the experiments concerning the non linear response of the polymer-based nanohybrids were carried out in their laboratories. I would like to especially thank Prof. S. Couris for the enlightening discussions we had on the field of non linear optics.

This thesis would not have been possible without the contribution of these people:

Prof. Costas Patrickios for providing access to the DLS and DSC apparatus as well as, his research group, especially Maria Rikkou and Kyriaki Pafiti, for helping me during measurement difficulties (Department of Chemistry, University of Cyprus).

Prof. Panayiotis Koutentis (Department of Chemistry, University of Cyprus) and especially Sophie Michaelidou-Papadopoulou for their help with the TGA measurements.

Dr. Rodica Turcu (National Insitute R&D for Isotopic and Molecular Technologies, Cluj-Napoca, Romania) for the TEM measurements.

Dr. Matthew Zervos (Department of Mechanical and Manufacturing Engineering, University of Cyprus) for the nanowire growth and for all valuable discussions.

Prof. Andrea Othonos (Department of Physics, University of Cyprus) for the photoluminescence measurements.

Prof. Epaminondas Leontidis for providing access to the spectrofluorimeter.

I would also like to acknowledge the project ΤΕΧΝΟΛΟΓΙΑ/ΘΕΠΙΣ/0308(ΒΕ) of the Cyprus Research Promotion Foundation and the University of Cyprus for financial support.

Last but not least I would like to express my gratitude to my hard-working parents who have supported me both psychologically and financially. Without their unconditional love and continuous encouragement I would not manage to come this far. Furthermore, many thanks to my family members and especially my brother, my sister, my grandparents and my aunts Chryso and Spyroula who have been there for me whenever I needed them, always encouraging me. I want them to know how much I appreciate their patience and their understanding throughout these years. Finally, I would like to send a special "Thank you" to my lifelong friends, who have been there every step in the way, in all the bad and good times. Their friendship has been invaluable and appreciated tremendously. Maria Kleitou, Georgia Ioannou, Andri Rikkou and Katerina Pafiti are some of the friends who accompanied me in this amazing and unforgettable journey.

"If a man empties his purse into his head no one can take it away from him.
An investment in knowledge always pays the best interest."
Benjamin Franklin

Maria Demetriou
University of Cyprus
October 2010

LIST OF FIGURES

LIST OF TABLES

ABBREVIATIONS

NLO	Nonlinear optics
MNP	Metal nanoparticle
ABC	Amphiphilic block copolymer
Pd	Palladium
PEO	Poly(ethylene oxide)
CMC	Critical micellization concentration
DP	Degree of polymerization
χ_{AB}	Flory-Huggins interaction parameter
MW	Molecular weight
MWD	Molecular weight distribution
NMP	Nitroxide-mediated polymerization
ATRP	Atom transfer radical polymerization
RAFT	Reversible addition-fragmentation chain transfer
CTA	Chain transfer agent
CDTB	Cumyl dithiobenzoate
CPDB	2-cyano-2-propyl benzodithioate
AEMA	(2-acetoacetoxy) ethyl methacrylate
PS	Poly(styrene)
PMMA	Poly(methyl methacrylate)
P4VP	Poly(4-vinylpyridine)
NMR	Nuclear magnetic resonance
US	Ultrasound
PEGMA	Poly(ethylene glycol)methyl ether methacrylate
MRI	Magnetic resonance imaging
PEG	Poly(ethylene glycol)
PLA	Poly(D,L-lactide)
DOXO	doxorubicin
SPIO	Superparamagnetic iron oxide
Au	Gold
PLED	Polymer light-emitting diode

MDMO-PPV	poly-[2-(3,7-dimethyloctyloxy)-5-methyloxy]-para-phenylene-vinylene]
ZnO	Zinc oxide
PI	Poly(isoprene)
PAA	Poly(acrylic acid)
PtBuMA	Poly(tert-butyl methacrylate)
SEC	Size exclusion chromatography
V_e	Elution volume
$\overline{M}_n$	Number-average molecular weight
$\overline{M}_w$	Weight-average molecular weight
PDI	Polydispersity
DRI	Differential Refractometer
DLS	Dynamic Light Scattering
UV-*vis*	Ultraviolet-visible
HUMO	Highest occupied molecular orbital
LUMO	Lowest unoccupied molecular orbital
λ	Wavelength
DSC	Differential Scanning Calorimetry
T_g	Glass transition temperature
T_m	Melting temperature
TGA	Thermal gravimetric Analysis
AFM	Atomic Force Microscopy
SEM	Scanning Electron Microscopy
TEM	Transmission Electron Microscope
γ'	Nonlinear refractive index
β	Nonlinear absorption coefficient
$\chi^{(3)}$	Third-order susceptibility
$\mathrm{Im}\chi^{(3)}$	Imaginary part of third-order susceptibility
$\mathrm{Re}\chi^{(3)}$	Real part of third-order susceptibility
LauMA	Lauryl-methacrylate
NW	Nanowire
CbzEMA	2-(N-carbazolyl) ethyl methacrylate
AnMMA	9-anthrylmethyl methacrylate

THF	tetrahydrofurane
D_H	Hydrodynamic diameter
RSA	Reverse saturable absorption
BuMA	Butyl methacrylate

RESEARCH GOALS

The goal of this Ph.D thesis was to develop novel polymer-metal hybrid systems consisting of Pd MNPs and well-defined block copolymers bearing *β*-ketoester functionalities with potential applications in optoelectronic and photonic devices. The stabilization of the MNPs is succeeded by the complexation of palladium ions with the *β*-ketoester moieties of block copolymers followed by the reduction of the palladium ions to noble palladium. Polymer-mediated self-assembly of MNPs is a versatile route followed for the their preparation, which leads to advanced hybrid materials since it promotes the confinement of metallic compounds within well-defined nanostructured domains, providing control of their shape and size. The originality of the present thesis lies in the fact that it constitutes the first systematic work including the synthesis, characterization and experimental investigation of the optoelectronic behavior (i.e. NLO response) of such systems. Pd NPs have been only rarely investigated towards their NLO properties. Most of the reported work refers to gold and silver NPs embedded in organic matrices. To the best of our knowledge, there is no example appearing in the literature describing the NLO response of Pd NPs encapsulated in amphiphilic block copolymer micelles. Due to the flexibility of the synthetic methodology followed in the present thesis, block copolymers with different chemical compositions and block length have been prepared. By varying these two parameters, the size and the morphology effect of the micellar hybrids on the NLO properties was investigated. The chemical structure of the second block (LauMA/ CzEMA / AnMMA) is an important parameter which provides valuable information regarding the effect of the chemical composition of the polymeric component on the NLO behavior. Furthermore, for polymer preparation a controlled polymerization method was employed, allowed the correlation of the structural characteristics of the polymers and hence the hybrid materials to their properties.

Additionally, the hybrid systems based on lauryl-containing polymers and Pd(^{0}) or Au NPs was investigated towards their applicability as efficient nanostructured catalysts for the development of ultrathin semiconductor metal-oxide nanowires in which quantization effects may occur. As mentioned above, amphiphilic block copolymer micelles are considered a powerful tool for the formation of stabilized MNPs. The spatial confinement created by micelles provides a tremendous size control of the MNPs and prevent their coagulation. The

use of polymer-metal hybrids for the development of nanowires is limited, so in the present work the potential applicability of the aforementioned systems for the growth of free standing or template metal oxide NWs is exploited.

Polymeric materials possessing fluorescent moieties have attracted significant attention due to their potential applications such as fluorescent chemosensors and biosensors, fluorescent imaging agents, optical materials for organic light emitting devices and metal ion sensors, to mention only a few. A widely used fluorescent molecule known for its interesting photophysical properties is anthracene. Fluorescence quenching is an effective mechanism that can be employed for the identification of ions (both, cations and anions) as well as amines with lone electron pairs in solution. Polymer-based metal ion sensors have been reported by various groups, however, most of the developed systems are homopolymers characterized by a structural complexity and demanding synthetic methodologies towards their preparation. In the present thesis a simple and cost-effective synthetic approach involving a controlled radical polymerization process was employed towards this purpose. AnMMA with AEMA were combined in diblock copolymer architecture to yield well-defined functional diblock copolymers presenting fluorescent and metal chelating properties. In this work efficacy of these systems to act as effective dual chemosensors (i.e. amino- and metal ion sensors) in organic media is demonstrated.

1. INTRODUCTION

Over the past decades, polymer science has strongly been entering the field of organic-inorganic hybrid materials, aiming to combine the optimum properties of metal compounds and polymers [1], via the formation of nanostructured materials [2]. This combination may lead to new materials that could be potentially used in a wide range of applications such as catalysis [3], waste-water treatment [4], information storage [5], biomedicine [6], semiconductor technologies [7], nanolithography [8], optoelectronics [9] and so forth. Regarding the latter, it is strongly believed that in the future optoelectronic and photonic devices will consist of organic-inorganic hybrid nanomaterials exhibiting custom-made nonlinear optical (NLO) response. Materials with NLO properties exhibit great interest due to their potential use in technological applications such as all-optical switching, signal processing and fast optical communications [10].

A versatile route followed for the preparation of metal nanoparticles (MNPs), makes use of well-defined amphiphilic block copolymers (ABCs). ABCs are capable to self-assemble in selective organic or aqueous media creating well-organized nanomorphologies (micelles, vesicles etc.) in solution, as well as in the solid state due to microphase separation occurring between their immiscible block segments. Their ability to create various organized nanomorphologies makes them ideal templates for the localization of metals on the nanoscale [11]. The utilization of amphiphilic block copolymers characterized by predetermined molecular characteristics as a medium for the formation of MNPs not only promotes the confinement of metallic compounds within well-defined nanostructured domains, providing an improved stabilization and control of nanoparticle growth, but also imparts new properties to the resulting hybrid materials [12].

The formation of polymer-stabilized MNPs requires the presence of metal-coordination sites within the polymer structure that would enable the development of specific metal-ligand interactions between the polymer and the metal or metal ion [13]. Polymers with coordinating moieties (containing -O, -S and N-) have been extensively investigated due to their ability to form polymer-metal complexes with various metal ions [2]. Among them, well-defined block copolymers containing β-ketoester ligating functionalities which are capable of complexing and solubilizing metal ions of different geometries and oxidation states [14], have been

studied towards their ability to complex different metal ions such as Fe(III), Co(II), Cu(II) etc. in selective organic media yielding sterically stabilized colloidal hybrid nanomaterials [15].

The unique size-dependent properties and the high surface-to-volume ratios of MNPs have led to an increased interest for such materials in many scientific fields such as chemistry, physics and nanotechnology [16]. In particular, their electronic and optical properties are of great interest for several optoelectronic and photonic applications and devices. As a result, during the last years, there has been an intense scientific activity concerning the preparation and the detailed investigation of their electronic and optical properties, mainly focused on noble metals (e.g. gold or silver) [17,18,19], whereas it is only recently, that transition metal nanoparticles have attracted more attention [12]. Among them, Palladium (Pd) nanoparticles are very interesting as they are expected to combine their catalytic [20], hydrogen storage [21], sensing [22] and magnetic properties [23] with their NLO properties which are relatively unexplored yet [24,25,26].

In the following sub-chapters, a brief description on block copolymers and their aggregation behavior in solution and at the solid state is discussed. In 1.2 an overview description on controlled radical polymerization methodologies employed for the synthesis of well-defined polymeric materials is given. Moreover, sub-chapter 1.3 is devoted to MNPs in regards to their synthesis and stabilization mechanisms, whereas in sub-chapter 1.4 different applications of polymer-metal hybrids in various fields are discussed.

1.1 Amphiphilic Block Copolymers and Micellization

The term “polymer”, deriving from the greek word “πολυμερές” (having many parts), denotes synthetic or natural large molecules consisting of repeated chemical units. By virtue of their mechanical and thermal properties, of their easy processability and low cost, they find numerous applications in construction, automobile, biomedicine, nanotechnology etc. Due to the appearance of new technological challenges in the near future in all fields of science and technology, new technologies have been developed in the last decades and efforts from research groups have been made to develop new polymerization tools in order to obtain advanced polymeric structures and architectures.

A particular class of polymers is block copolymers consisting of at least two blocks of compositionally and/or configurationally different monomeric units [28], which are connected usually *via* covalent bonds [29,30]. Unlike other copolymers, they retain many of the physical characteristics of the two corresponding homopolymers [31]. Block copolymers can be synthesized following various synthetic methods such as anionic, cationic, group transfer and controlled radical polymerizations [13]. The latter are further described in 1.2. Classification of these materials is made according to the number of different blocks incorporated in their structures, i.e. di-, tri-, or multi-block copolymers [31,32,33].

An increased interest is observed in the synthesis and characterization of amphiphilic block copolymers. These systems, when dissolved in a solvent which is selective for one of the blocks, they tend to self-assemble forming various well-organized nanomorphologies [34, 35, 36], similar to low molecular weight surfactant molecules [37, 38].

The simplest kind of amphiphilic block copolymers is diblock copolymers [21, 35, 39]. In the bulk and in solution, they microphase separate into a number of different morphologies (on scales from 1nm to 100nm) [13, 33, 40]. Since the two covalently bound blocks are physically incompatible [21,41] and due to the interactions taking place between the different blocks [42,43,44], the system will undergo a microphase separation to form fascinating arrays of nanostructures and morphologies. The covalent bond existing between the two blocks in diblock copolymers plays the role of the interface in such a microphase-separated system, where the one segment resides in one phase and the other one is located in the adjacent phase [44]. The most common structures generated by diblock copolymers are shown in Figure 1.1.

The aggregation process is affected by a number of parameters such as: chemical composition [32], block lengths [45,46], temperature [35, 45,46], concentration [45], etc. Those assemblies are driven by thermodynamic considerations (e.g., minimization of the free energy [28,39]) and require minimal external input. Additionally, the self-assembly behavior of amphiphilic block copolymers depends on the Flory Huggins polymer/polymer and polymer/solvent interaction parameters [32]. Depending on the kind of monomers, the length of the different block segments, their number (i.e. di-, tri- multiblocks) as well as the polymer architecture, block copolymers can exhibit a wide range of different properties [13,30].

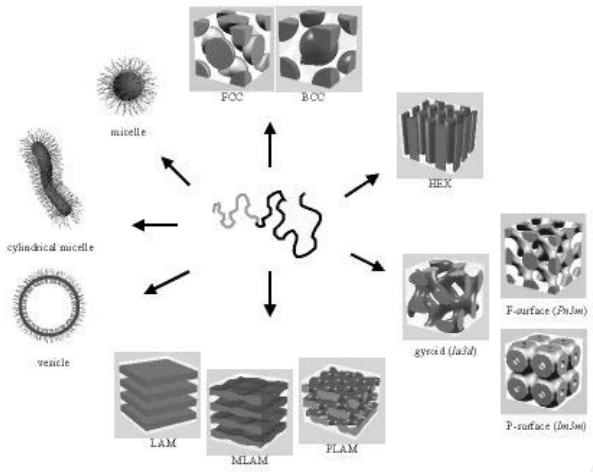

Figure 1.1: *Self-organized structures of block copolymers: spherical micelles, cylindrical micelles, vesicles (solution), fcc- and bcc-packed spheres (FCC, BCC), hexagonally packed cylinders (HEX), various minimal surfaces (gyroid, F surface, P surface), simple lamellae (LAM), as well as modulated and perforated lamellae (MLAM, PLAM) (solid state) [44].*

The micellization behavior of block copolymers in solution, both, aqueous and organic, has been investigated since the 1960´s [40,41,47]. In selective solvents, amphiphilic block copolymers tend to self-aggregate forming micellar nanomorphologies consisting of rather dense cores of the insoluble blocks, surrounded by solvated outer shells (coronas) of the soluble ones as depicted Figure 1.2.

Micellization in aqueous media can be considered as an entropy driven process [47]. Water is unique in terms of its properties as a solvent, which arise from a singular cohesive energy due to the strongest hydrogen binding network among polar solvents. Surface activity and tendency to self-assembly is displayed when a dissolved molecule presents an apolar moiety attached to polar (ionic or non-ionic), due its dual interaction with water. Considerably, the most common polar group found in aqueous block copolymer micelles is poly(ethylene oxide) (PEO), attached to a variety of apolar moieties. PEO is highly soluble in water, and its strong hydration is due to a very favourable fitting of the ethylene oxide monomer into the water structure [38]. The increasing interest in such systems is attributed to their widespread application possibilities in technical and especially biomedical areas [35,47].

The phenomenon of micellization of block copolymers in selective organic solvents (polar and non-polar) was extensively investigated and a great deal of experimental and theoretical work has been done, as outlined in different review papers [30,38,41,47]. Despite in aqueous systems, the formation of micelles in an organic solvent is mainly an enthalpy driven process [30,47].

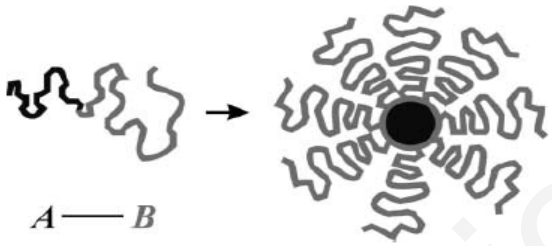

Figure 1.2: *Formation of an AB diblock copolymer micelle [44].*

Both, block copolymers and low MW surfactant molecules have the ability to form micelles in selective solvents. However, micellar structures deriving from amphiphilic block copolymers are thermodynamically and kinetically more stable. Besides the electrostatic stabilization of the aggregates existing in low MW surfactants, macromolecular aggregates are also stabilized by steric or electrosteric mechanisms. Furthermore, they are characterized by much lower critical micellization concentrations (CMC). In addition, amphiphilic block copolymers are characterized by a much lower mobility compared to low MW surfactants hence the life time of amphiphilic block copolymer micelles is found within seconds, minutes or hours compared to a much shorter life time of micelles created via self-assembly of low MW surfactants (msec.) [40, 48]. Their ability to solubilize in different solvents and the presence of functional groups make them versatile in numerous industrial applications such as stabilizers in colloidal systems, emulsifiers, compatibilizers, nanoreactors and in biomedical applications as colloidal dispersants, surface modifiers and drug carriers [21,38,45]. Additionally, they can be used in nanolithography, nanomaterial synthesis, in separation processes, pharmaceutical formulation and other dispersant technologies [49]. All the above-mentioned applications are closely correlated to the self-assembly behaviour of block copolymers.

Block copolymers self-assemble to form a micelle with defined size and shape [18]. The size (usually 10-100 nm) and shape of microdomains, formed by AB diblock copolymers, depend on four basic parameters:

i. The degree of polymerization (DP) which is equal to the sum of DPs of the two blocks,

ii. The composition of each block, i.e. $f_A = DP_A/DP$ and $f_B = DP_B/DP$ (where DP_A and DP_B the degree of polymerization of the A and B blocks respectively),

iii. The Flory-Huggins interaction parameter $\chi_{AB,}$ which characterizes polymer A/polymer B interactions, and

iv. The polymer/solvent interactions [13,40,47].

Assuming that the micellar core is mostly constructed of B blocks and the corona of A blocks, three different micellar structures may exist, depending on the relative block lengths of the two blocks [13,40]:

- if $DP_A >> DP_B$, meaning that the corona is much larger than the core, then the size of the corona almost equals to the size of the micelle. This micellar type is called "*hairy micelle*" (Figure 1.3.a) [42,50].
- In the opposite situation, where $DP_A << DP_B$, the core is much larger than the corona and a so-called "*crew cut micelle*" is formed (Figure 1.3.b) [42,50].

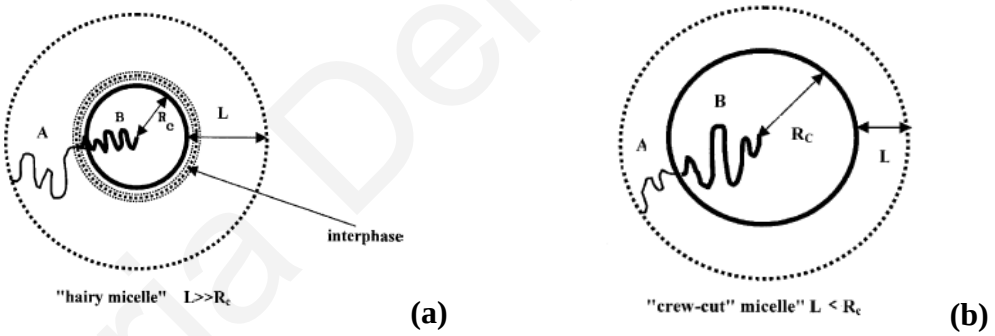

Figure 1.3: *Schematic representation of AB diblock copolymer micelles in a selective solvent for the A block. (a) hairy micelle, (b) crew-cut micelle. R_c: core radius; L: corona thickness [47].*

"*Amphiphilic micelles*" represent a third class of micelles formed (as their name denotes) by amphiphilic block copolymers. These systems are characterized by large interaction parameter χ. In this term both types of micelles (hairy and crew-cut) can be included as long as strong aggregation (i.e. high χ) is involved [13,51]. If the interaction parameter χ_{AB} (corresponding to interactions between the two blocks), is approximately equal to the one which describes the

polymer/solvent interactions of the one block (χ_{BS}) and these are much larger than that of the polymer/solvent interactions of the second block, (χ_{AS}), then χDP can serve as a parameter for characterizing the tendency for microphase separation [13,40].

1.2 Controlled Radical Polymerization

In order for the structural characteristics of polymers to be correlated to their properties, the polymer chains should be characterized by controlled molecular weights (MW_s) and low polydispersity indices (PDI_s). Hence, synthetic polymer chemists have been focused in developing new polymerization methods that could be used for the preparation of polymers with various compositions and architectures characterized by pre-determined MW_s and narrow MWD_s. Controlled radical polymerization techniques play a dominant role in the industrial preparation of a wide variety of polymeric materials because of their mild reaction conditions, compatibility with a wide range of monomers and high tolerance to impurities, water, functional groups and additives [52]. There are versatile techniques used to prepare polymers based on various monomers such as styrenes, (meth)acrylates and dienes [53]. During the last decade several advanced techniques of controlled radical polymerization have become available, including nitroxide-mediated polymerization (NMP), atom transfer radical polymerization (ATRP) and reversible addition-fragmentation chain transfer (RAFT) polymerization [54]. In this work, RAFT polymerization was employed for the synthesis of homopolymers, random and diblock copolymers.

1.2.1 Nitroxide-Mediated Polymerization (NMP)

NMP is one of the simplest controlled radical polymerization methods, based on the equilibrium between dormant alkoxyamine species and an active carbon-based radical. NMP can be performed with minimal purification of reagents and under mild reaction conditions [55].

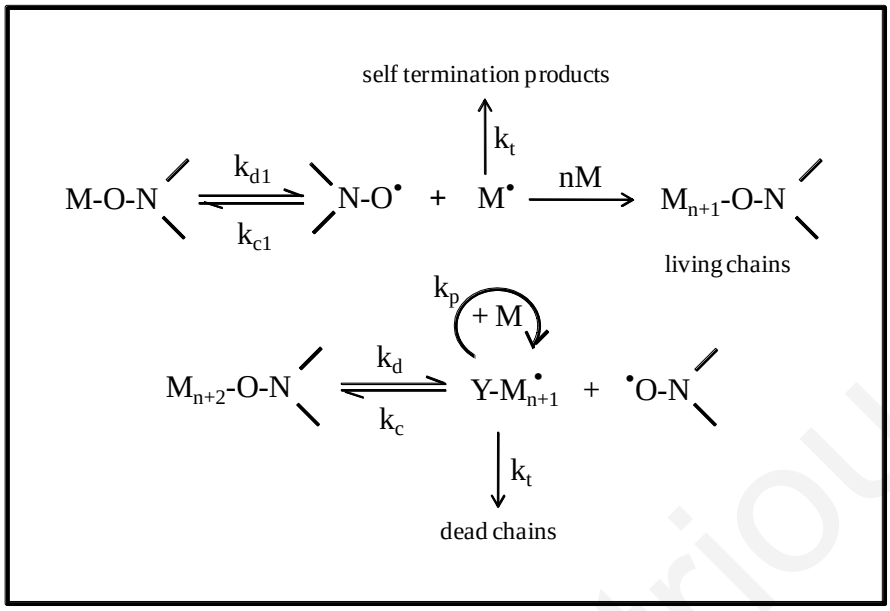

Figure 1.4: *Mechanism of NMP.*

The mechanism involves the reaction of the propagating species ($M^{\cdot}$) with a stable radical ($N\text{-}O^{\cdot}$) as seen in Figure 1.4. The resulting dormant species (M-O-N) undergoes reversible homolytic bond dissociation and generates the active species once again. Once $Y\text{-}M^{\cdot}_{n+1}$ forms, it can then react with a monomer, M, and propagate further. The reversible dissociation of the (macro)alkoxylamine decreases the probability of irreversible termination reactions. As a result, a majority of dormant living chains can grow until the monomer is consumed, producing polymer chains with equal chain lengths and with a reactive chain end. The most commonly used stable radicals are nitroxides, especially 2,2,6,6-tetramethylpiperidinoxy (TEMPO) [56,57]. TEMPO is used to control the polymerization of styrene and its derivaties. It is not suitable for the polymerizaztion of other monomers. New nitroxides, particularly acyclic nitroxides have been developed for the controlled polymerization of acrylate derivatives, acrylamides and dienes [56,58]. Nevertheless, the major limitation of NMP is its incompatibility with methacrylate derivatives [56]. Moreover, this polymerization requires high polymerization temperatures (125-145 ^{o}C) and long reaction times (24-72 h) [58].

1.2.2 Atom Transfer Radical Polymerization (ATRP)

The name Atom Transfer Polymerization originates from the atom transfer step, which is the key elementary reaction responsible for the uniform growth of polymeric chains. In ATRP a transferable (pseudo) halogen and a catalyst are employed during polymerization. A general mechanism for ATRP is shown in Figure 1.5. The active species are generated through a reversible redox process of alkyl halides with a transition metal complex (M_t^n-Y/Ligand), e.g. Cu^I/bipyridine, which behaves as a halogen atom transfer agent between the active and the dormant species. The active species initiate the monomer, which can then propagate with additional monomer or abstract the halide from the metal complex forming a dormant alkyl halide species. The alkyl halide species is then activated by the metal complex and propagates once more. α-haloesters or benzyl halides are usually used as initiators. A wide range of transition-metal complexes, such as Ru-, Cu-, and Fe-based systems, have been successfully applied in ATRP [59].

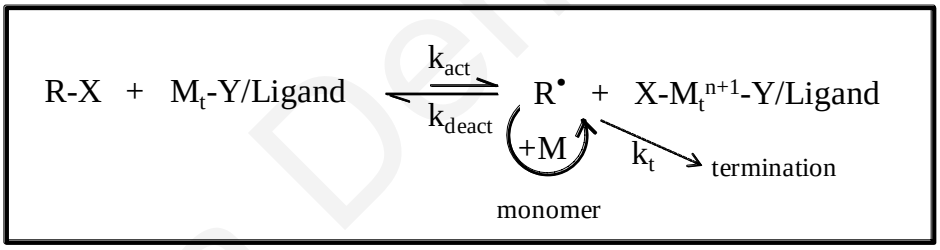

Figure 1.5: *Mechanism of ATRP.*

ATRP is more versatile than NMP in terms of diversity of polymerizable monomers. Substituted styrenes [60,61], acrylates [61,62], methacrylates [60,61,62] and acrylointrile [60,61] have been polymerized in a control fashion. It requires ambient reaction conditions and remains unaffected by the presence of O_2 and other inhibitors. The major drawback of ATRP is that it involves the use of a transition metal catalyst which after polymerization must be removed and if possible recycled [57].

1.2.3 Reversible Addition-Fragmentation Chain-Transfer Polymerization (RAFT)

In the last years, Reversible Addition-Fragmentation Chain-Transfer (RAFT) polymerization has evolved into one of the leading controlled radical polymerization techniques [63]. The RAFT process employs a molecule called the chain transfer agent (CTA), that reacts with a propagating (macro)radical, and it is characterized by a high transfer constant in the reactive system [63.64]. Such molecules are usually dithiocarbonyl compounds. The most common ones are the cumyl dithiobenzoate (CDTB) and the 2-cyano-2-propyl benzodithioate (CPDB) (which are the CTAs used in this work), whereas other CTA having hydrophilic segments are used in cases where RAFT polymerization is carried out in aqueous media [65,66]. In Figure 1.6 the chemical structures of CDTB and CPDB are shown, together with the general chemical structure of the dithiocarbonyl compounds.

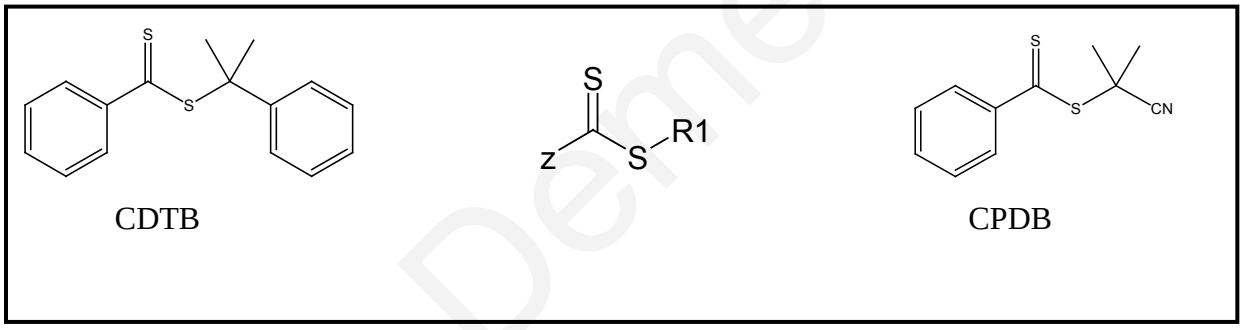

Figure 1.6: *General chemical structure of dithiocarbonyl compounds as well as chemical structures of the two most commonly used CTAs: CDTB and CPDB.*

In order to achieve high chain transfer constants, *Z* should be able to activate the C=S double bond and modify the addition and fragmentation rates [67]. Aryl and alkyl groups are suitable for this purpose, whereas dialkylamino and alkoxy groups are considered less effective [67,68]. In addition, R_1 should be a good free radical leaving group compared to the propagating radicals, and capable to re-initiate free radical polymerization. Initiation of polymerizations is accomplished by the presence of azo and peroxy initiators which decompose and form radicals. Figure 1.7 presents the proposed mechanism for RAFT polymerization.

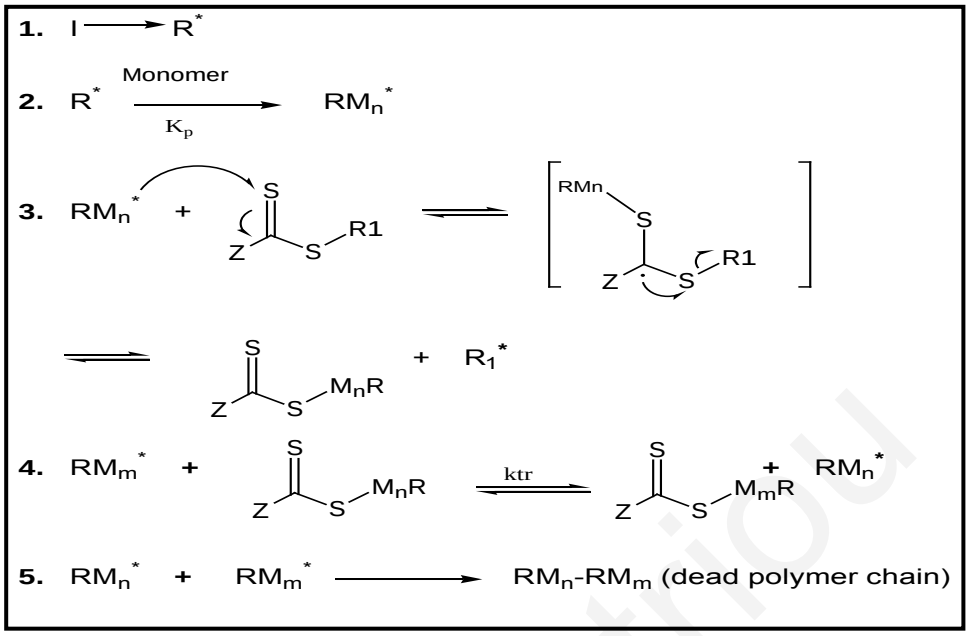

Figure 1.7: *Proposed mechanism for the RAFT controlled radical polymerization.*

At the first stage, the initiation of the polymerization process is accomplished by the formation of radicals, due to the decomposition of the initiator I (Step 1). Subsequently, the reaction of the propagating radicals with the CTA molecules (Step 2) leads to the formation of "dormant" chains and radical leaving groups R_1* (Step 3), which are capable of initiating another chain. Through this equilibrium, chains convert from propagating radicals to polymeric CTAs, meaning that they all grow incrementally with conversion. Hence, the amount of radicals remains constant during the whole process [69,70,71].

RAFT has proved to be a versatile polymerization technique, allowing for the preparation of well-defined polymers with functional moieties [63,71]. The process shows many of the characteristics of controlled polymerizations such as narrow MWD (usually <1.2) and linear MW vs conversion profile. RAFT can be applied to prepare block copolymers and other more complex polymer architectures such as stars [72], branched [73] or block copolymer networks [74].

The DP can be easily calculated by using equation:

$$polymer\ yield\% * [M]_o / [CTA]_o \qquad (2.5)$$

where x is the monomer conversion (polymerization yield), $[M]_o$ is the initial monomer concentration and $[CTA]_o$ is the initial concentration of the chain transfer agent [75].

Another advantage of RAFT is that it is compatible with a wide range of monomers (including functional monomers containing for example acidic, hydroxy or tertiary amino groups, that are not always polymerizable by NMP or ATRP) and reaction conditions, since there is no particular limitations on solvent or reaction temperature [63,64,71].

Furthermore, RAFT polymerizations can be performed in bulk [76], solution [77], emulsion [78], miniemulsion or suspension [79].

RAFT appears to be the most appropriate controlled radical polymerisation method to be applied in this work because it does not involve any kind of a metal ion complex catalyst, as in ATRP, which as demonstrated by Krasia *et al* [80] interferes with the β-dicarbonyl group of 2-(acetoacetoxy)ethyl methacrylate (AEMA), the ligating monomer used in this work.

1.3 Metal Nanoparticles (MNPs)

The term metal nanoparticle is normally used to describe small particles of metal, metal oxides or semiconductor materials which have been controllably synthesized within the nanometer range (1-100 nm) [81]. MNPs are currently interesting due to their unique properties which are quite different from those of bulk materials. These properties depend on their size, morphology, or the surrounding medium [82]. In particular, they are characterized by high surface-to-volume ratios, unique reactivities and spectroscopy features due to the size quantization effects [44,83,84]. MNPs can be employed in a wide range of chemical, physical and biomedical applications [82,83,85,86].

1.3.1 Synthesis of Metal Nanoparticles

Many methods have been developed for the preparation of MNPs, including mechanical alloying/milling of bulk metal [87], sol-gel processes [88], laser ablation [89], chemical reduction of metal ions with chemical reductants (such as H_2, hydrazine, $NaBH_4$, sugars) [90], chemical reduction in organometallic precursors [91], photoreduction [92], decomposition of

metal precursors with extra energy such as thermal [93] or photochemical [94] decomposition, metal vapour synthesis [95], sonochemical synthesis [96], electrochemical reduction [97] and sonoelectrochemical synthesis [98].

The major difficulty in working with nanoparticles is their undesirable agglomeration to form larger particles because they are too small and thermodynamically unstable [81]. Regardless of the method used, a protective agent such as surfactants, ligand, exchange materials and polymers are generally necessary to prevent aggregation. These agents generally contain functional groups such as amines, alcohols, thiols, leading to an increase in the strength of the interactions between the inorganic surface and the organic stabilizing agent [99]. Beside their stabilization, an important goal is the controlled synthesis of metal nanoparticles or well-defined nanostructures consisting of metal nanoparticles in order to obtain particles with uniform diameters and shapes since these parameters influence the material properties [44, 81, 100]. Most of the preparation methods are nucleation-and-growth processes that require demanding isolation procedures making metal nanoparticles too expensive for industrial applications [83,101]. Both, stability and concentration problems can be overcome by the implementation of the nucleation-and-growth process in solid polymer matrices or self-organized polymer media such as micelles, vesicles and inverse micelles [83].

Several methods for preparation of metal nanoparticles involve the presence of a polymer during the reduction of a metal precursor in solution. A very selective method employs amphiphilic block copolymer micelles formed in selective solvents (aqueous and organic), for metal colloid nanoparticle preparation. The use of block copolymers as a medium for the formation of metal nanoparticles not only provides an improved stabilization and control over the growth of nanoparticles, but imparts new properties to polymeric materials [44,85,102]. Consequently, there is a localization of nanoparticle generation within the micellar cores, and a tremendous size control of the MNPs due to the spatial confinement created by micelles. Additionally, the MNPs- block copolymer micellar solution can be easily deposited on a solid substrate or be directly patterned at a surface by using selective wetting, leading to the formation of metal nanoparticle arrays in the solid state [103].

1.3.2 Stabilization of Metal Nanoparticles

As already mentioned, a major problem during the synthesis of MNPs is their aggregation. Therefore, the stabilization of MNPs is a crucial aspect to be considered during their synthesis [97b]. The aggregation occurs in the absence of repulsive forces when two metallic particles with short interparticle distances attract each other due to Van der Waals forces. Consequently, the use of a protective agent capable of inducing a repulsive force opposed to these forces is essential to provide stability in the system [97b,99].

The stabilization of MNPs during their synthesis can be electrostatic (charge stabilization), steric, or electrosteric (combination of steric and electrostatic) [104].

The electrostatic stabilization is based on the repulsion between similarly-charged nanoparticle surfaces in solution. This is the main stabilization mechanism of particles in aqueous solutions. As electrostatic stabilizing agents low-molecular weight species such as inorganic ions [105] and surfactants are used [90c]. The adsorption of these stabilized agents and of their related counter ions on the metallic surface generates an electrical double-layer around the particles. (Fig. 1.8). This results in the development of Coulombic repulsion forces that prevent agglomeration. Electrostatic stabilization is very sensitive to any phenomenon capable of disrupting the electrical double layer like ionic strength or thermal motion [99,106].

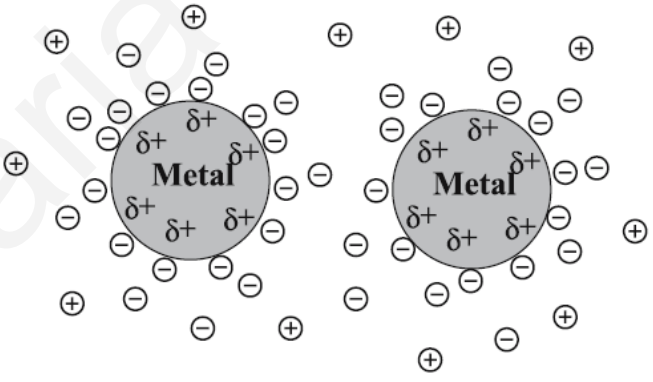

***Figure 1.8**: Schematic representation of electrostatic stabilization [97b]*

The steric stabilization is obtained by polymers or oligomers. The adsorption of these molecules onto a metallic surface generates a protective layer as shown in Fig. 1.9. In contrast

to the electrostatic stabilization mechanism, the steric stabilization can be used in both aqueous and organic solutions [97b,99]. Steric stabilization of MNPs by homopolymers, random and block copolymers is based on entropic and osmotic effects. Particularly, the reduced configurational freedom of the polymer chains in the region between particles causes a decrease in entropy and an increase in the free energy, while the increased concentration of the polymer in the interparticle region results in an increased local activity which in turn leads to an osmotic repulsion to restore the equilibrium by diluting the macromolecules and thus separating the particles [97b,107]. Additionally, polymers provide MNP stabilization not only because of the steric bulk of their framework, but also upon weak binding to the MNP surface of heteroatoms, playing the role of ligands.

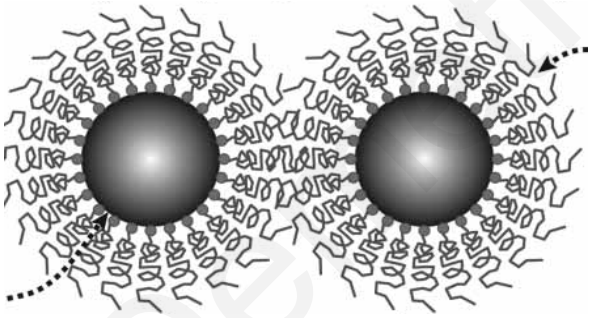

Figure 1.9*: Schematic representation of steric stabilization [104b]*

The electrostatic and steric effects can be combined to stabilize MNPs. This kind of stabilization is generally provided by ionic surfactants or polyelectrolytes [106]. These stabilizing agents bear a polar head group able to generate an electric double layer and a lypophilic side chain resulting in steric repulsion [97].

1.4 Hybrid NanoMaterials: Block Copolymers - Metal Nanoparticles

The combination of polymeric with inorganic materials aims in obtaining hybrid materials with synergetic or complementary behavior between the polymer and the inorganic counterpart. Polymers can be used to yield hybrid materials with desirable combination of properties that are not easily achieved by other means [108]. The properties of the designed

composites depend on both the characteristics of the polymers and the nature of the inorganic material.

Specifically, the formation of uniform MNPs within well-defined polymer-based nanostructures, derived from the self-assembly of amphiphilic block copolymers whose size and shape characteristics as well as the chemical functionality can be tailored, leads to the formation of advanced hybrid materials with new properties, functionalities and applications [82,109].

1.4.1 Applications of polymer-metal nanohybrids

- ***Polymer-metal nanohybrids in catalysis***

Nanosized metal particles stabilized by block copolymers are highly promising for the development of tailored catalytic materials and have been extensively studied by several groups, especially the Pd-containing systems. The use of block copolymers in such applications has a further advantage, since they retard the oxidation of the metal nanocatalyst and prevent its deactivation [104b,110]. Mayer et al. [110] synthesized palladium and platinum nanoparticles stabilized by poly(styrene)-*b*-poly(methyl methacrylate) (PS-*b*-PMMA, the b denotes the block copolymer structure) block copolymers and showed that these systems were catalytically active for the hydrogenation of cyclohexene with final conversions up to 100%. The metal nanoparticles were incorporated in the PS hydrophobic micelle core. Antonietti *et al.* [97] reported on the solubilization and stabilization of Pd NPs in block copolymer micelles of poly(styrene)-*b*-poly-4-vinylpyridine (PS-*b*-P4VP) was formed in various solvents (PS-selective), in order to develop block copolymer stabilized colloidal catalysts. Such catalysts, prepared from different sizes of block copolymers, different polymer-metal stoichiometries. and different Pd salts, have been compared in terms of their catalytic activity with the activity of a commercial Pd-catalyst. They have observed that the block copolymer-stabilized colloids show almost the same activity, but longer life times and higher selectivities than the commercial Pd-catalyst in hydrogenation reactions. Furthermore, they studied the catalytic activity of these systems in the Heck reactions. It was demonstrated that their reactivities were similar to those of some low molecular weight complexes [98]. Pd and bimetallic (PdAu, PdPt and PdZn) nanoparticles formed in (PS-*b*-P4VP) block copolymer

micelles were synthesized and their catalytic activity was studied by Bronstein et. al [111]. In these block copolymers, the P4VP core serves as a nanoreactor for metal nanoparticle formation. PS-*b*-P4VP coated Pd NPs were found to be promising catalysts for the hydrogenation of long chain acetylene alcohols combining high selectivity, stability and satisfying activity. In the case of bimetallic particles, their catalytic activity was higher due to the increased number of active centers on the particle surface.

- ***Polymer-metal nanohybrids in biomedicine***

Research has been focusing on the design and synthesis of nanohybrid biomaterials with specific properties such as high biodegradability and bioactivity, for biomedical applications such as in therapeutic (hyperthermia, drug-delivery/targeting) and diagnostic (nuclear magnetic resonance (NMR), ultrasound (US), optical imaging) fields. Such systems include among others: iron oxides or gold nanoparticles encapsulated within biocompatible or/and biodegradable block copolymers [112]. Polymer coatings on particles enhance compatibility with biomolecules, reduce susceptibility to leaching, and protect particle surfaces from oxidation. Consequently, encapsulation improves dispersibility, chemical stability, and reduces toxicity [113]. Papaphilippou et al. [112a] synthesized and characterized superparamagnetic hybrid micelles based on iron oxide nanoparticles and well-defined poly(ethylene glycol)methyl ether methacrylate-*b*-poly((2-acetoacetoxy) ethyl methacrylate) (PEGMA-*b*-PAEMA) block copolymers. The encapsulation of iron oxide magnetic nanoparticles was accomplished *via* complexation with the AEMA ligating block, forming the micellar core. These micelles exhibited superparamagnetic behavior and *in vitro* biocompatibility, which are important parameter for their potential use as magnetic resonance imaging contrast agents.

Multifunctional polymeric micelles with cancer-targeting ligand for controlled drug delivery and efficient magnetic resonance imaging (MRI) contrast characteristics were developed by N. Nasongkla *et al*. [114]. For this purpose amphiphilic block copolymers micelles based on maleimide-terminated poly(ethylene glycol)-block-poly(D,L-lactide) (MAL-PEG-PLA) and methoxy-terminated poly-(ethylene glycol)-block-poly(D,L-lactide) copolymer (MPEG-PLA) were used. Within the micellar hydrophobic cores, the chemotherapeutic agent doxorubicin (DOXO) and superparamagnetic iron oxide NPs (SPIONs) were encapsulated. The DOXO

was released by the polymeric micelles *via* a pH-dependent mechanism and SPIONs were used as MRI agents for ultrasensitive detection.

Dongkyu Kim *et al.* [115] have studied the feasibility of biocompatible polymer-coated gold nanoparticles (Au NPs) as a potential computed tomography contrast agent for angiography and hepatoma detection in vivo, since Au NPs have a higher X-ray absorption coefficient than the iodine agents normally used. They synthesized polyethylene glycol (PEG)-coated Au NPs, where the Au NPs were covalently conjugated to thiolated PEG. PEG-SH was chosen as a coating material because it is biocompatible and spontaneously forms a chemisorbed surface layer on gold surfaces. They showed that the PEG-coated Au NPs can be used as efficient computed tomography contrast agents for hepatoma exhibiting prolonged circulation time in the blood stream.

- ***Polymer-metal nanohybrids in optoelectronics***

Polymer-metal nanohybrid materials are very promising candidates for optoelectronic devices. Polymer light-emitting diodes (PLEDs) based on poly(9′,9 -dioctylfluorene) (a blue emitting polymer) and gold-nanoparticles were fabricated by Jong Hyeok Park [116]. By incorporating within the blue emitting polymer the gold nanoparticles (5-10 nm), blue-PLEDs with enhanced luminescent stability and quantum efficiency were obtained. The gold NPs used as the quenchers of the triplet states of poly(9,9 -dioctylfluorene) resulted in the oxidation of the polymer. Waldo J. E. Beek *et al* [118] have reported the fabrication of hybrid polymer–metal oxide thin films based on poly-[2-(3,7-dimethyloctyloxy)-5-methyloxy]-para-phenylene-vinylene] (MDMO-PPV) and zinc oxide NPs (ZnO) as well as the development of hybrid bulk-heterojunction solar cells. The external quantum efficiency and power conversion efficiency of this new type of solar cell represents a fourfold improvement compared to the existing hybrid solar cells based on metal oxides.

Moreover, MNPs embedded in polymer matrices have been shown to exhibit large and ultrafast NLO response, a fact that makes them very promising candidates for various photonic applications in optoelectronics such as optical limiting, optical switching etc. The NLO response of suspensions of Au nanoclusters encapsulated into poly(isoprene)-*b*-poly(acrylic acid) (PI-*b*-PAA) block copolymer micelles was investigated by Couris et al. The PAA segment constituted the micellar core, in which the Au nanoclusters were encapsulated. By increasing the PI:PAA ratio or reducing the PAA:Au ratio the NLO response increased.

Furthermore, these systems have been shown to exhibit large optical limiting efficiency [118]. Tsuchiya et al. investigated the enhancement of the optical nonlinearities of gold nanoparticles by using the periodic microphase-separated structure of PS-*b*-PMMA and poly(styrene)-*b*-poly(*tert*-butyl methacrylate) (PS-*b*-PtBuMA) diblock copolymers as templates for their dispersion. The introduction of gold nanoparticles into microphase-separated structures caused the local field effect and the effect of periodic gold nanoparticles arrays and consequent enhancement of the optical nonlinearities of the nanoparticles [119].

The present work has been focusing on the development of novel polymer-metal nanohybrids comprise of well-defined, functional diblock copolymers and MNPs (Pd), which have been further characterized for determining their NLO properties.

Chapter 2 describes the basic principles of the characterization methods used to determine the chemical, thermal and optical properties of the newly synthesized copolymers and hybrids. In Chapter 3 a detailed description of the synthetic methodologies employed in the present thesis is provided. Chapter 4 discusses the synthesis of the polymers as well as their characterization in regards to polymer molecular structure, aggregation behavior, thermal properties and morphological characteristics of the polymeric materials and the polymer-metal nanohybrids. In Chapter 5, the investigation of the NLO response of the polymer-metal nanohybrids in organic media is discussed. Moreover, the applicability of the synthesized systems in nanowire growth and chemical sensing is also presented.

2. CHARACTERIZATION METHODS

In Chapter 2, the basic principles of the characterization methodologies such as molecular (SEC, NMR), thermal (TGA, DSC), optical (UV-vis, fluorescence, Z-scan), microscopy (AFM, SEM, TEM) and scattering (DLS) characterization methods used in the present thesis are described.

2.1 Size Exclusion Chromatography [31,120]

Size exclusion chromatography (SEC) is well known as a special kind of liquid chromatography used in the fractionation and determination of average molecular weights (MWs) and molecular weight distributions (MWDs) of polymers. During this process macromolecules are separated according to their hydrodynamic volume (size in solution).

Separation of macromolecules on the basis of their molecular weight by SEC has been considered to be caused by geometry-dependent partition of macromolecules between a continuous phase and the porous interior of microporous glass beads or swollen polymer gel in which the pore size is comparable to the size of the molecules to be separated. A dilute polymer solution containing a broad molecular-weight distribution of polymer chains, oligomers or even unreacted monomer is allowed to flow through the column. The volume of a pore accessible to a solute is limited by its relative dimensions. Therefore, larger molecules will have access to a smaller volume and will remain in a pore for a shorter time than smaller molecules which are retarded by permeation into the gel pores and are eluted later. The separation process is illustrated in Figure 2.1.

SEC differs from other chromatography methods due to the fact that the former, separations are accomplished in the absence of any interactions taking place between the stationary phase and the sample. Interactions are undesirable and prevent a purely size based separation.

SEC is a relative method for the determination of polymer MWs. This can be achieved by calibrating the system. Calibration is performed with the use of homopolymers which have been previously well characterized in terms of MW_s using absolute methods such as osmosis and light scattering. These samples are known as polymer “standards” and are characterized by very narrow MWDs. The polymer concentration in the analyzer is measured as a function of time or elution volume (V_e). The measured elution volumes are plotted as a function of the

molecular weight ($logM = f(V_e)$). A typical calibration curve, created using poly(methyl methacrylate) (PMMA) standards is presented in Figure 2.2.

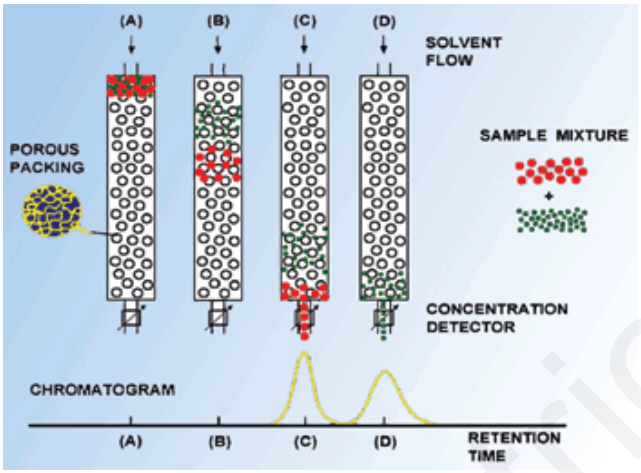

Figure 2.1: *Schematic representation of the fractionation process occurring for a dilute polymer solution in SEC [120].*

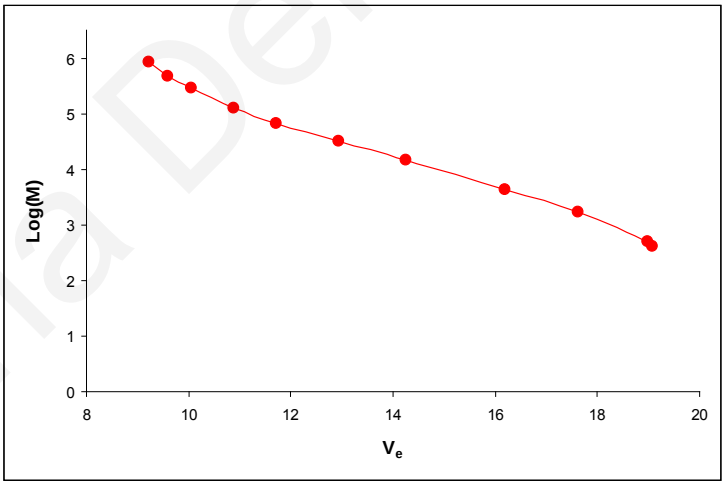

Figure 2.2: *SEC calibration curve based on well-defined PMMA standards [120].*

The molecular weight corresponding to each chromatographic fraction can be determined *via* the calibration curve. Therefore, from the obtained data, number- and weight-average molecular weights ($\overline{M}_n$, $\overline{M}_w$ respectively) can be calculated among others (equations 2.1 and 2.2 respectively, where C_i is the sample concentration and M_i is the molecular weight of the

fraction) and with them the polydispersity index (PDI = $\overline{M}_w / \overline{M}_n$). $\overline{M}_w / \overline{M}_n$ takes values from $1 \rightarrow \infty$. If this ratio is equal to 1 then a situation where all molecules have exactly the same molecular weight (i.e monodisperse sample) applies.

$$\bar{M}_n \equiv \frac{\sum_i c_i}{\sum_i c_i / M_i} \qquad (2.1)$$

$$\bar{M}_w \equiv \frac{\sum_i c_i M_i}{\sum_i c_i} \qquad (2.2)$$

The Differential Refractometer (DRI) and viscometry detectors are usually employed in SEC detectors in this work. According to the first method, the difference in the refractive index between the eluted solution and the pure solvent is proportional to the concentration of the polymer chains. The principle of the viscometry detector is based on the difference in pressure between the eluted solution and the pure solvent, which is proportional to the intrinsic viscosity [η] of the polymer.

The determination of the $\overline{M}_n$ for diblock copolymer systems used in the present work combines SEC with ^{1}H NMR. From SEC, $\overline{M}_n$, $\overline{M}_w$ and PDI values for the first block are determined. Thus, knowing the molecular weight of the first block in the block copolymer and calculating the copolymer compositions using ^{1}H NMR (by comparing the peak integrals assigned to the different comonomers), it is possible to determine the degree of polymerization (DP) of the second block within the copolymer.

2.2 Dynamic Light Scattering [121,122,123]

Light Scattering is extensively used for the characterization of polymers or colloidal particles in dilute solutions in terms of size and aggregation behavior. Generally, when a molecule interacts with an electromagnetic radiation, it absorbs and scatters the radiation. Scattering is attributed to the fact that the oscillating electric field of radiation interacts with the electrons

within the molecules, inducing a dipole, which oscillates with the electric field. Since this oscillating dipole is an electromagnetic radiation source, the molecules emit light, what is called *Scattered Light,* J_s. The frequency shifts, the angular distribution, the polarization and the intensity of the scattered light are determined by the size, shape and molecular interactions in the scattering material.

In Dynamic Light Scattering (DLS), monochromatic light with intensity I_o, passes through the sample - a dilute solution of suspended particles - and the latter scatters light in all directions relative to the incident beam. The major portion of the scattered light has almost the same wavelength as the incident radiation. The intensity of the scattered light $I(\theta)$ is detected at angle θ to the incident beam direction and at distance r from the center of the system as shown in Figure 2.3.

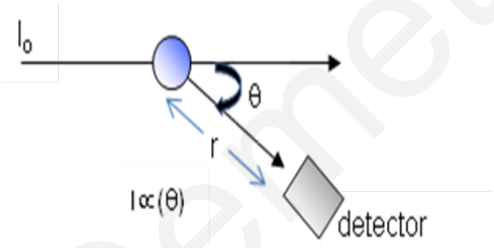

Figure 2.3*: Scattering of monochromatic light by a dilute sample solution and detection of the scattered beam at a specific scattering angle.*

Fluctuations in the scattering intensity at a given scattering angle arise because the phase and polarization of the light scattered by each particle changes with time and the particles continuously rearrange their configuration in the scattering volume due to Brownian motion (random thermal motion of the particles in the sample).

The scattered light coming from each particle has a specific amplitude and phase. It is recorded and analyzed in correlation delay time domain, at the detector. All these small scattered light amplitudes interfere and add up to a different sum, which depends on the relative phases of the moving particles. The relative positions of the particle in the sample volume at any instant determine the magnitude of constructive or destructive interference of the scattered light at the detector. The faster the particles move around, the faster the signal fluctuates. Since the diffusion rate of particles is determined by their sizes in a given environment, information about their size is provided by the rate of fluctuations of the

scattered light. This process is dynamic and therefore the scattering is called Dynamic Light Scattering.

As previously mentioned, the scattering light appears to fluctuate randomly with time. The time variation of the scattered intensity is analyzed by examining their autocorrelation. A digital corellator is used to compute the autocorrelation function. From the measured diffusion coefficient, particle size is calculated.

In DLS the output from the photomultiplier tube is the unormalized intensity autocorrelation function, $G_2(t)$ which is given as:

$$G_2(t) = A + [Bg_1(t)]^2 \qquad (2.3)$$

A is a constant background intensity to which the correlation function decays after a suitably long delay time *t,* and *B* is a constant close to unity. The term $g_1(t)$ is the normalized autocorrelation function which relates to:

$$\Gamma = D_\tau q^2 \qquad (2.4)$$

Γ^{-1} is the relaxation time of the diffusive process of the polymer, D_τ is the translational diffusion coefficient, and *q* is the scattering vector. The latter is expressed as:

$$q = \frac{4\pi n \sin(\theta/2)}{\lambda_o} \qquad (2.5)$$

where *n* is the refractive index of the solvent, θ the scattering angle and λ_o the laser's wavelength.

Assuming that molecules can move freely in the solvent colliding randomly with solvent molecules and considering R_H to be the radius of a sphere with equivalent friction, by using Stoke's Equation (2.6) the hydrodynamic radius R_H can be calculated. k_B is the Boltzmann`s constant, *T* the absolute temperature and η_o the viscosity of the solvent.

$$R_H = \frac{k_B T}{6\pi n_o D_\tau} \qquad (2.6)$$

DLS is considered to be one of the quickest and most convenient methods for the determination of the hydrodynamic radii and polydispersity of colloidal systems. It requires small sample volume and it is not destructive for the sample. The main disadvantages of this technique are that it is very sensitive in the presence of dust and it cannot be used in systems which absorb light at the same wavelength as that of the laser beam.

2.3 Nuclear Magnetic Resonance Spectroscopy [124]

Nuclear Magnetic Resonance (NMR) spectroscopy is a useful and powerful analytical technique for determining the structure of organic compounds. It is a spectroscopic technique which manipulates the magnetic moments of atomic nuclei and magnetic fields. The NMR phenomenon occurs when the nuclei of certain atoms are immersed in a static magnetic field and exposed to a second oscillating magnetic field. The nuclei of atoms have magnetic properties that can be utilized to yield chemical information. Some nuclei experience the NMR phenomenon and others do not, depending upon whether they possess a nuclear spin. In some atoms, the nucleus has no overall spin because their spins are paired and cancel each other out, such as in ^{12}C. In contrast, in many atoms, such as ^{1}H, and ^{13}C the nucleus has an overall spin.

In the absence of an external magnetic field, the spins of a magnetic nucleus are randomly orientated. When a nucleus like ^{1}H and ^{13}C with I = ½ (where I is the nuclear spin), is located between two strong magnets, it will adopt two possible orientations (+ ½ and – ½ presenting different energies). The magnetic moment of the lower energy + ½ state is aligned to the direction of the external field, whereas that of the higher energy – ½ spin state is opposed to the external field. The nucleus prefers to occupy the lower energy level. With the use of electromagnetic radiation, it is possible to excite the nucleus into the higher energy level. The frequency of the radiation needed is determined by the difference in energy (ΔE) between the energy levels, which is defined as:

$$\Delta E = \gamma h B / 2\pi \qquad (2.7)$$

$$\gamma = \mu / L \qquad (2.8)$$

where γ is the gyromagnetic ratio, μ is the magnetic dipole moment, L the angular momentum, h is the Planck's constant and B is the strength of the magnetic field.

When the populations of the higher and the lower state become equal, then there will be no further absorption of radiation and the spin system is saturated. After saturation, it is possible for the nuclei to return to the lower state through the relaxation processes. The relaxation of the spins back to the lower state produces a measurable amount of Radiofrequency (RF) signal at the resonant frequency associated with the spin flip.

In general, a nucleus is surrounded by electrons. Since electrons are moving charges, they obey the laws of electromagnetic induction. Hence, the applied magnetic field, B_o, induces circulation in the electron cloud, in such a way that a local magnetic field, B_{local}, is produced, which opposes B_o (B_{local} is proportional to B_o). Consequently, the actual magnetic field, B_{local}, at the nucleus is always less than the external field B_o and the nucleus is shielded from the external magnetic field (equation 2.9):

$$B_{local} = B_o(1-\sigma) \qquad (2.9)$$

where σ is the shielding constant. The extent of shielding is influenced by many structural features within the molecule, for example protons in different chemical groups have different shielding constants, and hence in the NMR spectrum chemical shifts are observed. The chemical shifts are measured along the bottom of the spectrum on a delta (δ) scale, in units of parts per million (ppm) and the externally applied magnetic field strength increases from left to right. Signals on the left of the spectrum are said to occur downfield and those on the right are said to be upfield. The signal δ=0 in the spectrum arises from a reference compound, such as tetramethylsilane, (TMS, $(CH_3)_4Si$), that is added to the sample to allow calibration of the chemical shift scale. The difference between the frequency of the signal and the frequency of the reference is divided by the frequency of the reference signal to give the chemical shift (equation 2.10). The frequency shifts are extremely small in comparison to the fundamental NMR frequency.

$$\delta = \frac{\nu_{sample} - \nu_{TMS}}{\nu_{sample}} \qquad (2.10)$$

2.4 Ultraviolet-visible Spectroscopy [124,125]

Ultraviolet-visible (UV-*vis*) spectroscopy is used to obtain the absorbance spectrum of a compound in solution or at the solid state. The UV-vis region of energy for the electromagnetic spectrum covers 1.5 - 6.2 eV which relates to a wavelength range of 800 - 200 nm. UV-*vis* uses photons from the ultraviolet (UV) and the visible (vis) region of the electromagnetic spectrum to cause electron excitation from the ground state to the first singlet excited state of the compound or material.

The energy of the photon must be equal to the difference between the two orbital energy levels according to the equation 2.11:

$$\Delta E = h\nu = \frac{hc}{\lambda} \qquad (2.11)$$

where, h is the Plank's constant, ν is the frequency in Hz, c is the velocity of radiation in vacuum, and λ is the wavelength in nm.

UV-*vis* spectroscopy is a very useful analytical technique for the identification of some functional groups in molecules and for determining the content of the different compounds. Different molecules absorb radiation at different wavelengths. In a UV-*vis* spectrum, a number of absorption bands can be presented, corresponding to structural groups within the molecule. Absorbance of UV-*vis* light is directly proportional to the path l and the concentration c of the molecule, according to the Lambert-Beer Law:

$$A = \varepsilon . c . l \qquad (2.12)$$

Where A is the absorbance, l is the path length of the radiation, c is the concentration of the molecule and ε is proportionality constant called the absorptivity or extinction coefficient.

When a molecule absorbs UV or visible radiation, the outer shell (valence) electrons can be excited. This excitation can cause three types of electron transition: (a) transitions involving π, σ and n electrons, (b) transitions involving charge-transfer electrons and (c) transitions involving *d* and *f* electrons. In a molecule where atoms are bonded to each other by covalent bonds, their atomic orbitals mixed together and construct new molecular orbitals like the σ and π bonding, the n non-bonding and the anti-bonding σ^* and π^* orbitals. The atomic orbitals of two bounded atoms are combined to form a "bonded" low energy molecular orbital and an "antibonded" molecular

orbital of high energy. Electrons are excited from the highest occupied molecular orbital (HOMO-bonding) to the lowest unoccupied molecular orbital (LUMO) (Fig. 2.4). An optical spectrophotometer records the wavelengths at which absorption occurs and also the degree of absorption at each wavelength. The resulting spectrum is presented as a graph of absorbance (A) *vs* wavelength (λ). The absorbance of a sample is proportional to the number of absorbing molecules that are present in the light beam.

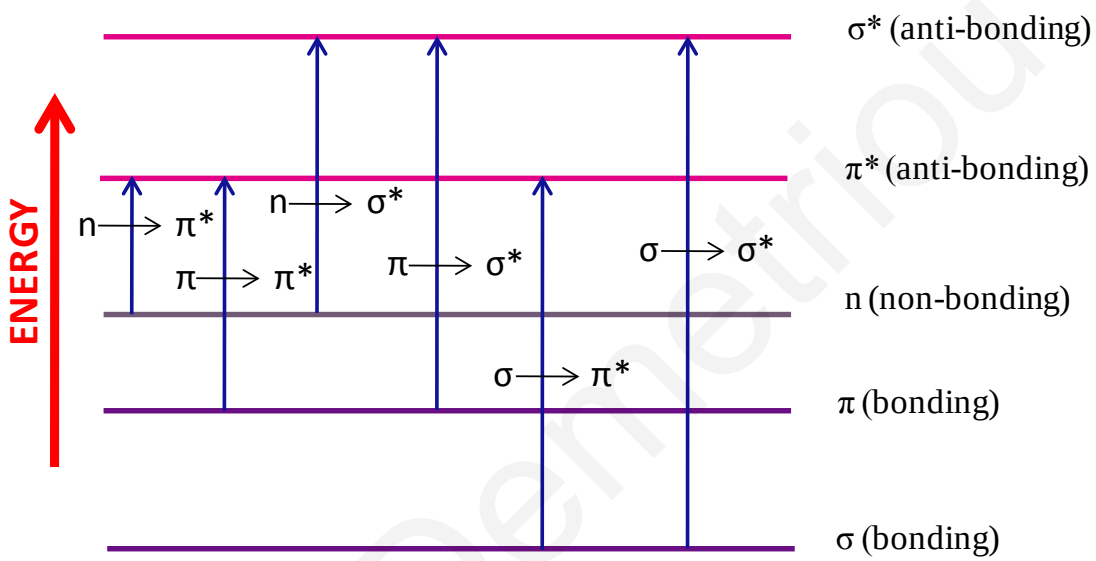

Figure 2.4: *Possible electronic excitations from the HOMO (bonding) to the LUMO (non-bonding or anti-bonding) orbitals.*

2.5 Fluorescence Spectroscopy [125]

Fluorescence is the emission of light from molecules that have been excited at a certain wavelength by an electromagnetic radiation and their relaxation from the singlet excited state to the singlet ground state. The wavelength of the light emitted is longer than the excitation one and is dependent on the energy gap between the ground state and the singlet excited state. Fluorescence has short lifetime (~10^{-8} sec) so that in many molecules it can compete favorably with collisional deactivation, intersystem crossing an ɔhosphorescence.

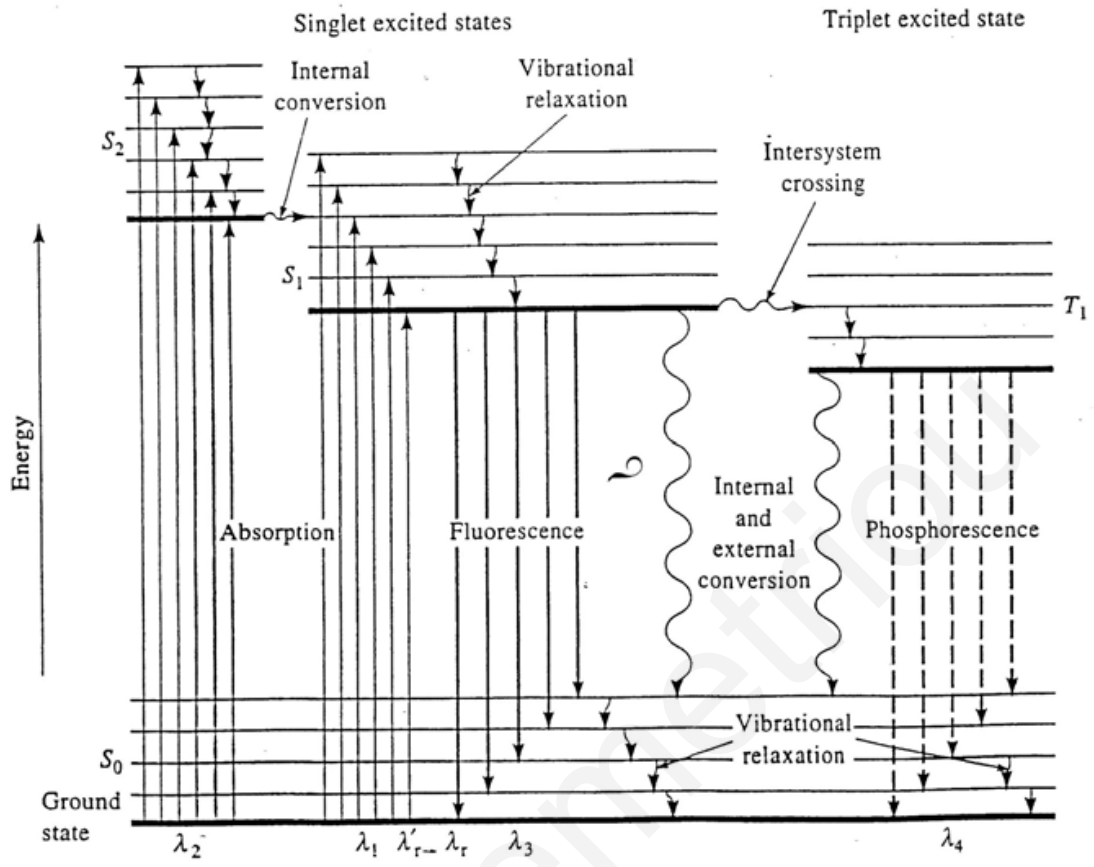

Figure 2.5: *Electronic transition energy level diagram [125b].*

When a molecule absorbed energy and reached one of the higher vibrational levels of an excited state, rapidly loses its excess of vibrational energy by collision and falls to the lowest vibrational level of the excited state. In addition, almost all molecules occupying an electronic state higher than the second undergo internal conversion and pass from the lowest vibrational level of the upper state to a higher vibrational level of a lower excited state which has the same energy. From there, the molecules again lose energy until the lowest vibrational level of the first excited state is reached. From this level, the molecule can return to any of the vibrational levels of the ground state, emitting its energy in the form of fluorescence (Figure 2.5).

2.6 Differential Scanning Calorimetry [126,127,128]

The Differential Scanning Calorimetry (DSC) is a thermal analysis technique that determines the temperature and heat flow associated with material transitions as a function of time and temperature. It is a versatile thermal analysis technique, which can be used to study phase transitions such as melting, crystallization, or glass transition, endothermic or exothermic processes, or changes in heat capacity, as well as crystallization kinetics. Furthermore, it provides information on the crystallization time and temperature, the heat of fusion, the oxidative or thermal stability, any chemical reactions taking place upon heating and the purity of a sample.

DSC gives a measure of the difference in the rates of heat absorption by a sample with respect to an inert reference as the temperature is raised at a constant rate. It can be classified into two types, based on the mechanism of operation: a) Heat flux DSC and b) Power Compensated DSC. In a heat flux DSC, which is used in this work, the sample material enclosed in a pan and an empty reference pan are placed on a thermoelectric disk surrounded by a furnace. The furnace is heated at a linear heating rate and the heat is transferred to the sample and reference pan through the thermoelectric disk. However owing to the heat capacity of the sample, a temperature difference between the sample and reference pan exists, which is measured by the thermocouples and the consequent heat flow is determined by the thermal equivalent of Ohm's law:

$$q = \Delta T/R \qquad (2.13)$$

where q is the sample heat flow, ΔT is the temperature difference between the sample and the reference and R is the resistance of the thermoelectric disk. In the case of power compensated DSC the sample and the reference are placed in separate furnaces, heated by separate heaters. Both, the sample and the reference are maintained at the same temperature and the difference in thermal power required to maintain those at the same temperature is measured and plotted as a function of temperature or time.

Most long-chain synthetic polymers show a characteristic sequence of morphological changes upon heating. All linear polymers are hard, rigid solids and they present a glasslike behavior at low temperatures. By increasing the temperature, the polymer loses its glasslike properties, and changes into a rubber-like morphology. This change occurs at the so called glass transition

temperature, T_g. On the other hand, crystalline polymers remain flexible and thermoplastic above T_g and change to liquid phase at the crystalline melting temperature (T_m). DSC technique is widely used for examining the thermal transitions of a polymeric material such as the T_m and the T_g. As seen in the heat flow *vs* temperature diagram presented in Fig. 2.6, a glass transition of a polymer (amorphous solid) occurs as the temperature is increased. These transitions appear as a step in the baseline of the DSC signal. Upon further increasing the temperature, a semi-crystalline polymer presents the so-called melting temperature T_m. At this point, the crystalline areas existing within the polymer are destroyed and the sample melts. The DSC method may also give information related to the percentage of the crystalline and amorphous content in the sample.

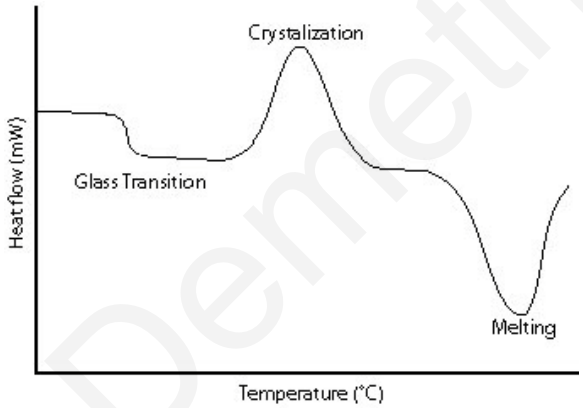

Figure 2.6: *DSC traces indicating the thermal transitions that may occur in a semi-crystalline polymer.*

2.7 Thermal Gravimetric Analysis [126,127]

Thermal gravimetric Analysis (TGA) is a simple thermal analytical technique that measures the weight loss of a sample as a function of temperature. TGA is commonly used to verify polymer degradation temperatures, residual solvent levels, absorbed moisture content and the amount of fillers in composite materials.

The TGA experiments are carried out in an atmosphere of nitrogen, helium or other gas, and also under vacuum, at a temperature range from 25 ^{o}C to 900 ^{o}C. The sample to be analyzed is placed into an alumina cup, which is attached to a sensitive microbalance assembly located outside the furnace chamber. The temperature depends on variables, such as the heating rate,

the nature of the solid and the atmosphere in which the sample is heated. The sample, usually a few milligrams in weight is heated by following a predetermined thermal cycle at a controlled heating rate and has constant weight until it begins to decompose at a certain temperature. The weight loss of the sample is determined by the difference between the initial and the final weight. The TGA curve presents at the Y-axis the change percentage of the sample and at the X-axis the temperature, as depicted in Fig. 2.7.

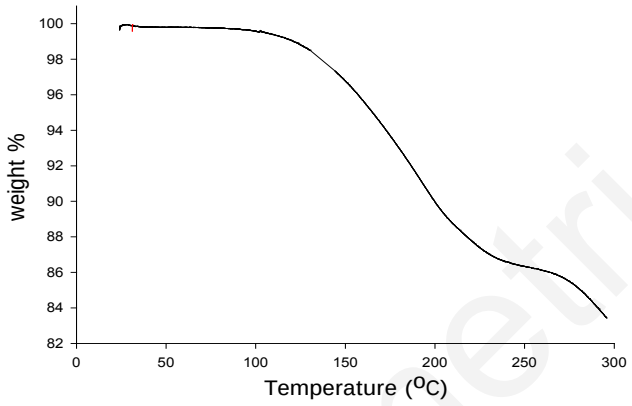

Figure 2.7: *TGA curve.*

2.8 Microscopy Techniques

2.8.1 Atomic Force Microscopy

The Atomic Force Microscopy (AFM) is a three-dimensional imaging technique, which was invented by Binnig *et al*. in 1986. It has evolved into a useful tool for providing information on atomic and molecular scale interactions as well as nanoscale adhesive and elastic response [129,130,131]. Unlike the electron microscopy methods, which often require sophisticated sample preparation procedures, the sample preparation for AFM is easy, fast and allows the material to be preserved in its native state [132].

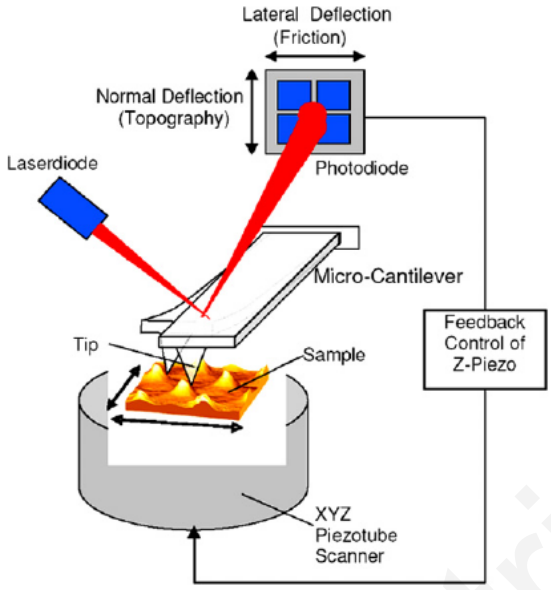

Figure 2.8: *Schematic representation of an Atomic Force Microscope [130].*

A typical AFM system utilizes a sharp tip attached to a flexible micro-cantilever of a specific spring constant. The tip is scanned automatically over the sample surface in a way that enables the piezoelectric tube scanner to maintain the tip at a constant force (obtaining height information) or height (obtaining force information) above the surface of the sample. The cantilever deflects in z-direction due to the surface topography during the tip scanning of the sample surface. A laser beam strikes the backside of the cantilever, and as the tip scans the sample surface moving up and down, the laser beam is deflected off the attached cantilever into a dual element photodiode. The difference in light intensities between the upper and lower photodetectors is measured and converted into voltage [129,130].

Considering the tip approach and the deflection way, AFM can operate in three different modes: the *Contact*, the *Non-contact* and the *Tapping Mode*. In the contact mode, the tip is constantly in close contact with the sample (physical contact). As the tip moves across the sample, the contact force causes the cantilever to bend according to changes in the topography. This mode can be used to analyze hard samples such as silicone matrices, carbon surfaces etc. [129]. In contrast, in the non-contact mode, the cantilever is oscillated quite close to the surface of the sample. This is advantageous since the tip has little or no contact with the sample and for that reason it can be used to analyze soft biomaterials [129,130]. Finally, in the tapping mode, the tip is alternatively placed in contact with a surface and then is lifted off the surface to avoid dragging it across. Tapping Mode is implemented by oscillating the cantilever

assembly at or near its resonance frequency using a piezoelectric crystal [130,133]. The piezo motion causes the oscillation of the cantilever usually when the tip is not touching the surface. The oscillating tip is then moved slowly towards the surface and begins to tap it lightly. When the cantilever touches the surface, its oscillation amplitude is reduced due to the loss in energy. It is this reduction that is used for measuring the characteristics of a surface. With tapping mode, "problematic" sample surfaces, which can be easily damaged and are held weakly to their substrate or are difficult to visualize with other AFM techniques, can be topographically imaged with high resolution. Moreover, the intermittent contact motion of the tip in tapping mode eliminates lateral (friction, adhesion forces) or shear forces which would deform the sample [129]. Tapping mode is considered to be the best mode for imaging soft and fragile samples such as polymers and biological objects and therefore it is the one used in the present work. Finally, tapping mode operates in a large, linear range allowing reproducibility of a measurement. AFM phase imaging in tapping mode is a widely employed and useful technique for the characterization of phase-separated materials, especially if the material phases have distinct physical properties.

2.8.2 Scanning Electron Microscopy [127]

Scanning Electron Microscopy (SEM) constitutes one of the oldest and most widely used methods for surface analysis, since it provides a three-dimensional visual image, with a qualitative relatively straightforward analysis. In SEM, scanning a focused electron beam along the specimen of interest creates an image. The beam interacts with a thin layer (few micrometers) at the surface of the specimen. This interaction causes the production of secondary electrons, which are emitted from the sample surface, are detected and used to modulate the brightness of a synchronously scanned cathode ray tube (CRT). Hence these electrons are responsible for the formation of a TV-type of image. X-rays, characteristic of that part of the specimen probed by the electron beam, allow both a qualitative and quantitative determination of the elements present in the selected region. High energy back-scattered electrons can be separated and also used for image formation. Since the back scattering efficiency is a function of the atomic weight, this image reveals compositional variations due to average atomic number.

2.8.3 Transmission Electron Microscope [134]

The Transmission Electron Microscope (TEM) is an important tool in material science since information about the morphology, structure and composition of a specimen can be obtained. Particularly, it gives details in relation to the size, shape and arrangement of the atoms in the sample. Additionally, it enables the investigation of the crystal structure as well as the quantification of the different elements comprising the specimen.

An electron gun produces a beam of monochromatic electrons, which is focused a small and thin coherent beam by electromagnetic lenses. Then, the beam is restricted by the condenser aperture leaving out high angle electrons. Then the focused electron beam strikes the sample which is on a concrete base namely grid holder and parts of the beam are transmitted. The transmitted radiation is transformed by the objective lens into an image. After the objective lens, optional objective and selected area metal apertures are placed inside the column where they can restrain the beam by blocking out the high angle diffracted electrons and examine the periodic diffraction of electrons by ordered arrangements of atoms in the sample. The beam passes down the column through the projector lenses, being enlarged all the way. Finally, the beam strikes the phosphor image screen and light is generated allowing the user to observe the image. The darker areas of the image represent those areas of the sample through which fewer electrons were transmitted and the lighter areas of the image represent those areas of the sample through which more electrons were transmitted.

TEM can image and analyze successfully a wide range of solid materials, such as metals, ceramics, minerals, polymers as well as other organic and biological materials.

2.9 Z-scan

The Z-scan technique is a simple, highly sensitive, single beam technique that is particularly useful when the nonlinear refraction is accompanied by nonlinear absorption phenomena. By Z-scan, the nonlinear refractive index (γ') and the nonlinear absorption coefficient (β), which are related to the imaginary and real part of the third-order NLO susceptibility $\chi^{(3)}$ respectively can be measured simultaneously in one single measurement [135]. Basically, in this method, translation of a sample through a tightly focused Gaussian laser beam and monitoring of the changes in the far field intensity pattern occurs. Depending on the sample position *z* with

respect to the focal plane, the sample has the tendency to recollimate or defocus the incident beam, due to the light-induced lens-like effect [136,137].

Figure 2.10 shows the schematic diagram of the experimental setup. The excitation source is a Nd:YAG laser. During the Z-scan measurements, a sample is moving along the propagation direction through the focal plane of a focused Gaussian laser beam, experiencing therefore different incident laser intensity at each different position. The transmitted through the sample laser beam is then divided by means of a 50:50 beam splitter into two equal parts and the normalized transmission of the sample is measured by two different configurations, known as "open-aperture" and "closed-aperture" Z-scans respectively. In the former configuration, the transmitted beam is totally collected (e.g. by means of a large diameter lens) and measured by a photomultiplier, while in the latter configuration only a part of the transmitted laser light is collected and measured by an identical and electrically matched photomultiplier, after it has passed through a small aperture placed in the far field.

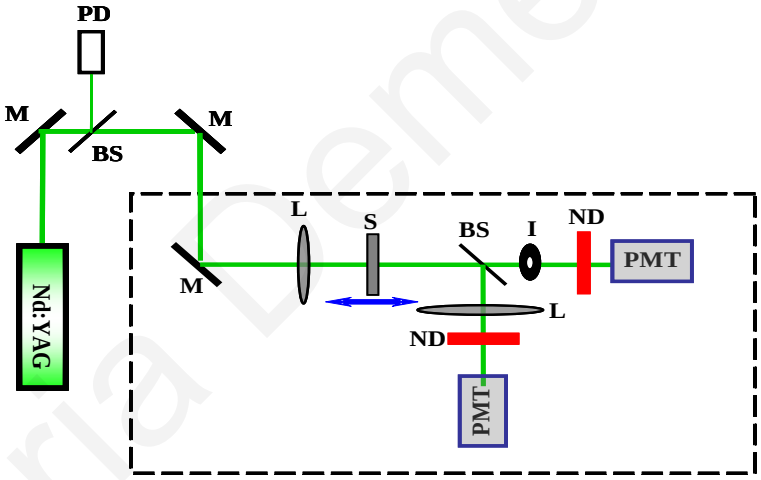

Figure 2.9: *Schematic diagram of the Z-scan experiment setup.*

In the "open-aperture", the totally transmitted through the sample beam is measured, while in the "closed-aperture" only a small central part of the beam is measured after having passed through a small circular aperture positioned in the far-field. The former measurement ("open-aperture" Z-scan) provides the variation of the transmission of the sample while it experiences varying laser intensity. This measurement allows for the determination of the nonlinear absorption parameter β of the sample by fitting the "open aperture" curves with the following equation [138]:

$$T = \frac{1}{\sqrt{\pi}\left[\frac{\beta I_0 L_{eff}}{1+z^2/z_0^2}\right]} \int_{-\infty}^{+\infty} \ln\left[1+\frac{\beta I_0 L_{eff}}{1+z^2/z_0^2}\exp\left(-t^2\right)\right] dt \qquad (2.14)$$

where T is the normalized transmittance, $L_{eff} = \left(1-\exp\left(-a_0 L\right)\right)/a_0$ is the effective thickness of the sample, α_0 is the linear absorption coefficient of the sample at the laser excitation wavelength and I_0 is the on-axis irradiance at the focus. In such Z-scan experiments, the curves are symmetric with respect to the focal point (z=0), where they exhibit a maximum transmittance in the case of saturable absorption and a minimum for the reverse saturable absorption.

As mentioned above, from the "closed aperture" data, information regarding the nonlinear refractive index can be obtained. The transmittance curve can exhibit "peak-valley" or "valley-peak" configuration corresponding to negative and positive nonlinear refractive index respectively (Figure 2.10). As seen in Fig. 2.10.a, the curve presents a maximum in transmittance before the focal plane of the lens and a minimum after the focal plane, therefore the sample exhibits a self-defocusing behavior ("peak-valley"). In contrast, when the sample is characterized by a self-focusing behavior, the curve has a minimum in transmittance followed by a maximum ("valley-peak" (Fig. 2.10.b)). By the "closed aperture" Z-scan, the non-linear refraction parameter (γ') can be measured, assuming that the non-linear absorption is negligible. If the length of the sample is small compared to the Rayleigh beam length, the maximum nonlinear phase-shift can be evaluated from the peak to valley variation of the measured normalized transmittance curve (ΔT_{P-V}). The ΔT_{P-V} is taken to be negative (or positive) when the material exhibits a "peak-valley" (or "valley-peak") transmittance curve. It can be determined by the equation:

$$\Delta T_{P-V} = \frac{1.624\,\gamma' L_{eff} E (1-S)^{0.25}}{\lambda\sqrt{2} w_0^2 \tau} \qquad (2.15)$$

where the factor $(1-S)^{0.25}$ is related to the diameter of the aperture P, E is the energy of the beam, w_0 is the beam radius and τ the time duration of the beam pulses.

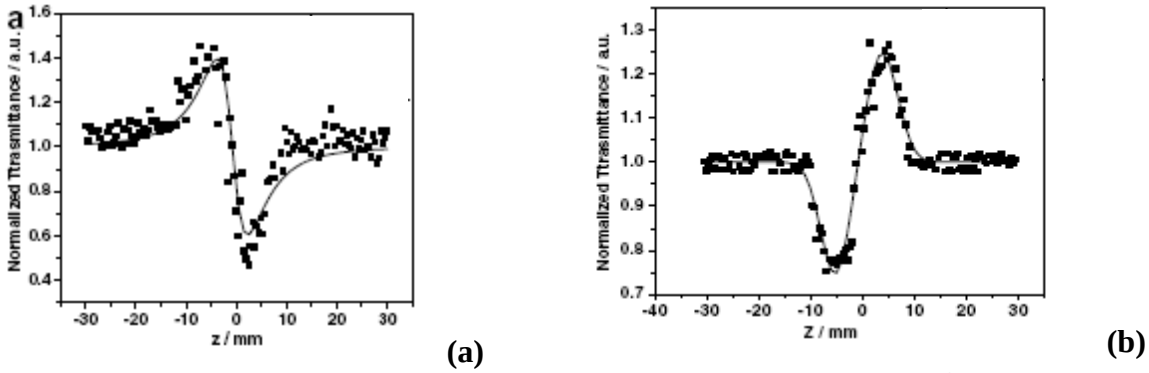

Figure 2.10: *Transmittance curves for samples with (a) positive and (b) negative nonlinear refractive index ("Closed aperture" Z-scan data)* [146].

In the case where the material exhibits both nonlinear refraction and absorption properties, the pure third-order nonlinear refractive index can be obtained by dividing the "closed aperture" data with the "open aperture" data, resulting in a new curve the so-called "divided aperture" Z-scan [137]. The latter curve has the same shape ("peak-valley" or "valley peak") with the "closed aperture" but does not include the contribution of the non-linear absorption.

The resulting curve provides the corresponding γ' through the relation:

$$T = 1 - \frac{4\Delta\Phi_0 x}{\left(x^2+9\right)\left(x^2+1\right)} \qquad (2.16)$$

where: $\Delta\Phi_0 = k I_0 \gamma' L_{eff}$ is the on-axis nonlinear phase shift at the focus and I_0 is the peak intensity of the laser pulse at the focal plane.

Finally, from the nonlinear refraction parameter γ' and the nonlinear absorption parameter β, the real and the imaginary parts of the third-order susceptibility $\chi^{(3)}$ respectively can be easily obtained from the following relations:

$$\mathrm{R_e}\,\chi^{(3)} = 10^{-6} c n_0 \gamma' / (480\pi^2) \qquad (2.17)$$

$$\mathrm{Im}\,\chi^{(3)} = 10^{-7} c^2 n_0{}^2 \beta / (96\pi^2 \omega) \qquad (2.18)$$

3. EXPERIMENTAL

In this chapter a detailed description of the experimental methodology followed for the synthesis of: (a) LauMA-containing BCs, (b) CbzEMA-containing BCs, (c) AnMMA-containing BCs, (d) polymer-metal nanohybrids (Pd, Au) and (e) MNP-assisted metal oxide nanowire growth, is given. Furthermore, details related to the characterization methodologies used are provided.

3.1 Solvents and Reactants

Benzene (Fluka, ≥ 99.5%), ethyl acetate (Scharlau, 99%) and tetrahydrofuran (THF) (Scharlau, 99.9%) were stored over CaH_2 (Merck, 99.9%) and distilled under reduced pressure immediately prior to the polymerization reactions. Chloroform (Scharlau, 99%) was dried over anhydrous $MgSO_4$. Methanol (LabScan, 99.9%), *n*-hexane (LabScan, 99%), toluene (Scharlau, 99.9%), dimethylformamide (DMF) (Aldrich, 99.8%), cyclohexane (Sigma-Aldrich, ≥ 99.9%), dichloromethane (Sigma-Aldrich, ≥ 99.5%), HCl (Merck, 37% solution), diethyl ether (LabScan, 99.5%), benzoic acid (Merck, 99%), aqueous solution of tetrabutylammonium hydroxide (Sigma-Aldrich, 40% w.t), triethylamine (Merck, ≥ 99%), pyridine (Sigma-Aldrich, ≥ 99.9%), hydrazine monohydrate (Sigma-Aldrich, 98%), benzyl chloride (Sigma-Aldrich, 99%), carbon tetrachloride (Riedel de Haën, ≥ 99.8 %), α -methylstyrene (Sigma-Aldrich, 99%), sodium methoxide (Aldrich, 30% solution in methanol), crystalline carbazole (Sigma, ≥ 99.5%), ethylene carbonate (Aldrich, 97%), methacryloyl chloride (Fluka, ≥ 97%), 9-anthracenemethanol (Aldrich, ≥ 98%), 2-cyano-2-propyl benzodithioate (Sigma-Aldrich, > 97%) and deuterated chloroform (Merck) were used as received. The following inorganic compounds were used without further purification: Sulfur (Aldrich, powder ~ 100 mesh), silica gel (Aldrich, 60 Å, 70-230 mesh), NaOH pellets (Scharlau, 99%), KOH pellets (HiMedia, 85%), Na_2SO_4 (HiMedia, 99%), $NaHCO_3$ (Sigma-Aldrich, 99.5%), NaCl (HiMedia, ≥99.0%), $Pd(CH_3COO)_2$ (Sigma-Aldrich, 99.98%), anhydrous $MgSO_4$ (Scharlau, 98%), $HAuCl_4.3H_2O$ (Sigma-Aldrich, ACS reagent, ≥49.0% Au basis), Ga (Aldrich, 99.99%). 2-acetoacetoxy ethyl methacryalte (Aldrich, 95%) was passed through a basic alumina column prior to the polymerizations and used without further purification. Lauryl methacrylate

(Aldrich, 99%) was also passed through a basic alumina column and stored over CaH_2 in the presence of a free radical inhibitor, namely 2,2`-diphenyl-1-picrylhydrazyl hydrate (DPPH, Sigma-Aldrich, 95%). This was followed by distillation under reduced pressure, and storage under nitrogen atmosphere prior to use. 2,2-Azobis(isobutylnitrile) (AIBN, Sigma-Aldrich, 95%) was recrystallized twice from ethanol and dried *in vacuo* at room temperature for three days.

3.2 Characterization Methods

^1H NMR spectra were recorded in $CDCl_3$ using an Avance Brucker 300 MHz spectrometer equipped with an Ultrashield magnet. The $CDCl_3$ contained traces of tetramethylsilane (TMS), which was used as an internal reference. For classifying the signals in the *^1H NMR spectra* abbreviations such as s (single), d (double), m (multiple), br (broad) are used.

The molecular weights and polydispersity indices of the polymers were determined by *size exclusion chromatography (SEC)* using equipment supplied by Polymer Standards Service (PSS). All measurements were carried out at room temperature using Styragel HR 3 and Styragel HR 4 columns. The mobile phase was THF, delivered at a flow rate of 1 mL min^{-1} using a Waters 515 isocratic pump. The refractive index was measured with a Waters 2414 refractive index detector supplied by Polymer Standards Service (PSS). The instrumentation was calibrated using poly(methyl methacrylate) (PMMA) standards with narrow polydispersity indices (MWs of 102, 450, 670, 1580, 4200, 14400, 31000, 65000, 126000, 270000, 446000, 739000 g mol^{-1}) supplied by Polymer Standards Service (PSS).

Differential scanning calorimetry (DSC) was used to measure the glass transition temperatures (T_gs) of the homopolymers, random and block copolymers using a Q100 TA Instrument with a heating rate of 10 ºC min^{-1}. Each sample was scanned two times between -100 and +150 ºC. The second run (heat) was used for data analysis.

Thermal gravimetric analysis (TGA) measurements were performed on a Q 500 under argon at a heating rate of 10 ºC min^{-1}.

Dynamic Light Scattering (DLS) measurements were carried out using a DLS 90Plus Brookhaven light scattering spectrometer operating at 633 nm (power: 30 mW). DLS experiments were performed at a 90^o scattering angle. Solution concentrations varied between

4g/L and 1g/L. All polymer solutions were filtered through PTFE microfilters (pore size: 0.45 μm) prior to measurements.

UV-*Vis* spectra were recorded in solution at room temperature using a dual-beam grating spectrophotometer (Jasco V-630) with a 1 cm quartz cell. Measurements were carried out in *n*-hexane, THF and chloroform.

Fluorescence emission spectra of the anthracene-containing polymers prepared in the present study, were recorded in chloroform by using a Jasco 6300 spectrofluorimeter. The excitation wavelength was set at 368 nm. The polymer concentration in solution was $1x10^{-4}$ M (polymer concentration based on anthracene groups). Fluorescence measurements were carried out in the presence of: (a) thriethylamine (concentration range: 3.6 mM – 1 M) and (b) $FeCl_3.6H_2O$ (concentration range: 12.3 and 18.5 mM)

Dilute sample solutions were spin-coated on a mica surface and the surface topography images were obtained using *Atomic Force Microscope* in tapping mode with the constant force method (the force between the sample surface and the AFM tip being kept constant by a feedback system while the surface beneth the tip was scanned). The samples were imaged with the aid of MultiMode Scanning Probe Microscopy (Veeco), using a Nanoscope IIIa controller and a 120μm×120μm magnet -free scanner (Model AS-130VMF) developed by Digital Instruments with vertical range 5 μm and z-axis resolution 0.05 nm. The scan rate was 1 Hz. The cantilever's spring constant was 40 N/m. The shape of the silicon nitride tips was square pyramidal with radius of curvature ~10nm and half angle ~150^o. The images were processed with a linear plane fit in order to remove any sample tilt on them. The AFM measurements were carried out at the Institute of Chemical Engineering and High Temperature Chemical Processes, Foundation for Research and Technology-Hellas (ICEHT-FORTH).

The morphology of the polymer-metal nanohybrids was investigated by *Transmission Electron Microscopy* (TEM) using 1010 JEOL microscope (200kV). The colloidal suspension of nanoparticles was dried on a carbon coated copper grid to allow the TEM investigation. The TEM studies were carried out at the National Insitute for Isotopic and Molecular Technologies Cluj-Napoca in Romania by Dr. Rodica Paula Turcu.

The nonlinear optical properties of the synthesized hybrid micellar systems have been studied by means of the *Z-scan* technique, employing both visible (532 nm) and infrared (1064 nm) laser pulses delivered from a 35 ps mode-locked Nd:YAG laser operating at a repetition rate between 1 and 10 Hz. For the measurements, different concentrations of Pd-containing

micellar systems in n-hexane and THF solutions have been prepared while Z-scan measurements have been performed at various incident laser energies, by placing the samples into 1 mm thick quartz cells. These meausurements were performed at ICEHT-FORTH, in the group of the Professor S. Couris.

Nanowires were grown in the Nanostructured Materials Laboratory (by Prof. M. Zervos) using a 1″ Horizontal Atmospheric Pressure Chemical Vapor Deposition (APCVD) system by Atomate US which conists of four mass flow controllers and is capable of reaching a temperatures of 1100 ^{o}C. Atmospheric Pressure Chemical Vapor Deposition (APCVD) is a chemical process used to produce high-purity, high-performance solid materials. The process is often used in the semiconductor industry to produce thin films of metal oxides. In a typical APCVD process, the wafer (substrate) is exposed to one or more volatile precursors, which react and/or decompose on the substrate surface to produce the desired deposit at atmospheric pressure. The morphology of the obtained nanowires were examined with by Tescan *Scanning Electron Microscope* (SEM) while their crystal structure and the phase purity were investigated using SHIMADZU, XRD-600 with a Cu-Ka source by performing a scan of θ-2θ in the range between 10-80^{o}. Finally, photoluminescence (PL) measurements were carried out using a Ti-Sapphire ultrafast laser amplifier generating 75 fs pulses at repetition rate of 250 kHz.

3.3 Synthesis of cumyl dithiobenzoate, CDTB (Chain Transfer Agent, CTA)

For the synthesis of the homopolymers, random and diblock copolymers by RAFT controlled radical polymerization the use of the so-called “chain transfer agent” is essential so as for the polymerization to take place in a controlled manner. Therefore firstly, the cumyl dithiobenzoate, a well-known CTA used in the RAFT process, was synthesized and characterized. The synthetic procedure followed is described as below:

CDTB was synthesized in two steps [139]. Briefly, the procedure involved the preparation of dithiobenzoic acid and its subsequent reaction with α-methylstyrene to obtain CDTB. Specifically, benzyl chloride was added dropwise within an hour, to a stirring mixture of methanol (50 mL), sulfur (6.4g) and sodium methoxide (25% in methanol, 43.2g or 45.7 mL), under dry nitrogen atmosphere and at room temperature. Subsequently, the reaction mixture

was heated at 70^{o}C for 16 hours. Then, the mixture was allowed to cool down to room temperature, filtered (separation of NaCl) and the solid was washed with methanol (20 mL).

The combined filtrate was concentrated on a rotary evaporator until complete removal of methanol. After that, water (100 mL) was added to re-dissolve the brown colour mixture. The brownish colour aqueous solution was extracted 3 times with diethyl ether (3x50 mL). The obtained aqueous phase was acidified with concentrated HCl (37%) after having placed a layer of diethyl ether (50 mL) on top of the aqueous layer in the extraction funnel. This procedure continued until the aqueous phase was discolorated. Then, the organic layer was extracted with a NaOH solution (1 M, 3x50 mL).

Finally the organic layer was separated and dried with anhydrous magnesium sulfate. The solvent was removed under reduced pressure and dithiobenzoic acid was obtained as a dark purple oil (yield of the crude product: 8.7g, 56.5%).

The product was used in the second stage without further purification. Because of the high instability of the product, the second step was carried out immediately after isolation of dithiobenzoic acid. A mixture of dithiobenzoic acid (8.7 g, mmol), α-methyl styrene (8.87 g, mmol) and CCl_4 (40 mL) was heated at 70^{o}C for 18 hrs. The solvent and excess monomer were removed on a rotary evaporator and the residue was purified by column chromatography (silica gel) using *n*-hexane as eluent to give CDTB (2.97 g, 19.3% yield) as a dark purple oil. The product was left to dry for 24 h in a vacuum oven and stored in the freezer.

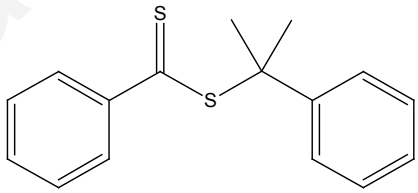

^{1}H NMR (300MHz, $CDCl_3$) δ (ppm): 7.87 (d, 2H), 7.58-7.22 (m, 8H), 2.01 (s, -CH_3).

3.4 Lauryl-containing polymers

3.4.1 Synthesis of $LauMA_x$ homopolymers

The polymerization followed for the preparation of a $LauMA_x$ homopolymer (asumming 100% conversion) is described as follows: CDTB was dried under high vacuum for approximately 30 min prior to use. In a round-bottom flask maintained under a dry nitrogen atmosphere, freshly distilled LauMA (9.0 mL, 31.0 mmol) was added. CDTB (100 mg, 0.367 mmol) and AIBN (33.0 mg, 0.201 mmol) were dissolved in freshly distilled benzene (2.2 mL) and were transferred into the flask together with the aid of a syringe. Subsequently, the resulting solution was degassed by three freeze–evacuate–thaw cycles, placed under a dry nitrogen atmosphere and heated at 65 ^{o}C for 18 hours. The polymerization was terminated by cooling the reaction down to room temperature. The produced $LauMA_x$ (6.99 g, 89.5% polymerization yield) was retrieved by precipitation in methanol and was left to dry *in vacuo* at room temperature for 24 hours.

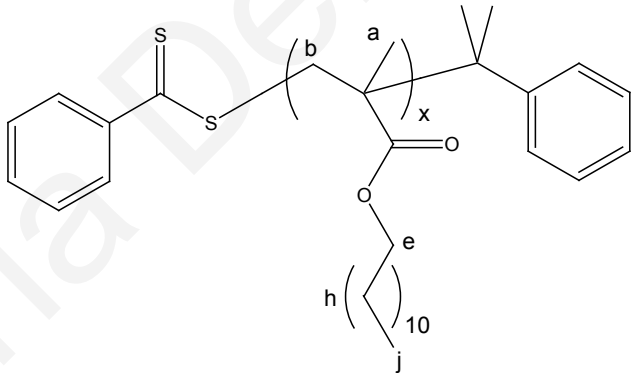

^{1}H NMR (300MHz, $CDCl_3$) δ (ppm): 3.90 (br, -CH_2O (e)), 2.17-1.6 (br, -CH_2 (b)), 1.27-1.02 (br, -CH_3 and -CH_2 (a, h))0.8 (br, -CH_3 (j))

3.4.2 Synthesis of $LauMA_x$-b-$AEMA_y$ diblock copolymers

The preparation of functional diblock copolymers bearing *β*-ketoester moieties has been carried out *via* RAFT polymerization in a two step procedure. The first step involved the

synthesis of $LauMA_x$ homopolymers which were subsequently used as macro-CTAs for the polymerization of AEMA, to prepare well-defined $LauMA_x$-b-$AEMA_y$ diblock copolymers. Chain growth of the obtained $LauMA_x$ homopolymers was accomplished *via* the addition of the second monomer AEMA. The synthetic methodology followed for the preparation of a $LauMA_x$-b-$AEMA_y$ diblock copolymer is described as follows: The macro-chain transfer agent (macro-CTA), $LauMA_{75}$, (M_n^{SEC}=19100 $g.mol^{-1}$, 1 g, 0.052 mmol) was placed in a round-bottom flask and dissolved in freshly distilled ethyl acetate (1.5 ml) under a dry nitrogen atmosphere. AIBN (3.0 mg, 0.018 mmol) dissolved in ethyl acetate and AEMA (0.5 ml, 3.0 mmol) were then transferred into the flask *via* a syringe. The reaction mixture was degassed by three freeze–evacuate–thaw cycles and placed under a dry nitrogen atmosphere at 65 ^oC for 18 hours. The polymerization was terminated by cooling the reaction down to room temperature. The produced diblock copolymer (1.46 g, 94% polymerization yield) was retrieved by precipitation in methanol and was left to dry *in vacuo* at room temperature for 24 hours.

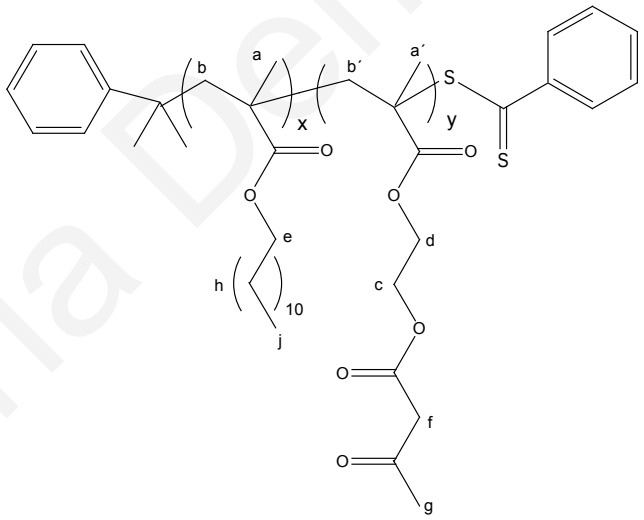

^{1}H NMR (300MHz, $CDCl_3$) δ (ppm): 4.36 (br, -CH_2 (c)), 4.16 (br, -CH_2 (d)), 3.91 (br, -CH_2 (f)), 3.47 (br, -CH_2 (e)), 2.29 (br, -CH_3 (g)), 1.60 (br, -CH_2 (b, b´)), 1.26 (br, -CH_2 (h)), 1.23 (br, -CH_2 (b´)), 0.87 (br, -CH_3 (a, a´, j)).

3.5 Carbazole-containing polymers

3.5.1 Synthesis of 2-(N-carbazolyl) ethyl methacrylate (CbzEMA)

The synthesis of CbzEMA was succeeded in two steps by following a modified methodology based on previous reports [140]. Firstly, 2-(N-carbazolyl) ethanol was synthesized and it was then modified into 2-(N-carbazolyl) ethyl methacrylate as follows: A solution of carbazole (19 g, 0.114 mol) and ethylene carbonate (11 g, 0.125 mol) in dimethylformamide (DMF) was placed under reflux for 8 hours in the presence of KOH (1.9 g). After been cooled to room temperature, the reaction mixture was filtered and then poured into a large amount of water (4 L). The precipitated white crystalline 2-(N-carbazolyl) ethanol (yield: 38%) was collected and dried in a vacuum oven for 12h at 40^{o}C. Subsequently, it was purified twice by recrystallization in a 1:1 (v/v) benzene/cyclohexane mixture. The obtained 2-(N-carbazolyl) ethanol (5 g, 0.024 mol) was then dissolved in dichloromethane (80 ml). In the reaction flask, triethylamine (2.8 ml, 0.028 mol) and methacryloyl chloride (4 ml, 0.028 mol) were added in a 20% excess, for a more quantitative reaction. The methacryloyl chloride was added dropwise during stirring at 0^{o}C. During the addition of the last component an exotherm was observed and sediment was formed, namely hydrochloric triethylamine (Et_3NHCl), which is a byproduct of the reaction. The reaction mixture was stirred for additional 24h. The hydrochloric triethylamine was filtered by using a glass frit filter and removed from the reaction mixture. After filtration, 10 ml of water were added for the hydrolysis of the methacryloyl chloride (excess) into methacrylic acid and the segregation of the organic phase from the aqua. The product remained in the organic phase. Subsequently, dichloromethane (40 ml) was added in the solution and the mixture was extracted two times with water (5 and 10 ml), then three times with $NaHCO_3$ solution (5% in water, addition of 5ml each time) and again three times with water. The monomer was purified twice by recrystalization in methanol (yield: 42%).

For the preparation of the 2-(N-carbazolyl) ethanol, a different procedure was also carried out as follows [140b]: Carbazole (19 g, 0.114 mol) and ethylene carbonate (11 g, 0.125 mol) were left to react under reflux in DMF for 8 hours in the presence of NaOH (0.5 g). After the reaction mixture was cooled down to room temperature, toluene (50ml) was added and transferred in a beaker with distilled water (1600ml), under stirring. When the stirring was

stopped, two layers appeared. The product was trapped in the organic layer; however its isolation presented difficulties.

^{1}H NMR (300MHz, $CDCl_3$) δ (ppm): 8.1 (d, -Ph), 7.46 (m, -Ph), 7.24 (m, -Ph), 5.92 (s, $=CH_2$), 5.48 (s, $=CH_2$), 4.64 (t, $N–CH_2$), 4.53 (t, $O–CH_2$), 1.94 (s, CH_3).

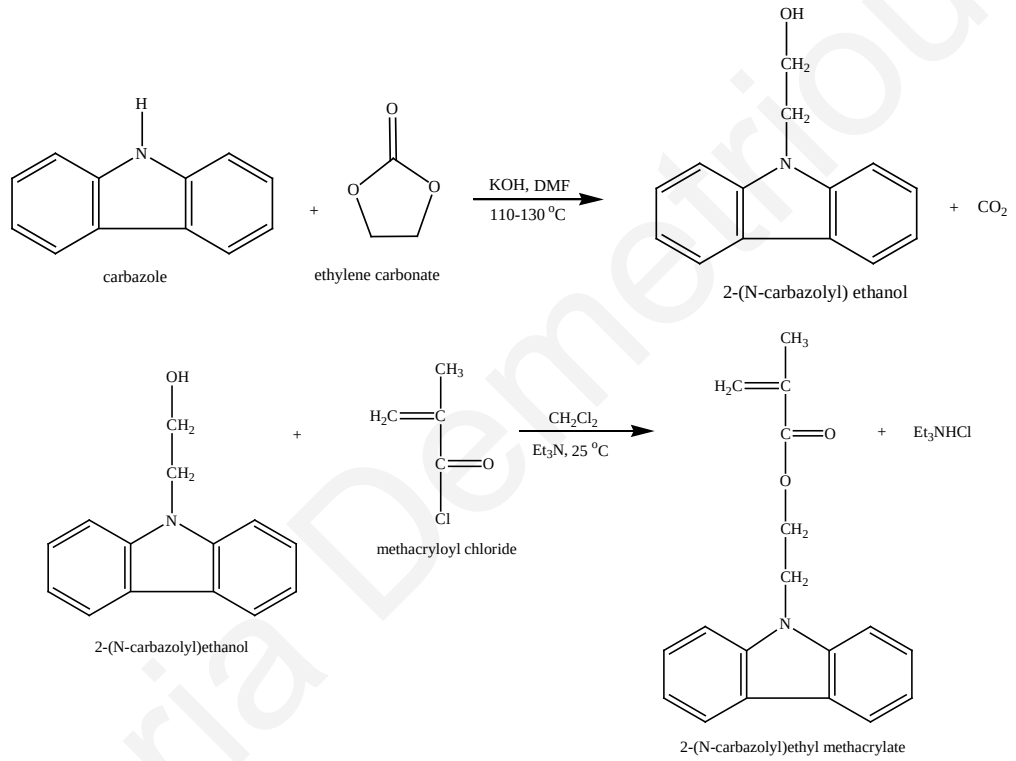

Figure 3.1: *Synthesis scheme followed for the preparation of the CbzEMA monomer.*

3.5.2 Synthesis of $CbzEMA_x$ homopolymers

The RAFT polymerization process followed for the preparation of the $CbzEMA_x$ homopolymer (assuming 100% conversion) is described as follows: CbzEMA (733 mg, 2.63 mmol) was placed in a round-bottom flask and dissolved in freshly distilled benzene (0.7 ml) under a dry nitrogen atmosphere. CDTB (7.2 mg, 0.026 mmol) and AIBN (2.36 mg, 0.014

mmol) were dissolved in benzene and were then transferred into the flask *via* a syringe. The reaction mixture was degassed by three freeze–evacuate–thaw cycles and placed under a dry nitrogen atmosphere at 65 ^{o}C for 20 hours. The polymerization was terminated by cooling the reaction down to room temperature. The produced homopolymer (555 mg, 76% polymerization yield) was retrieved by precipitation in methanol and was left to dry *in vacuo* at room temperature for 24 hours.

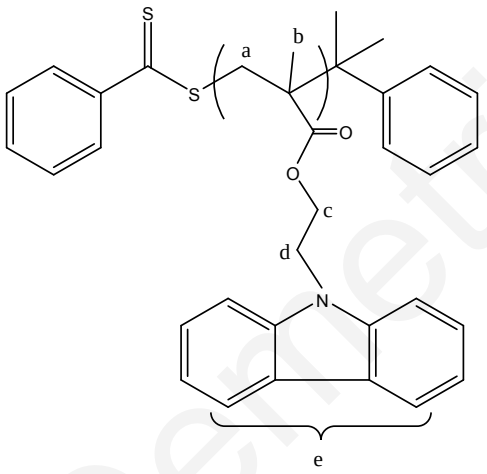

^{1}H NMR (300MHz, $CDCl_3$) δ (ppm): 7.1-7.9 (m, -Ph, (e)), 4.15 (br, N-CH_2, (d)), 3.98 (br, O-CH_2, (c)), 1.6 (br, -CH_2, (a)), 0.86 (m, -CH_3, (b)).

3.5.3 Synthesis of CbzEMA$_x$-b-AEMA$_y$ diblock copolymers

The general procedure followed for the preparation of the CbzEMA$_x$-b-AEMA$_y$ diblock copolymers was similar to that employed in the case the LauMA$_x$-b-AEMA$_y$ diblock copolymers. In a round-bottom flask, the macro-CTA, CbzEMA$_{82}$, (M_n^{SEC}=23075 g.mol^{-1}, 493 mg, 0,020 mmol) was placed and dissolved in freshly distilled tetrahydrofuran (0.9 ml) under a dry nitrogen atmosphere. AIBN (1.6 mg, 0.0096 mmol) dissolved in THF and AEMA (0.2 ml, 0.99 mmol) were then transferred into the flask *via* a syringe. The reaction mixture was degassed by three freeze–evacuate–thaw cycles and placed under a dry nitrogen atmosphere at 65 ^{o}C for 20 hours. The polymerization was terminated by cooling the reaction down to room temperature. The produced diblock copolymer (603 mg, 36% polymerization yield) was

retrieved by multiple precipitation steps in methanol and was left to dry *in vacuo* at room temperature for 24 hours.

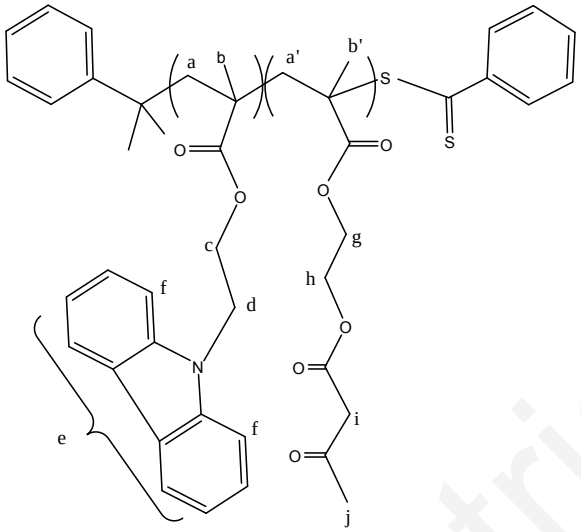

^{1}H NMR (300MHz, $CDCl_3$) δ (ppm): 7.9 (br, -Ph, (f)), 7-7.2 (-Ph (e)), 4.35 (br, -CH_2 (i)), 4.18 (br, N-CH_2 (d)), 3.97 (br, O-CH_2 (c)), 3.75 (br, -CH_2 (h)), 3.56 (br, -CH_2 (g)), 2.29 (br, -CH_3 (j)), 0.86-2.00 (-CH_2, -CH_3 (a, a΄,b, b΄))

3.6 Anthracene-containing polymers

3.6.1 Synthesis of 9-anthrylmethyl methacrylate (AnMMA)

Two procedures were followed for the synthesis of the AnMMA. In the first procedure [140], anthracenemethanol (5 g, 0.024 mol) was dissolved in dichloromethane (160 ml). Afterwards, triethylamine (3.89 ml, 0.028 mol) and methacryloyl chloride (2.71 ml, 0.028 mol) were added in a 20% excess, in the reaction flask. The methacryloyl chloride was added dropwise during stirring at 0^{o}C. The reaction mixture was stirred for 24 hours. The mixture was filtered by using a glass frit filter in order to remove the hydrochloric triethylamine. After filtration, 10 ml of water were added for the hydrolysis of methacryloyl chloride (excess) into methacrylic acid and the segregation of the organic phase from the aqua. The product remained in the organic phase. Subsequently, dichloromethane (40 ml) were added in the solution and the mixture was extracted two times with water (5 ml and 10 ml), then three times with $NaHCO_3$ solution (5% in water, addition of 5 ml each time) and again three times with water. The

extraction was dried with $MgSO_4$ and the solvent was removed under reduced pressure. The residue was an orange viscous liquid. The product (pale yellow solid) was obtained by recrystallization in methanol and left to dry for 24 hours in a vacuum oven. The yield of the reaction was very low (~5%), therefore a second procedure was followed for the preparation of AnMMA [141]. Anthracenemethanol (3 g, 0.014 mol) was dissolved in THF (12 ml). Subsequently, triethylamine (3 ml, 0.016 mol), pyridine (2 ml, 0.016 mol) and methacryloyl chloride (2.1 ml, 0.016 mol) were added in a 20% excess, in the reaction flask. The methacryloyl chloride was added dropwise during stirring at 0^oC. After addition, the mixture was left to warm up to room temperature and stirred for 1 hour. Water (10 ml) was added and the mixture was extracted with diethyl ether. The organic phase was then extracted with HCl (1 M, 3 x 5 ml), then with $NaHCO_3$ solution (5% in water, 3 x 5 ml) and with a saturated NaCl solution (3 x 5 ml). Afterwards, the organic phase was isolated, dried over $MgSO_4$ and after filtration the solvent was removed under reduced pressure and the product was recrystallized from methanol (yield: 42%).

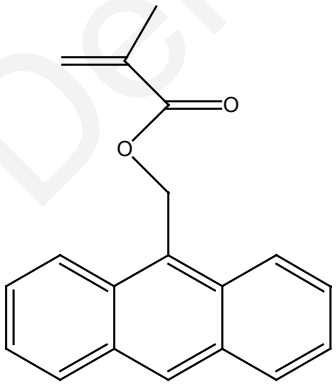

^{1}HNMR (300MHz, $CDCl_3$) δ (ppm): 7.2-8.5 (m, -Ph), 6.2 (s, $-CH_2Ph$), 6.05 (s, -Ph), 5.50 (s, -Ph), 5.30 (s, $=CH_2$), 3.49 (s, $=CH_2$), 2.17 (s, $-CH_2$), 1.9 ($-CH_3$).

3.6.2 Synthesis of $AnMMA_x$ homopolymers

A typical procedure for the synthesis of an $AnMMA_x$ homopolymer (assuming 100% conversion) is described as follows: AnMMA (800 mg, 2.87 mmol) was placed in a round-

bottom flask and dissolved in freshly distilled benzene (1.2 ml) under a dry nitrogen atmosphere. Cumyl dithiobenzoate (CDTB) (7.89 mg, 0.029 mmol) and AIBN (2.61 mg, 0.016 mmol) dissolved in benzene, were then transferred into the flask *via* a syringe. The reaction mixture was degassed by three freeze–evacuate–thaw cycles and placed under a dry nitrogen atmosphere at 65 ^{o}C for 20 hours. The polymerization was terminated by cooling the reaction down to room temperature. The produced homopolymer (300 mg, 37.5 % polymerization yield) was retrieved by precipitation in methanol and was left to dry *in vacuo* at room temperature for 24 hours.

The synthesis of the $AnMMA_x$ was also carried out using 2-cyano-2-propylbenzodithioate (CPDTB) (6.4 mg, 0.029 mmol) as the CTA by following the same experimental conditions (718.7 mg, 89.8 % polymerization yield).

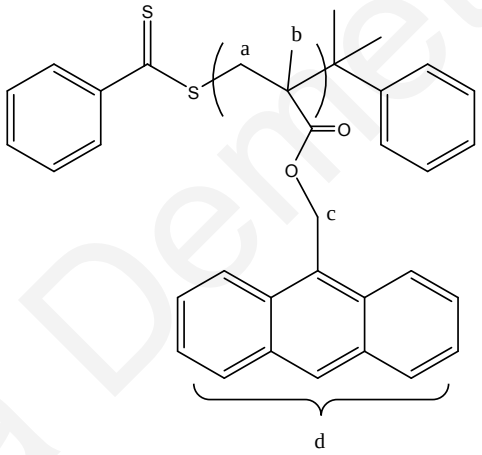

^{1}H NMR (300MHz, $CDCl_3$) δ (ppm): 7.2-8.5 (m, br, -Ph, (d)), 6.2 (br, -CH_2Ph, (c)), 1.99-0.7 (-CH_2, -CH_3, (a, b))

The copolymerization of the $AnMMA_x$ homopolymer with AEMA was not successful in the case where $AnMMA_x$ was used as the macro-CTA. For that reason, two AEMA macro-CTAs were synthesized and further used in the copolymerization with the AnMMA.

3.6.3 Synthesis of $AEMA_x$ homopolymers

The methodology for the synthesis of an $AEMA_x$ homopolymer (assuming 100% conversion) is as follows: AEMA (2.7 ml, 14 mmol) was placed in a round-bottom flask under a dry nitrogen atmosphere. CDTB (127.1 mg, 0.466 mmol) and AIBN (14 mg, 0.086 mmol) were dissolved in ethyl acetate and transferred into the flask *via* a syringe. The reaction mixture was degassed by three freeze–evacuate–thaw cycles and placed under a dry nitrogen atmosphere at 65 ^{o}C for 20 hours. The polymerization was terminated by cooling the reaction down to room temperature. The produced homopolymer (2.48 g, 85% polymerization yield) was retrieved by precipitation in methanol and was left to dry *in vacuo* at room temperature for 24 hours.

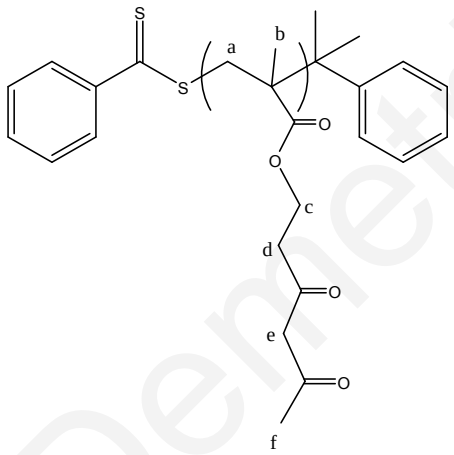

^{1}HNMR (300MHz, $CDCl_3$) δ (ppm): 11.90 (s, -OH (enol)), 5.10 (br, s, =CH (enol)), 4.2 (s, -CH_2, (e)), 4.08 (s, -CH_2, (c)), 3.6 (s, -CH_2, (d)), 1.8 (s, -$COCH_3$, (f)), 1.74-0.76 (br, -CH_2, -CH_3, (a, b)).

3.6.4 Synthesis of $AEMA_x$-b-$AnMMA_y$ diblock copolymers

The general procedure followed for the preparation of the $AEMA_x$-b-$AnMMA_y$ diblock copolymers was the same as that already described for the $LauMA_x$-b-$AEMA_y$ and $CbzEMA_x$-b-$AEMA_y$ diblock copolymers. In a round-bottom flask, the macro-CTA, $AEMA_{42}$ (M_n^{SEC}=9235 g.mol^{-1}, 200 mg, 0.022 mmol) was placed under a dry nitrogen atmosphere. AIBN (1.6 mg, 0.0096 mmol) and AnMMA (1.08 g, 3.909 mmol) dissolved in THF were then transferred into the flask *via* a syringe. The reaction mixture was degassed by three freeze–evacuate–thaw cycles and placed under a dry nitrogen atmosphere at 62 ^{o}C for 20 hours. The

polymerization was terminated by cooling the reaction down to room temperature. The produced diblock copolymer (17% polymerization yield) was retrieved by multiple precipitation steps in methanol and was left to dry *in vacuo* at room temperature for 24 hours.

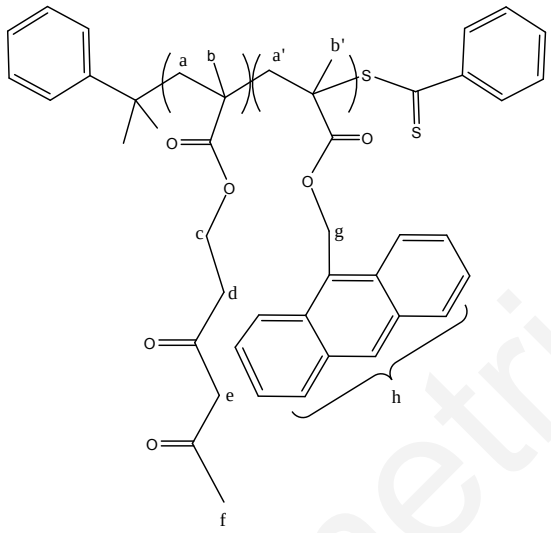

^{1}HNMR (300MHz, $CDCl_3$) δ (ppm): 11.90 (s, -OH (enol)), 7.16-8.03 (br, -Ph, (h)), 4.35 (s, -CH_2, (g)), 4.16 (s, -CH_2, (c)), 3.56 (s, -CH_2, (d)), 2.35 (s, -$COCH_3$, (f)), 0.85-1.74 (br, -CH_2,-CH_3, (a, b, a´, b´)).

3.7 Preparation of polymer-metal nanohybrids

3.7.1 Palladium-containing nanohybrids

a. LauMA$_x$-*b*-AEMA$_y$/Pd(^{0})

A typical methodology followed for the preparation of LauMA$_x$-*b*-pAEMA$_y$/Pd(^{0}) micellar hybrids in n-hexane is described as follows: 20 mg of LauMA$_{120}$-b-AEMA$_{67}$ (20 mg, 0.0297 mmol of AEMA units) was dissolved in *n*-hexane (5 mL). After complete dissolution of the polymer, triethylamine (80 μL) was added to the solution. Subsequently, the resulting solution was mixed with Pd($CH_3COO)_2$ (3.3 mg, 0.015 mmol) and left to stir at room temperature until complete solubilization of the salt. Upon complexation and solubilization the colour of the solution changed from white to yellow transparent. Finally, hydrazine monohydrate (40μL)

was added to the solution upon stirring. The reduction of Pd(II) ions to noble palladium was accompanied by a colour change of the solution from yellow to dark brown.

Table 3.1: *The quantities of the reactants (polymer, Pd(II) salt) used for the preparation of the $LauMA_x$-b-$AEMA_y$/Pd(^{0}) nanohybrids.*

POLYMER	AEMA Units (mmol)	$Pd(CH_3COO)_2$ (mg)	$Pd(CH_3COO)_2$ (mmol)	[AEMA]:[Pd(II)]
$LauMA_{75}$-b-$AEMA_{46}$	0.0318	3.6	0.016	2:1
$LauMA_{120}$-b-$AEMA_{67}$	0.0297	3.3	0.015	2:1
$LauMA_{50}$-b-$AEMA_{9}$	0.0122	1.4	0.006	2:1
$LauMA_{271}$-b-$AEMA_{81}$	0.0184	2.1	0.009	2:1

b. $CbzEMA_x$-*b*-$AEMA_y$/Pd(^{0}) nanohybrids

Table 3.2: *Quantities of the reactants (polymer, Pd(II) salt) used for the preparation of $CbzEMA_x$-b-$AEMA_y$/Pd(^{0}) nanohybrids.*

POLYMER	AEMA Units (mmol)	$Pd(CH_3COO)_2$ (mg)	$Pd(CH_3COO)_2$ (mmol)	[AEMA]:[Pd(II)]
$CbzEMA_{82}$-*b*-$AEMA_{47}$	0.0284	6.4	0.0284	1:1
		3.2	0.0142	2:1
$CbzEMA_{104}$-*b*-$AEMA_{44}$	0.0228	5.1	0.0228	1:1
		2.6	0.0114	2:1
$CbzEMA_{38}$-*b*-$AEMA_{50}$	0.0463	10.4	0.0463	1:1
		5.2	0.0232	2:1
$CbzEMA_{38}$-*b*-$AEMA_{10}$	0.0154	3.4	0.0154	1:1
		1.7	0.0077	2:1

The general procedure, followed for the preparation of the $CbzEMA_x$-*b*-$AEMA_y/Pd(^0)$ nanohybrid systems, is similar to that already described for the preparation of $LauMA_x$-$AEMA_y/Pd(^0)$. $CbzEMA_{82}$-*b*-$AEMA_{47}$ (20 mg, 0.0284 mmol of the AEMA units) was dissolved in THF (5 ml). After complete dissolution of the polymer, triethylamine (80 μL) was added to the solution. Subsequently, the resulting solution was mixed with $Pd(CH_3COO)_2$ (3.2 mg, 0.0142 mmol) and left to stir at room temperature. Finally, hydrazine monohydrate (40 μL) was added to the solution upon stirring. The reduction of Pd(II) ions to noble palladium was accompanied by a colour change of the solution from yellow to dark brown.

c. $AnMMA_x$-*b*-$AEMA_y/Pd(^0)$ nanohybrids

The general procedure followed for the preparation of the $AEMA_x$-$AnMMA_y$ nanohybrids is similar to that already described previously for the $CzEMA_x$-*b*-$AEMA_y/Pd(^0)$ nanohybrid systems. $AEMA_{42}$-$AnMMA_{83}$ (20 mg, 0.0265 mmol of the AEMA units) was dissolved in THF (5 ml). After complete dissolution of the polymer, triethylamine (80 μL) was added to the solution. Subsequently, the resulting solution was mixed with $Pd(CH_3COO)_2$ (3 mg, 0.017 mmol) and left to stir at room temperature. Finally, hydrazine monohydrate (40 μL) was added to the solution upon stirring. The reduction of Pd(II) ions to noble palladium was accompanied by a colour change of the solution from yellow to dark brown.

Table 3.3: *Quantities of the reactants (polymer, Pd(II) salt) used for the preparation of* $AEMA_x$-*b*-$AnMMA_y/Pd(^0)$ *nanohybrids.*

POLYMER	AEMA Units (mmol)	$Pd(CH_3COO)_2$ (mg)	$Pd(CH_3COO)_2$ (mmol)	[AEMA]:[Pd(II)]
$AEMA_{42}$-$AnMMA_{83}$	0.0265	3.0	0.0131	2:1
$AEMA_{42}$-$AnMMA_{113}$	0.0251	2.8	0.0126	2:1
$AEMA_{21}$-$AnMMA_{43}$	0.0256	2.9	0.0126	2:1

3.7.2 Gold-containing nanohybrids

A typical methodology followed for the preparation of the LauMA$_x$-*b*-pAEMA$_y$/Au nanohybrid systems in *n*-hexane is described as follows: LauMA$_{277}$-b-AEMA$_{81}$ (179 mg, 0.1648 mmol of AEMA units) was dissolved in *n*-hexane (10 ml). After complete dissolution of the polymer, triethylamine (80 μL) was added to the solution. Subsequently, the resulting solution was mixed with $HAuCl_4.3H_2O$ (6.5 mg, 0.017 mmol) and left to stir at room temperature until complete solubilization of the salt. The generation of gold nanoparticles was accompanied by a colour change from white to pink-purple transparent. The solution was then filtered for the removal of any uncomplexed $HAuCl_4.3H_2O$ and the triethylamine hydrochloride salt (reaction by-product).

Table 3.4: *Quantities of the reactants (polymer, $HAuCl_4.3H_2O$ salt) used for the preparation of LauMA$_x$-b-AEMA$_y$/Au nanohybrids.*

Polymer	Polymer Mass (mg)	AEMA Units (mmol)	$HAuCl_4.3H_2O$ (mg)	$HAuCl_4.3H_2O$ (mmol)	[AEMA]:[Au]
LauMA$_{277}$ -b- AEMA$_{81}$	179	0.1648	5.0	0.0165	10:1
LauMA$_{277}$ -b- AEMA$_{81}$	114	0.1048	4.1	0.0105	10:1
LauMA$_{50}$ -b -AEMA$_9$	114	0.0677	2.7	0.0068	10:1

3.8 Metal Oxide Nanowire Growth

For the metal oxide (*β*-Ga_2O_3, ZnO) nanowire growth preliminary experiments involved the deposition of LauMA$_x$-*b*-AEMA$_y$/Pd(^{0}) and LauMA$_x$-*b*-AEMA$_y$/Au solutions prepared as described in 3.7.1.a and 3.7.2 of various concentration on p^+ Si(001) substrates *via* spin-coating or drop casting. The experimental conditions followed for the deposition by spin-coating are provided in Table 3.5.

β-Ga_2O_3 NW growth was carried out as follows: 0.1-0.2 g of Ga were used while square pieces of Si(001)≈ 7 x 7 mm^2 with the Au or Pd MNPs were loaded only a few mm's away from the Ga inside a quartz boat which was positioned directly above the thermocouple used

to measure the heater temperature (T_H). After loading, 500 sccm's of Ar was allowed to flow for 10 min. Then the temperature was ramped to 900 ^oC under a reduced flow temperature of 100 sccm's of Ar at 30 ^oC/min. Upon reaching 900 ^oC the same flow of Ar was maintained for various times between 5-60 min after which the tube was allowed to cool down using the same gas flows during growth. The sample was removed only when the temperature was lower than 100 ^oC. Similarly, ZnO NWs were grown by reactive vapor transport using 0.2 g Zn under an inert flow of 100 sccms of Ar at 550 ^oC for 60 min.

Table 3.5: *Spin-coating conditions and polymer solution concentration for the $LauMA_{50}$-b-$AEMA_9$/Au and $LauMA_{50}$-b-$AEMA_9$/Pd micellar systems. These were spin coated on p^+ Si(001) using 50 μL of solution.*

Speed/Time (rps:sec)	**$LauMA_{50}$-*b*-$AEMA_9$/Au (mg/L)**		**$LauMA_{50}$-*b*-$AEMA_9$/Pd(^{0}) (mg/L)**	
250:20	1393	CVD933		
250:20	2785	CVD934		
250:20	5570	CVD935		
250:20	11400	CVD936		
250:20	696	CVD937	700	CVD970
200:20	696	CVD938	700	CVD962
150:20	696	CVD939	700	CVD971
100:20	696	CVD940	700	CVD972
50:20	696	CVD941	700	CVD973
250:20	69.6	CVD995	70	CVD998
250:20	6.96	CVD996	7	CVD998
250:20	0.696	CVD997	0.7	CVD1000

4. RESULTS AND DISCUSSION

In this chapter, the obtained results related to the synthesis and characterization (molecular, thermal, aggregation behavior) of the three block copolymer families are presented and discussed. Furthermore, results related to the NLO response of the polymer-metal micellar nanohybrid systems as well as to their ability to act as nanocatalysts for the growth of metal oxide nanowires are presented. Finally, the applicability of the antrhacene-containing BCs toward fluorescence chemical sensing in solution is also discussed.

4.1 Synthesis and Characterization

4.1.1 LauMA$_x$-b-AEMA$_y$ Amphiphilic Diblock Copolymers

4.1.1.1 Synthesis and Molecular Characterization [142]

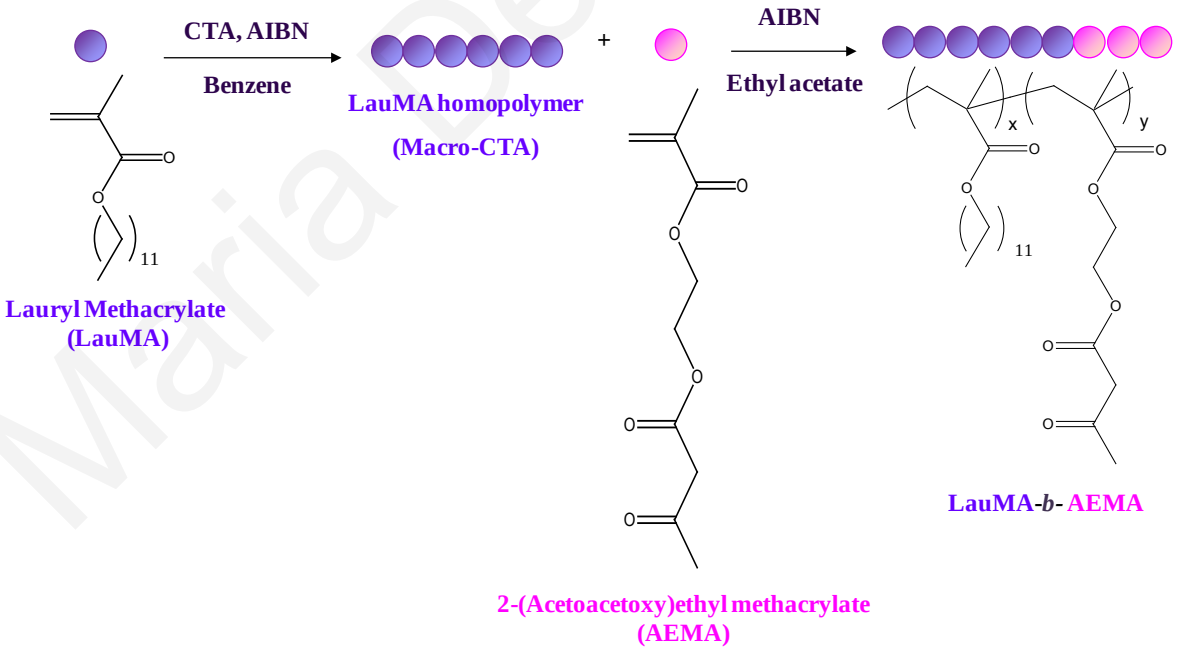

Figure 4.1: *Schematic representation of the synthetic procedure followed for the preparation of the LauMA$_x$-b-AEMA$_y$ diblock copolymers.*

A series of well-defined $LauMA_x$ homopolymers and $LauMA_x$-*b*-$AEMA_y$ block copolymers were successfully synthesized *via* RAFT polymerization following typical methodologies already described in the experimental section. The block copolymer synthesis involved the post-growth of AEMA onto a $LauMA_x$ homopolymer chain used as a macro-CTA, as schematically presented in Fig. 4.1.

The products were characterized by means of SEC and ^{1}H NMR in order to obtain information on their molecular characteristics. Table 4.1 summarizes the molecular weight (MW) and composition characteristics as determined by SEC and ^{1}H NMR for the four homopolymers and the corresponding diblock copolymers synthesized in the present study.

Table 4.1: *Characteristics of the $LauMA_x$ and the corresponding $LauMA_x$-b-$AEMA_y$ diblock copolymers synthesized by RAFT (polymerization yields, MWs, PDIs and compositions).*

Experimental structure[a]	**Conversion (%)**	**Theor. MW**[b] **g mol^{-1}**	**SEC results**[c]		**AEMA (% content by ^{1}H NMR)**
			M_n	**PDI**	
$LauMA_{75}$	89.5	19126	19100	1.19	-
$LauMA_{75}$-*b*-$AEMA_{46}$	81	24301	30700	1.13	38
$LauMA_{120}$	90	31826	30700	1.07	-
$LauMA_{120}$-*b*-$AEMA_{67}$	68	40940	45100	1.16	36
$LauMA_{50}$	93	6878	12874	1.14	-
$LauMA_{50}$-*b*-$AEMA_{9}$	98	14715	14200	1.18	15
$LauMA_{277}$	97	64426	70725	1.16	-
$LauMA_{277}$-*b*-$AEMA_{81}$	92	78862	88750	1.27	21

[a]determined by SEC and ^{1}H NMR; [b][(g. monomer)/(mol RAFT agent)]x(polymerization yield) + MW of CTA (for homopolymers) and [(g. monomer)/(mol CTA agent)]x(polymerization yield) + M_n of macro-CTA (for diblock copolymers); [c]SEC calibrated with PMMA standards; M_n = number average molecular weight; PDI = polydispersity index; LauMA = lauryl methacrylate; AEMA = 2-(acetoacetoxy)ethyl methacrylate.

All polymers were characterized by narrow molecular weight distributions which varied between 1.07-1.27 and experimental molecular weights close to the theoretical ones. Figure 4.2 displays the SEC traces of the $LauMA_{120}$ homopolymer and the corresponding $LauMA_{120}$-

b-AEMA$_{67}$ diblock copolymer. The molecular weight distribution (MWD) of the latter is shifted towards higher MW$_s$ compared to that of the homopolymer, demonstrating the block efficiency from homopolymer to block copolymer. However, a small shoulder arising at higher MW$_s$, may indicate the existence of a small proportion of recombined polymer chains.

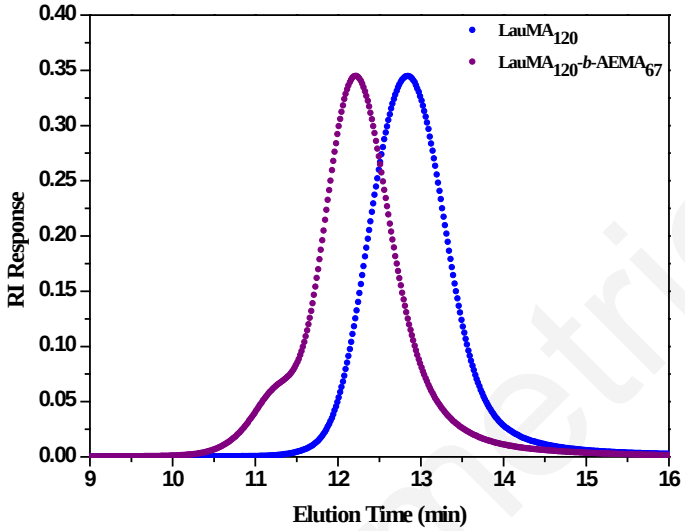

Figure 4.2: *SEC elugrams of LauMA$_{120}$ and LauMA$_{120}$-b-AEMA$_{67}$.*

^{1}H NMR spectroscopy confirmed the expected chemical structure of the LauMA$_x$-*b*-AEMA$_y$. Figure 4.3 presents the ^{1}H NMR spectrum of the LauMA$_{75}$-*b*-AEMA$_{46}$ diblock copolymer. The peak assignments are shown in the spectrum. The AEMA comonomer compositions shown in Table 4.1 were determined from the ratio of the areas under the characteristic signals of the LauMA and AEMA, appearing at 3.93 (e) and 2.27 (g) ppm respectively.

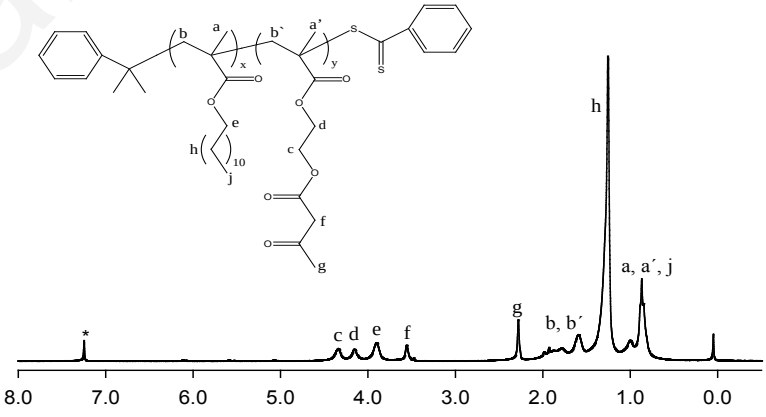

Figure 4.3: *^{1}H NMR spectrum of the LauMA$_{75}$-b-AEMA$_{46}$ block copolymer. * Solvent (CHCl$_3$).*

4.1.1.2 Thermal Properties [142]

The glass transition (T_g) and decomposition temperatures of the $LauMA_x$ homopolymers and the $LauMA_x$-*b*-$AEMA_y$ diblock copolymers were provided by DSC and TGA measurements, respectively. The T_g of the $LauMA_{75}$ homopolymer was determined to be -53 ^oC, which is close to literature values [143]. $LauMA_x$-*b*-$AEMA_y$ diblock copolymers exhibited two T_gs (~ -50 ^oC for the LauMA block and ~ -10 ^oC for the AEMA block (Fig. 4.4) indicating that microphase separation might occur between the two blocks. The fact that the T_g values of the block copolymer deviate from the corresponding homopolymers may suggest partial intermixing of the polymer segments.

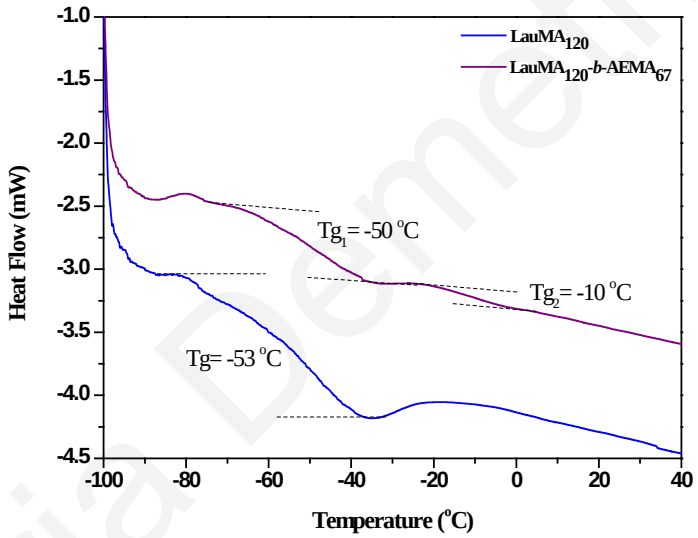

Figure 4.4: *DSC graphs of the $LauMA_{120}$ homopolymer and $LauMA_{120}$-b-$AEMA_{67}$ diblock copolymer.*

As far as the thermal stability of these systems is concerned, the polymers started loosing weight at ~ 100-150 ^oC and decompose loosing most of their weight between 250-300 ^oC (Fig. 4.5). Similar values (degradation temperature range 200-300 ^oC) were reported in literature for the degradation of copolymers based on methyl methacrylate and lauryl methacrylate [144].

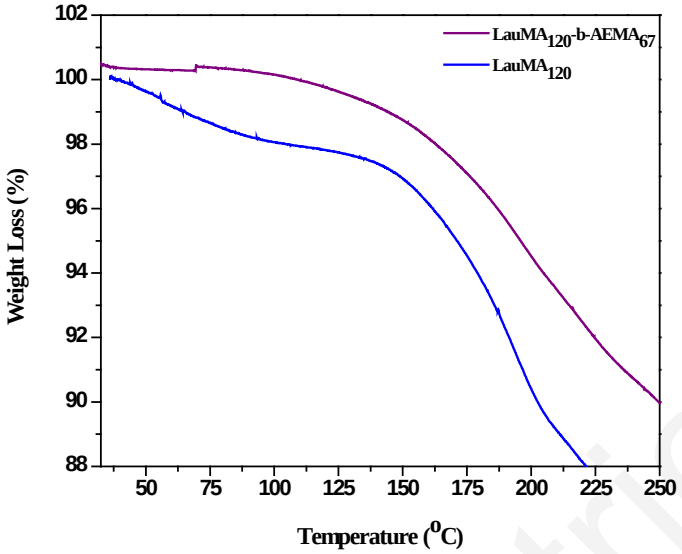

Figure 4.5: *TGA traces of the LauMA$_{120}$ homopolymer and the LauMA$_{120}$-b-AEMA$_{67}$ block copolymer.*

4.1.1.3 Aggregation Behaviour in Solution [154]

Due to their amphiphilic character, it was expected that the LauMA$_x$-*b*-AEMA$_y$ diblock copolymers would self-organize in selective solvents creating well-defined nanomorphologies. Therefore, in order to investigate the aggregation behavior of the four LauMA$_x$-*b*-AEMA$_y$ diblock copolymers in solution, a selective solvent (*n*-hexane) for the LauMA$_x$ block was chosen. In this solvent, the formation of micelles consisting of a LauMA$_x$ solvating corona and an AEMA$_y$ core occurred. DLS was employed to determine the hydrodynamic diameter (D_H) of these micelles. In Table 4.2, the experimental and theoretical (contour length) D_H values for the four LauMA$_x$-*b*-AEMA$_y$ diblock copolymers micellar systems in *n*-hexane are summarized. As seen in the Table, the experimental values (ranging between ~ 20-180 nm) were in most cases systematically lower than the theoretical ones, calculated assuming a spherical morphology for the micelles and fully extended chains (0.252 nm per monomer repeating unit) [31]. This is reasonable since in solution the polymer chains especially those constructing the micellar core are not found in their extended form.

Moreover, from the data it can be clearly seen that micelles of tunable diameters could be obtained upon varying the block lengths of the two segments. Because these systems were

destined to be used as a nanoenviroment for the encapsulation of metal nanoparticles (MNPs), the ability to control the micellar size synthetically was extremely important, since the latter may affect significantly the size of the entrapped MNPs.

Table 4.2: *Hydrodynamic diameters obtained by DLS for a series of LauMA$_x$-b-AEMA$_y$ diblock copolymer micelles formed in n-hexane.*

Experimental structure[a]	LauMA$_{75}$-*b*-AEMA$_{46}$	LauMA$_{120}$-*b*-AEMA$_{67}$	LauMA$_{50}$-*b*-AEMA$_{9}$	LauMA$_{277}$-*b*-AEMA$_{81}$
D_H theor. (nm)	61	94	30	180
D_H exper. (nm)	37	56	17	181

[a]determined by SEC and ^{1}H NMR

In an effort to see whether our experimental results follow scaling theories corresponding to hairy micelles, the star polymer theory of Daoud and Cotton [47] was applied. According to this model the star polymer radius scales as $R \sim N_A^{3/5} f^{1/5}$ where *f* is the number of arms correlated to the aggregation number in the case of block copolymer micelles. In the case of hairy micelles in a good solvent of A blocks, the aggregation number Z scales as $N_B^{4/5}$. Therefore, the scaling relationship correlating the micellar radius with the lengths of the two blocks is: $R = aN_A^{3/5} N_B^{4/25}$ [146]. Experimental values of R of LauMA$_x$-*b*-AEMA$_y$ micelles formed in n-hexane follow in a relatively well manner the scaling law as seen from the results provided in Table 4.3. The deviation observed might be attributed to the non-negligible core size of the micelles.

Table 4.3: *Experimental hydrodynamic radius ($R_{exp.}$) of LauMA$_x$-b-AEMA$_y$ diblock copolymer micelles formed in n-hexane and the corresponding $R_{exp.}/ N_A^{3/5}. N_B^{4/25}$.*

Experimental structure[a]	N_A	N_B	$N_A^{3/5}$	$N_B^{4/25}$	$R_{exp.}$ *(nm)*	$R_{exp.}/ N_A^{3/5}. N_B^{4/25}$
.LauMA$_{75}$-*b*-AEMA$_{46}$	75	46	17.681	1.959	18.5	0.808
LauMA$_{120}$-*b*-AEMA$_{67}$	120	67	13.336	1.845	28	0.752
LauMA$_{50}$-*b*-AEMA$_9$	50	9	10.456	1.421	8.5	0.572
LauMA$_{277}$-*b*-AEMA$_{81}$	9	81	29.207	2.020	90.5	1.534

4.1.1.4 LauMA$_x$-b-AEMA$_y$/Pd(^{0}) Micellar Nanohybrids [145]

As previously mentioned (chapter 1), the *β*-ketoester unit is capable of complexing various transition metal ions of different oxidation states and geometries. It consists of two tautomeric forms the keto and the enol existing in equilibrium as shown in Figure 4.6.a.

The LauMA$_x$-*b*-AEMA$_y$ could complex and solubilize an inorganic palladium (II) salt in hydrophobic media by simply mixing micellar solutions of LauMA$_x$-*b*-AEMA$_y$ in *n*-hexane with Pd(CH$_3$COO)$_2$ at room temperature. Even though the Pd(II) salt was completely insoluble in this particular solvent, solubilization assisted by the ligating block copolymer (dissolution in the micellar core) was readily obtained. Pd(CH$_3$COO)$_2$ could be complexed and solubilized in *n*-hexane by the enolate anion, formed by adding triethylamine (Et$_3$N) to the micellar solution of LauMA$_x$-*b*-AEMA$_y$ in *n*-hexane. Upon loading of the micelles with Pd(II), yellow transparent solutions were obtained, indicating the formation of polymer-metal complexes as shown in Figure 4.7.

(a)

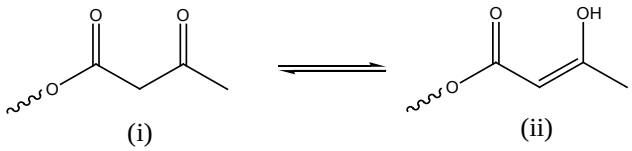

(b)

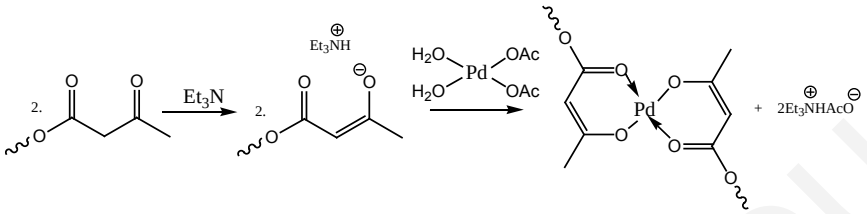

Figure 4.6: *(a) (i) The keto and (ii) the enol tautomeric forms of the β-ketoester group existing in equilibrium. (b) Formation of the enolate anion of the β-ketoester moiety in the presence of a strong base (Et_3N); subsequent replacement of the "X" type of acetate ligands leading to complex formation.*

(a)

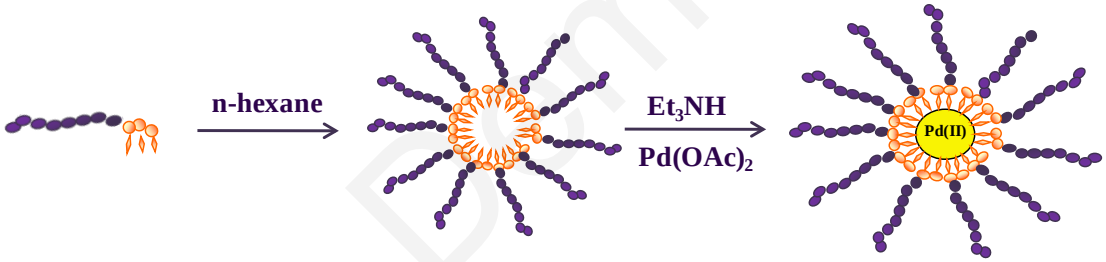

(b)

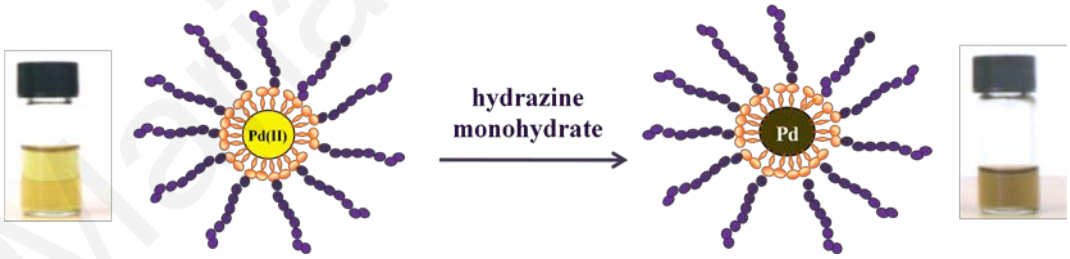

Figure 4.7: *Schematic representation of the steps followed for the formation of polymer-metal micellar nanohybrids: (a) formation of polymer/Pd(II) complex and (b) reduction of Pd(II) ions to noble Pd (^{0}).*

The UV-*Vis* spectra of the $LauMA_{120}$-*b*-$AEMA_{67}$ in *n*-hexane before and after complexation with the Pd(II) salt are exemplarily shown in Figure 4.8. All changes observed in the spectrum

of the LauMA$_x$-*b*-AEMA$_y$/Pd(II) compared to that of the "uncomplexed" polymer are attributed to complex formation. The presence of any uncomplexed salt is excluded, since the latter is completely insoluble in *n*-hexane. In the UV-*Vis* spectrum of polymer/Pd(II) complex, a peak at 378 nm appeared which is a characteristic peak for Pd(II) complexes [147]. Considering what is known from the literature, the above mentioned polymer-metal complexes were expected to have a four-coordinated square planar geometry. The whole spectrum resembles that of Pd(CH$_3$COO)$_2$ and Pd(AEMA)$_2$, suggesting a square-planar coordination geometry.

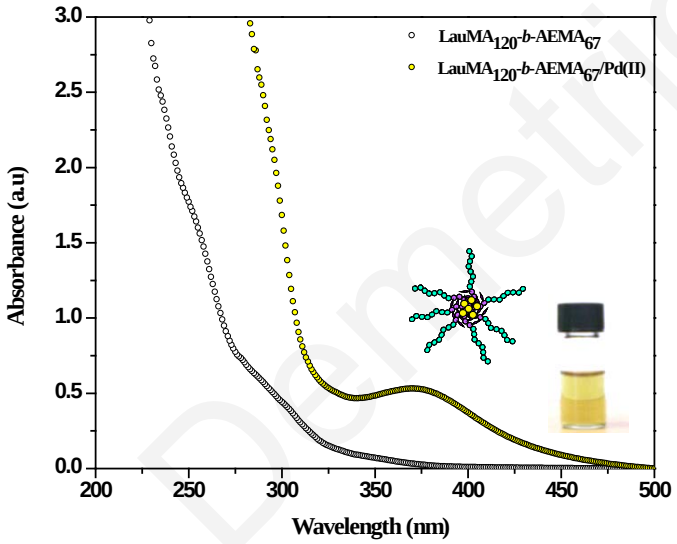

Figure 4.8: *UV-Vis spectra of the LauMA$_{120}$-b-AEMA$_{67}$ and the LauMA$_{120}$-b-AEMA$_{67}$/Pd(II) micellar nanohybrids formed in n-hexane.*

The chemical reduction of the Pd(II) ions incorporated within the micellar cores of the LauMA$_x$-*b*-AEMA$_y$ in *n*-hexane was accomplished *via* the addition of an excess of hydrazine monohydrate to the micellar solution. The reduction of Pd(II) to Pd(^{0}) was successful as indicated by a change in the color of the solution from yellow to dark brown as seen in Fig. 4.7.b. The darkening of the solution accompanied by the disappearance of the characteristic signal of Pd(II) at 378 nm (Figure 4.9) indicated colloidal Pd nanoparticle formation [42].

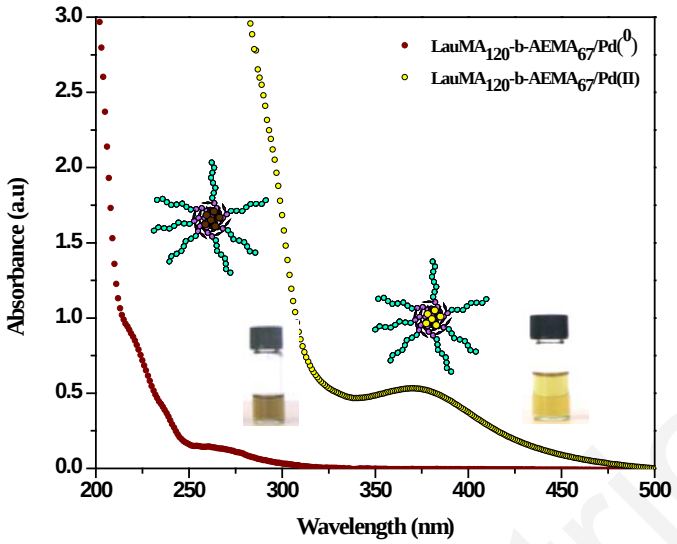

Figure 4.9: *UV-Vis spectra of the $LauMA_{120}$-b-$AEMA_{67}$/$Pd(CH_3COO)_2$ complex formed in n-hexane and the $LauMA_{120}$-b-$AEMA_{67}$/$Pd(^0)$. The latter were obtained upon reduction of Pd(II) in the presence of hydrazine monohydrate.*

The hydrodynamic diameters of the hybrid micelles determined by DLS are summarized in Table 4.4. The obtained results suggested that the reduction caused a decrease in the D_Hs of the micelles compared to the non-loaded macromolecular aggregates (see Table 4.2). Similar observations were reported by other groups [82,148] and were attributed to a more compact conformation adopted by the polymer surrounding the metal nanoparticle due to the interactions existing between the surface of the nanoparticle and the metal binding block segments. Alternatively, the decrease in the micellar size upon reduction might be a result of a change in the aggregation number within the micelle occurring due to the existence of the metal nanoparticle/coordinating block segment interactions [82].

Table 4.4: *Hydrodynamic diameters obtained by DLS for a series of LauMA$_x$-b-AEMA$_y$/Pd(^{0}) micellar nanohybrids formed in n-hexane.*

	Experimental structure[a]	**LauMA$_{75}$-*b*-AEMA$_{46}$**	**LauMA$_{120}$-*b*-AEMA$_{67}$**	**LauMA$_{50}$-*b*-AEMA$_9$**	**LauMA$_{277}$-*b*-AEMA$_{81}$**
AEMA:Pd(^{0}) 2:1	D_H exper. (nm)	21	36	13	143

Dilute hybrid micellar solutions were spin-coated on a mica substrate and visualized by AFM. Figure 4.10 presents the AFM micrographs of (a) LauMA$_{50}$-*b*-AEMA$_9$/Pd(^{0}), (b) LauMA$_{120}$-*b*-AEMA$_{67}$/ Pd(^{0}), (c) LauMA$_{75}$-*b*-AEMA$_{46}$/Pd(^{0}) and (d) LauMA$_{277}$-*b*-AEMA$_{81}$/ Pd(^{0}). Relatively monodisperse micellar hybrids were obtained with sizes comparable with those obtained by the DLS. Depending on the ratios of the LauMA$_x$ and the AEMA$_y$ segments within the block copolymers, either spherical (LauMA$_{50}$-*b*-AEMA$_9$, LauMA$_{277}$-*b*-AEMA$_{81}$) or elliptical (LauMA$_{120}$-*b*-AEMA$_{67}$, LauMA$_{75}$-*b*-AEMA$_{46}$) shaped micelles were observed. Similarly, Sigel *et al.* [149] have reported that the variation of the AEMA molar fraction within BuMA$_x$-*b*-AEMA$_y$ block copolymer resulted in the formation of micelles with different shapes. In particular, spherical shaped micelles have been found to be formed for molar fractions in the range of 0.1–0.15, while for AEMA molar fractions of 0.22 and 0.45, elliptical and cylindrical shaped micelles respectively have been observed.

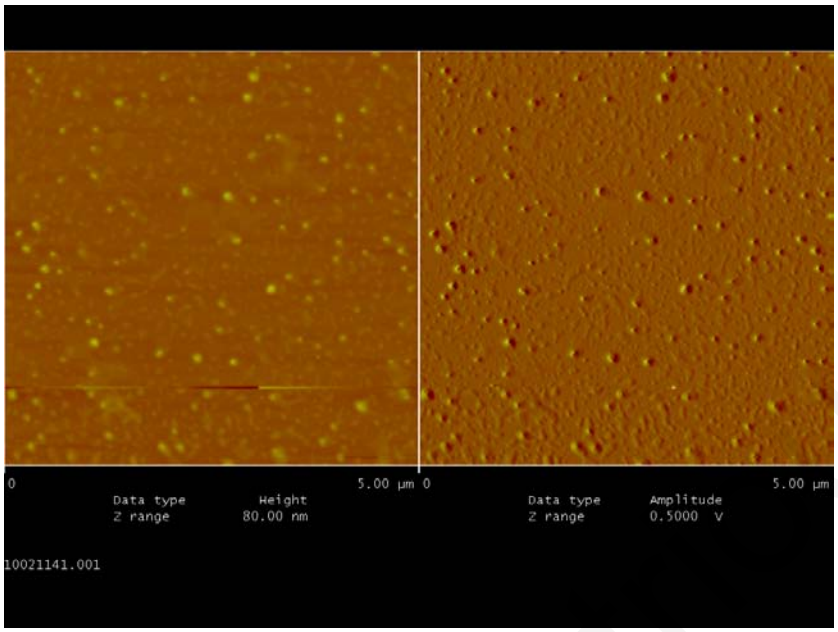
0
5.00 µm 0
5.00 µm
Data type Height
Z range 80.00 nm
Data type Amplitude
Z range 0.5000 V
10021141.001

(a)

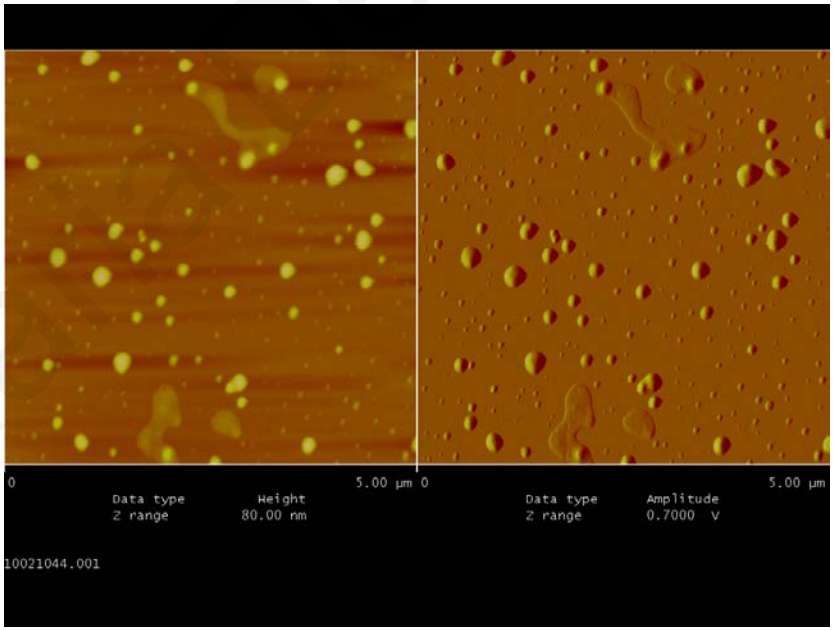
0
5.00 µm 0
5.00 µm
Data type Height
Z range 80.00 nm
Data type Amplitude
Z range 0.7000 V
10021044.001

(b)

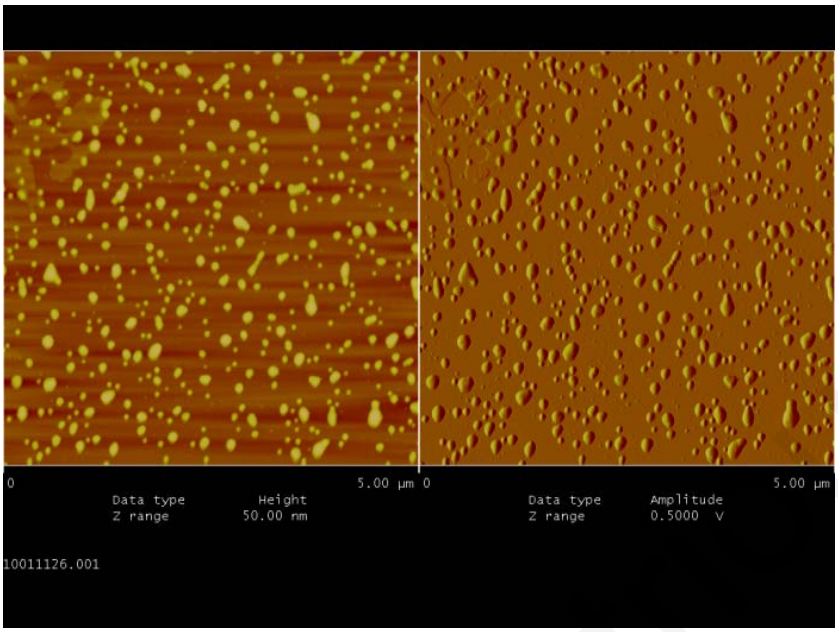

(c)

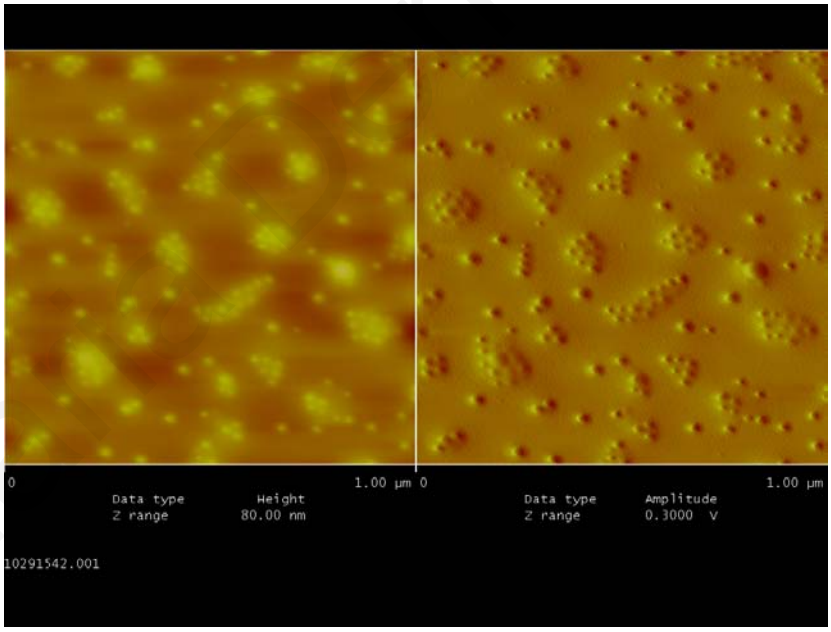

(d)

Figure 4.10: *AFM images of the LauMA$_x$-b-AEMA$_y$/Pd(^{0}) systems formed in n-hexane as obtained after spin-coating of a dilute micellar solution on mica. (a) LauMA$_{50}$-b-AEMA$_9$/Pd(^{0}), (b) LauMA$_{277}$-b-AEMA$_{81}$/Pd(^{0}) (c) LauMA$_{120}$-b-AEMA$_{67}$/Pd(^{0}) and (d) LauMA$_{75}$-b-AEMA$_{46}$/Pd(^{0})*

TEM was also employed for the determination of the size and the morphology of the Pd NPs embedded within the micelles. Figure 4.11 shows the TEM images of the LauMA$_{50}$-*b*-AEMA$_9$/Pd(^{0}), LauMA$_{120}$-*b*-AEMA$_{67}$/Pd(^{0}) and LauMA$_{277}$-*b*-AEMA$_{81}$/Pd(^{0}) systems. From the images, it is evident that depending on the block length within the block copolymers, micelles of tunable diameters can be obtained, leading to control over the NP size. The obtained Pd NPs were characterized by narrow size distribution and mean diameters of 2.3 ± 0.3, 7.2 ± 1.7 and 18.6 ± 4.5 nm for the LauMA$_{50}$-*b*-AEMA$_9$/Pd(^{0}), LauMA$_{120}$-*b*-AEMA$_{67}$/Pd(^{0}) and LauMA$_{277}$-*b*-AEMA$_{81}$/Pd(^{0}) respectively.

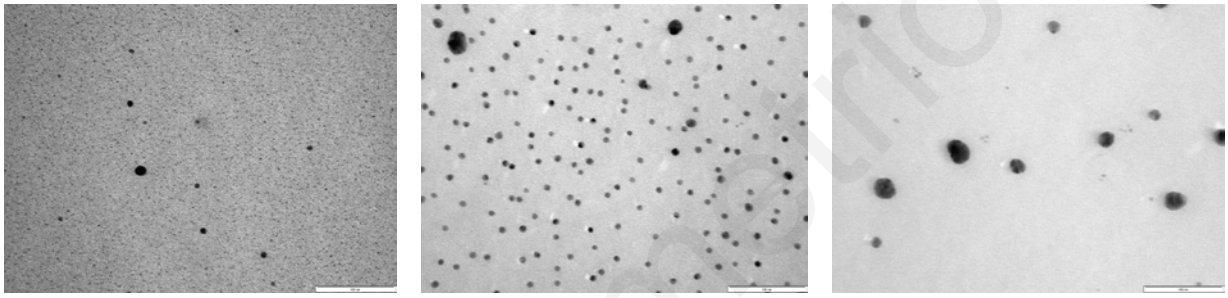

(a) **(b)** **(c)**

Figure 4.11: *TEM images of (a) LauMA$_{50}$-b-AEMA$_9$/Pd(^{0}), (b) LauMA$_{120}$-b-AEMA$_{67}$/Pd(^{0}) and (c) LauMA$_{277}$-b-AEMA$_{81}$/Pd(^{0}) systems.*

4.1.2 *CbzEMA$_x$-b-AEMA$_y$ Amphiphilic Diblock Copolymers* [150]

4.1.2.1 *Synthesis and Molecular Characterization [150]*

Well-defined CbzEMA$_x$ homopolymers and CbzEMA$_x$-*b*-AEMA$_y$ diblock copolymers were successfully synthesized following typical RAFT methodologies. As stated in the experimental section (3.5.1), the CbzEMA monomer was in-house synthesized following a two-step methodology as already described in the experimental section (3.5.1). CbzEMA homopolymers were synthesized first by RAFT and further used as the macro-CTAs for the growth of the AEMA block segment as schematically presented in Figure 4.12.

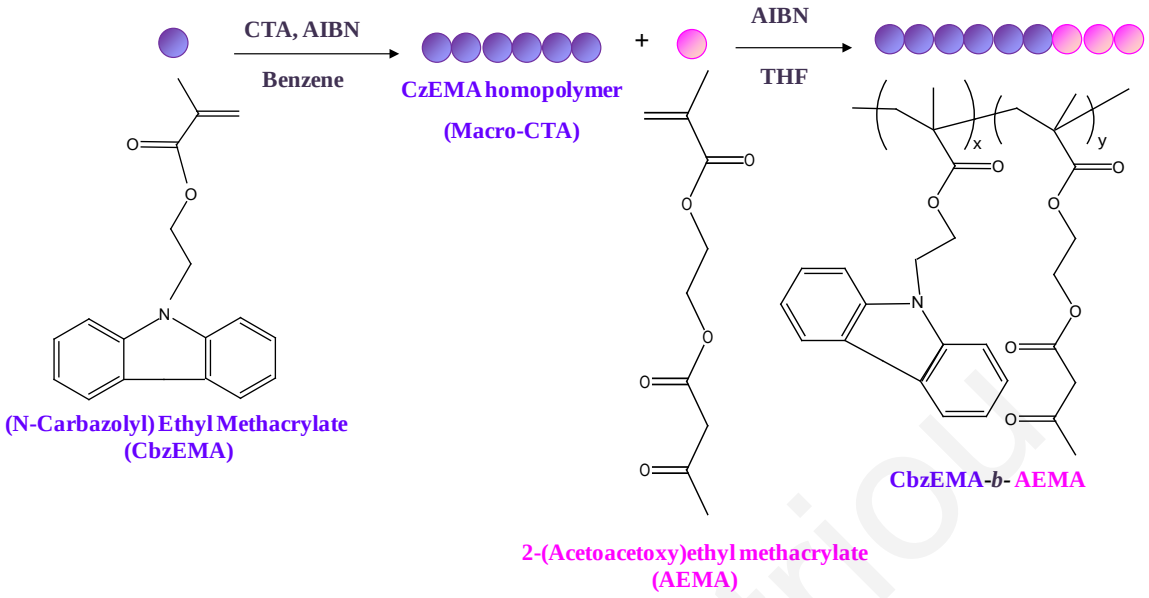

Figure 4.12: *Schematic representation of the polymerization steps followed for the synthesis of CbzEMA$_x$-b-AEMA$_y$ diblock copolymers.*

SEC and H^1 NMR were used to determine the molecular characteristics of all polymers. As far as the data obtained by SEC are concerned, low to moderate PDIs were observed for the homopolymers and diblock copolymers, varying between ~1.2 – 1.8. In most cases, the experimental MWs were found to be in good agreement with the theoretical ones as seen in Table 4.5. Figure 4.13 exemplarily displays the SEC traces of the CbzEMA$_{82}$ homopolymer and the corresponding CbzEMA$_{82}$-*b*-AnMMA$_{47}$ diblock copolymer. The MWD of the latter is shifted towards higher MWs compared to that of the homopolymer, demonstrating the block efficiency from homopolymer to block copolymer.

Figure 4.14 shows the ^{1}H NMR spectrum of the CbzEMA$_{82}$-*b*-AnMMA$_{47}$ diblock copolymer. The peak assignments are provided on the spectrum. The AEMA comonomer compositions within the CbzEMA$_x$-*b*-AnMMA$_y$ diblock copolymers were determined from the ratio of the areas under the characteristic signals of the AEMA and the CbzEMA, appearing at 2.27 (f) and 7.99 (h) respectively.

Table 4.5: *Characteristics of the homopolymers and block copolymers based on CbzEMA and AEMA obtained by RAFT (polymerization yields, molecular weights and polydispersity indices).*

Experimental Structure[a]	**Conversion (%)**	**Theor. MW[b] gmol^{-1}**	**SEC[c] Mn (gmol^{-1})**	**PDI**
$CbzEMA_{82}$	76	21388	23075	1.19
$CbzEMA_{82}$-*b*-$AEMA_{47}$	36	11986	31800	1.31
$CbzEMA_{104}$	75	41830	29158	1.50
$CbzEMA_{104}$-*b*-$AEMA_{44}$	n.d.	n.d.	22950	1.33
$CbzEMA_{38}$	81	11534	10883	1.22
$CbzEMA_{38}$-*b*-$AEMA_{10}$	20.5	11931	14464	1.83
$CbzEMA_{38}$-*b*-$AEMA_{50}$	75	12483	12561	1.34

[a]determined by SEC and ^{1}H NMR; [b][(g. monomer)/(mol RAFT agent)]x(polymerization yield) + MW of CTA (for homopolymers) and [(g. monomer)/(mol CTA agent)]x(polymerization yield) + M_n of macro-CTA (for diblock copolymers); [c]SEC calibrated with PMMA standards; M_n = number average molecular weight; PDI = polydispersity index; CbzEMA = 2-(N-carbazolyl) ethyl methacrylate; AEMA = 2-(acetoacetoxy)ethyl methacrylate; n.d.: not determined.

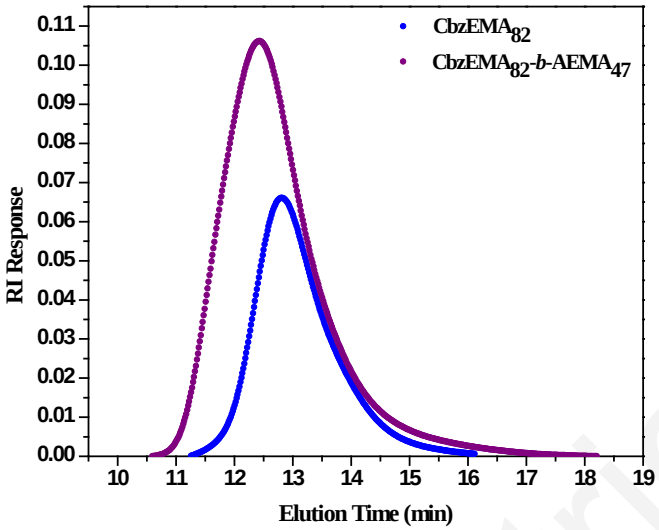

Figure 4.13: *SEC elugrams of the $CbzEMA_{82}$ and the $CbzEMA_{82}$-b-$AEMA_{47}$.*

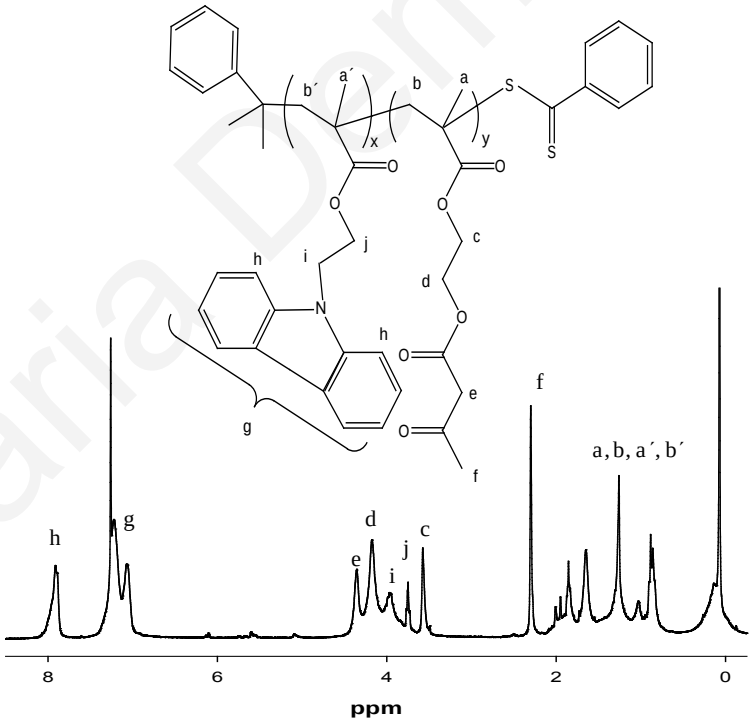

Figure 4.14: *^{1}H NMR spectrum of the $CbzEMA_{82}$-b-$AnMMA_{47}$ diblock copolymer. *Solvent ($CHCl_3$).*

4.1.2.2 Thermal properties

The glass transition (T_g) and decomposition temperatures of the carbazole-containing systems were provided by DSC and TGA measurements, respectively. The T_g of the $CbzEMA_{82}$ homopolymer was determined to be 145 ^oC, which is close to previous findings [151]. As seen in Figure 4.15 (a), the $CbzEMA_{82}$-*b*-$AEMA_{47}$ diblock copolymers exhibits two T_gs (~ 124 ^oC for the CbzEMA block and ~ 13 ^oC for the AEMA block), suggesting that microphase separation may occur in the bulk. The fact that the T_g values of the block copolymer deviate from the corresponding homopolymers may suggest partial intermixing of the polymer segments.

The obtained TGA results indicated that the $CbzEMA_x$-*b*-$AEMA_y$ exhibited relatively higher thermal stability than the $LauMA_x$-*b*-$AEMA_y$ diblock copolymers. More precisely, the polymers started losing weight at ~250 ^oC and decomposed losing most of their weight at around 400 ^oC (Figure 4.15 (b)), whereas as previously discussed (sub-chapter 4.1.2), the $LauMA_x$-*b*-$AEMA_y$ systems started decomposing at 100-150 ^oC while at ~300 ^oC decomposed completely.

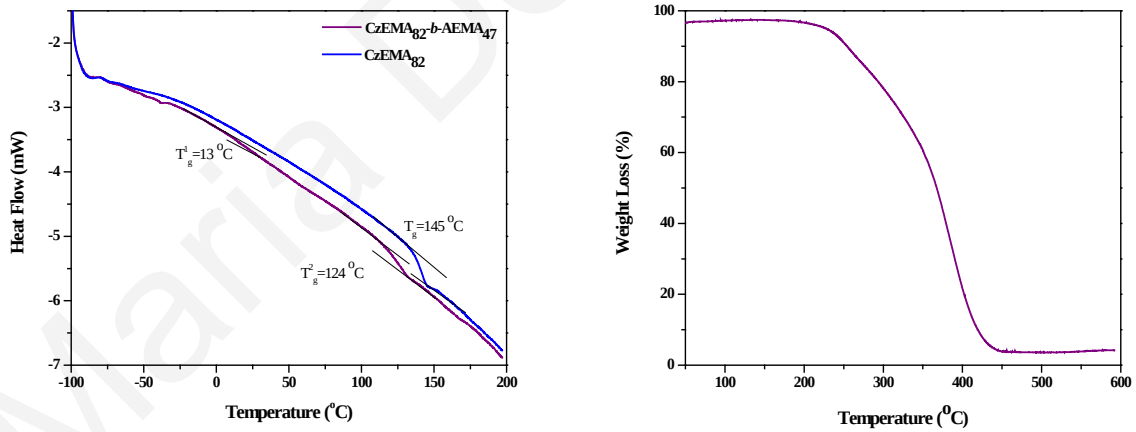

Figure 4.15: *(a) DSC curves of the $CbzEMA_{82}$ and $CbzEMA_{82}$-b-$AEMA_{47}$. (b) TGA curve of the $CbzEMA_{82}$-b-$AEMA_{47}$.*

4.1.2.3 CbzEMA$_x$-b-AEMA$_y$ /Pd(^{0}) micellar nanohybrids

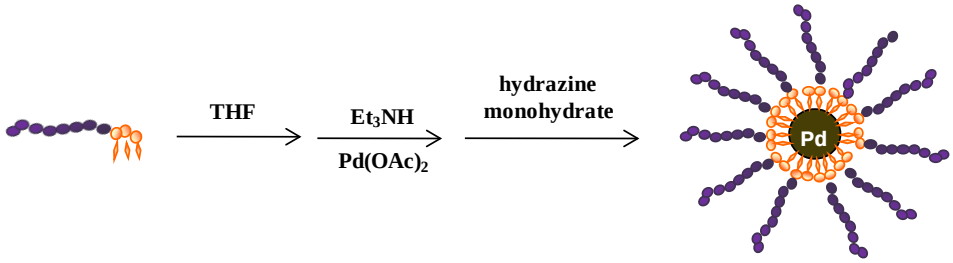

Figure 4.16: *Formation of micellar nanohybrids consisting of CbzEMA$_x$-b-AEMA$_y$ diblock copolymers and Pd(^{0}) nanoparticles in an organic solvent (THF).*

The CbzEMA$_x$-*b*-AEMA$_y$/Pd(^{0}) hybrid systems were fabricated in THF, which is a non-selective solvent (i.e. a good solvent) for both, the CbzEMA and AEMA block segments. Therefore, the CbzEMA$_x$-*b*-AEMA$_y$ block copolymers exist only as unimers in this solvent. Upon the addition of the Pd salt no complexation occured between Pd(II) ions and the *β*-ketoester groups as demonstrated by UV-*vis* measurements, since the characteristic peak at 378 nm corresponding to Pd ion complexes did not appear (Figure 4.17). This phenomenon is likely to attributed to the fact that THF is a good solvent for Pd(CH$_3$COO)$_2$ therefore the distribution of the salt in an excess of solvent may favor de-complexation [15]. However, the reduction of Pd(II) into Pd(^{0}) via the addition of hydrazine monohydrate resulted to micelle formation. The resulting polymer/Pd(^{0}) micellar systems consisted of a CbzEMA$_x$ corona and an AEMA$_y$/Pd(^{0}) insoluble core, as schematically presented in Figure 4.16.

Similar observations i.e. micelle formation upon complexation and/or reduction were reported by various groups. For example, Zhao *et al.* [172] have reported the induction of micellization in THF upon coordination of Cd^{2+} metal ions with the 2VP units of a PS-*b*-P2VP block copolymer. In the absence of the ions both block segments are soluble in THF, i.e. no micelles were present, whereas, upon addition of Cd^{2+} to the PS-*b*-P2VP/THF solution, the complexed 2VP segments became insoluble in THF and collapse resulting in formation of the single micelle cores. Moreover, Bronstein and coworkers **[**148] have reported the formation of micellar structures in aqueous media upon interaction of certain metal compounds such as Pd, Au and Pt with poly(ethylene oxide)-*b*-poly(ethylene imine) double-hybrophilic block copolymers.

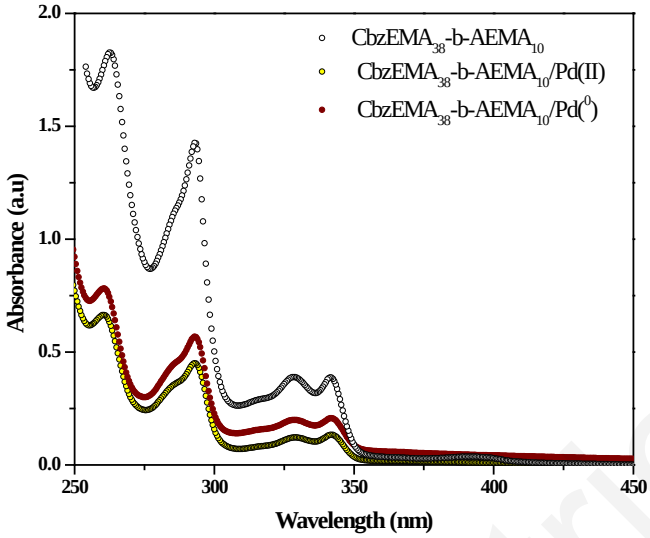

Figure 4.17: *UV-vis spectra of the uncomplexed $CbzEMA_{38}$-b-$AEMA_{10}$ diblock copolymer, the $CbzEMA_{38}$-b-$AEMA_{10}$/Pd(II) and the $CbzEMA_{38}$-b-$AEMA_{10}$/Pd(^{0}) systems.*

Table 4.6: *Hydrodynamic diameters of $CbzEMA_x$-b-$AEMA_y$ micelles generated in THF after the addition of $Pd(CH_3COO)_2$ followed by reduction.*

Experimental Structure	**$CbzEMA_{82}$-*b*-$AEMA_{47}$**	**$CbzEMA_{104}$-*b*-$AEMA_{44}$**
D_H (no Pd)	unimers	unimers
D_H (nm) AEMA:Pd(^{0}) [1:1]	91	114
D_H (nm) AEMA:Pd(^{0}) [2:1]	72	91

The D_Hs of the $CbzEMA_{82}$-*b*-$AEMA_{47}$ and $CbzEMA_{104}$-*b*-$AEMA_{44}$ hybrid micelles loaded with different Pd(^{0}) concentrations are summarized in Table 4.6. As seen in the Table, upon

increasing the Pd(^{0}) content within the micelles, the hydrodynamic diameter increased. As previously reported [148], in cases where micelles are formed owing to complexation with a metal compound, a change in metal loading may significantly affect the micellar size.

The CbzEMA$_x$-*b*-AEMA$_y$ hybrid systems were visualized by TEM. Figure 4.18 presents characteristic TEM images for the systems CbzEMA$_{82}$-*b*-AEMA$_{47}$/Pd(^{0}) and CbzEMA$_{104}$-*b*-AEMA$_{44}$/Pd(^{0}). From the images it can be clearly observed that in the case where the AEMA:Pd(^{0}) molar ratio of the systems is [2:1], the micelles had a smaller number of Pd NPs within their core than the systems with [1:1] molar ratio.

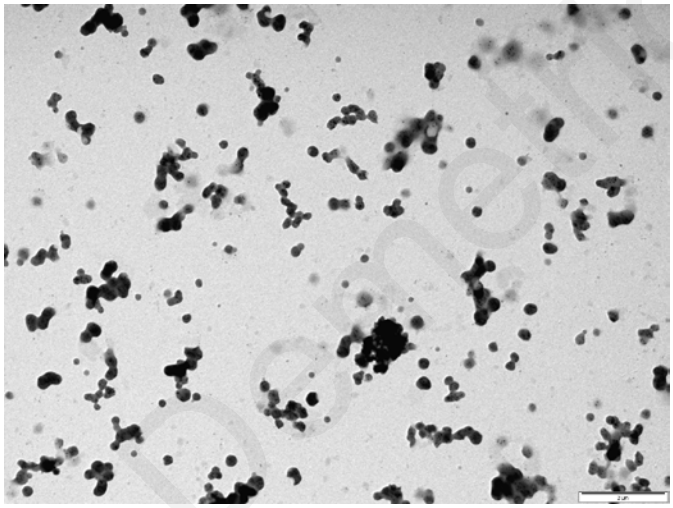

(a)

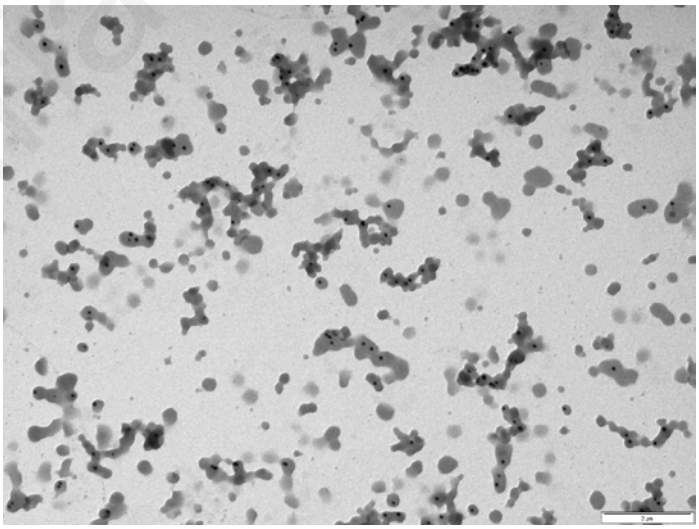

(b)

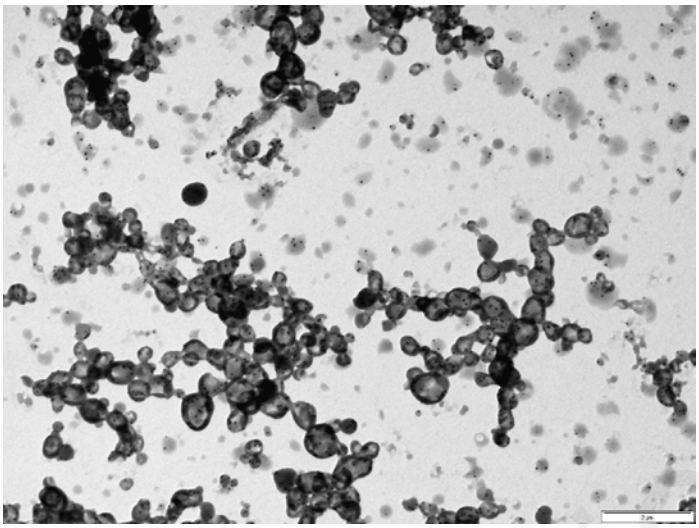

(c)

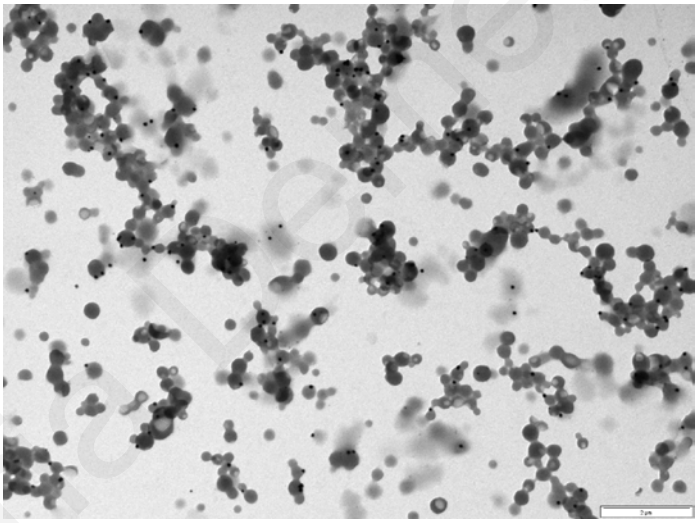

(d)

Figure 4.18: *TEM images of the carbazole-containing hybrid systems with different AEMA:Pd(^{0}) molar ratios: (a) CbzEMA$_{82}$-b-AEMA$_{47}$/Pd(^{0}) [1:1], (b) CbzEMA$_{82}$-b-AEMA$_{47}$/Pd [2:1], (c) CbzEMA$_{104}$-b-AEMA$_{44}$/Pd(^{0}) [1:1], and (d) CbzEMA$_{104}$-b-AEMA$_{44}$/Pd(^{0}) [2:1].*

4.1.3 AEMA$_x$-b-AnMMA$_y$ Amphiphilic Diblock Copolymers [153]

4.1.3.1 Synthesis and Molecular Characterization

Well-defined AEMA$_x$ and AnMMA$_x$ homopolymers, as well as AEMA$_x$-*b*-AnMMA$_y$ diblock copolymers were successfully synthesized by RAFT polymerization. The AnMMA monomer was in-house synthesized as described in the experimental section (see sub-chapter 3.6.1). To the best of our knowledge for the first time in this work well-defined AnMMA$_x$ homopolymers and AEMA$_x$-*b*-AnMMA$_y$ diblock copolymers are prepared by RAFT polymerization method. Initial efforts carried out for the preparation of these diblock copolymers involved the synthesis of AnMMA$_x$ homopolymers to be further used as macro-CTAs for the growth of the 2nd block segment. The polymerization of AnMMA was carried out by using CDTB or CPDTB as the CTAs. The obtained data presented in Table 4.8, demonstrated the effectiveness of the RAFT process towards the polymerization of this monomer, especially in the case where CPDTB was used as the CTA. As reported by Moad *et al*, at certain RAFT agent concentrations, retardation – that is partially manifested by an inhibition period corresponding to the required time to convert the RAFT agent into a polymeric RAFT agent – occurs in a much less extend in the case of CPDTB compared to CDTB [154]. Moreover, the copolymerization of the AnMMA$_x$ homopolymer with AEMA monomer was not successful. For that reason, AEMA$_x$ homopolymers were synthesized first and successfully used as the macro-CTAs for the growth of the AnMMA segment as schematically presented in Figure 4.19.

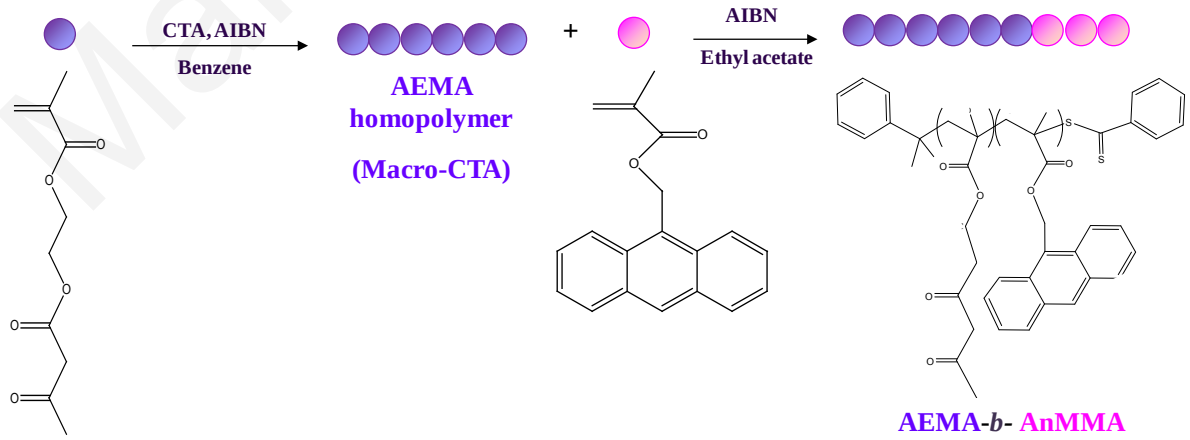

Figure 4.19: *Schematic representation of the polymerization steps followed for the synthesis of AEMA$_x$-b-AnMMA$_y$ diblock copolymers.*

Table 4.7 summarizes the chemical structures of all homopolymers and diblock copolymers prepared along with their molecular MWs and composition characteristics. The post-growth of the AnMMA block onto the $AEMA_x$ homopolymers used as the macro-CTA did not proceed in a quantitative manner. The low polymerization conversion reported may be attributed to the multiple precipitation steps required for the isolation of the pure product as stated in the experimental section as well as to the use of CDTB-$AEMA_x$ macro-CTAs instead of CPBTD-$AEMA_x$ systems.

Table 4.7: *Characteristics of the homopolymers and block copolymers based on AEMA and AnMMA obtained by RAFT (polymerization yields, molecular weights and polydispersity indices).*

Experimental Structure[a]	**Yield (%)**	**Theor. MW[b] g.mol^{-1}**	**SEC Results[c]**	
			Mn	**PDI**
$AnMMA_{36}$ (CDTB)	37.5	18381	16177	1.31
$AnMMA_{47}$ (CPBD)	90	25062	13228	1.27
$AEMA_{42}$ (CDTB)	85	5694	9235	1.23
$AEMA_{42}$-*b*-$AnMMA_{83}$ (CDTB)	17	17688	18802	1.33
$AEMA_{42}$-b-$AnMMA_{113}$ (CDTB)	20	25810	38870	1.43
$AEMA_{21}$ (CDTB)	90	2414	4749	1.26
$AEMA_{21}$-b-$AnMMA_{43}$ (CDTB)	25	14279	15822	1.34

[a] Determined by SEC and ^{1}H NMR; [b] [(g. monomer)/(mol RAFT agent)]x(polymerization yield) + MW of CTA (for homopolymers) and [(g. monomer)/(mol CTA agent)]x(polymerization yield) + M_n of macro-CTA (for diblock copolymers); [c] Mn: number average molecular weight; PDI: polydispersity index. CDTB: cumyl dithiobenzoate. CPBD: 2-cyano-2-propylbenzodithioate.

Low to moderate PDIs were observed for the homopolymers and diblock copolymers, varying between 1.23 – 1.43. Figure 4.20 displays the SEC traces of the $AEMA_{21}$ homopolymer and the corresponding $AEMA_{21}$-*b*-$AnMMA_{43}$ diblock copolymer. The MWD of the latter wa s shifted towards higher MWs compared to that of the homopolymer, demonstrating the block efficiency from homopolymer to block copolymer.

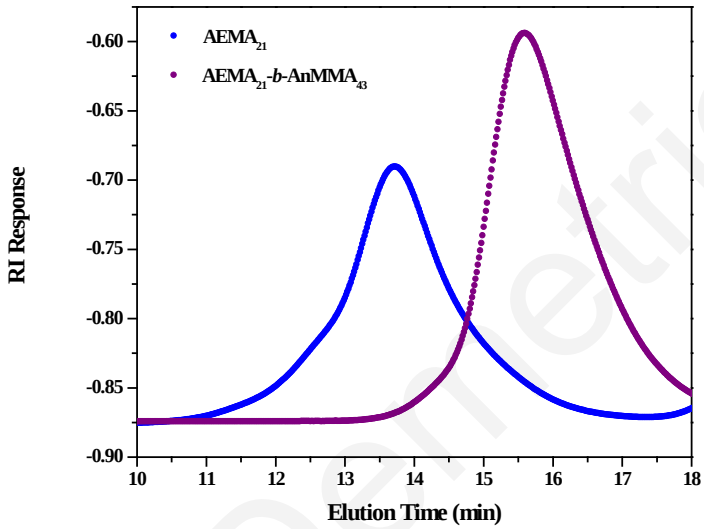

Figure 4.20: *SEC eluograms of the $AEMA_{21}$ and the $AEMA_{21}$-b-$AnMMA_{43}$.*

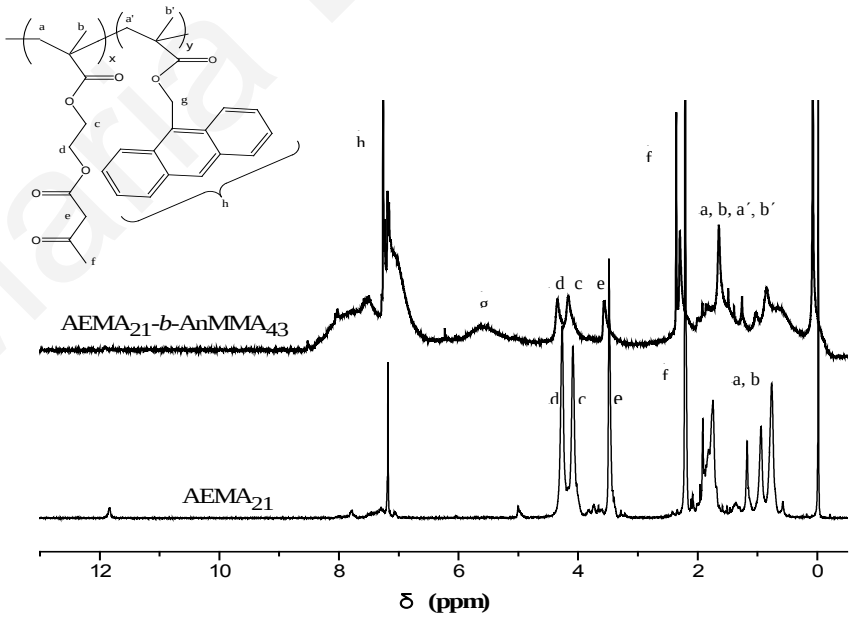

Figure 4.21: *^1H NMR spectrum of (a) the $AEMA_{21}$ homopolymer and (b) the $AEMA_{21}$-b-$AnMMA_{43}$ diblock copolymer.*

Figure 4.21 shows the ^{1}H NMR spectra of (a) the $AEMA_{21}$ homopolymer and (b) the $AEMA_{21}$-*b*-$AnMMA_{43}$ diblock copolymer. The peak assignments are shown in the two spectra. The AEMA comonomer compositions were determined from the ratio of the areas under the characteristic signals of the AEMA and AnMMA, appearing at 3.6 and 5.6 ppm respectively.

4.1.3.2 Thermal properties

DSC measurements provided the T_g temperatures of the $AEMA_x$ and $AnMMA_x$ homopolymers and the $AEMA_x$-*b*-$AnMMA_y$ diblock copolymers. The T_g of the $AEMA_x$ homopolymer was determined to be -3 ^oC, which is close to previous findings [80] whereas the T_g of the $AnMMA_x$ homopolymer was found to be around 125 ^oC. Block copolymers exhibited two T_gs (~ 10 ^oC for the $AEMA_x$ block and ~ 144 ^oC for the $AnMMA_y$ block), suggesting that microphase separation may exist in the bulk. In general, the T_gs in block copolymers can be influenced by the sizes of the phases generated and the compatibility of the different components (blocks). According to Buzin et al. [155] in the case where the two blocks in a diblock copolymer are incompatible, the lengths of the two segments are the determining factor for the sizes of the phases generated due to microphase separation; the morphology of the latter will depend on their ratio. The T_gs of both components are affected by the continuing molecules that cross the interface. Depending on the phase mobility, variation in the T_gs of the different block segments can be observed compared to the T_g values of the corresponding homopolymers. The fact that the T_g values of the block copolymer deviate from the corresponding homopolymers may suggest partial intermixing of the polymer segments. Moreover, in the case of the AnMMA segment, the observed differences in the glass transition temperature of the $AnMMA_{36}$ homopolymer and the $AnMMA_{83}$ block segment incorporated within the diblock copolymer (appearing at 125 ^oC and 144 ^oC respectively) may be reinforced by the increased MW and the more pronounced π-π interactions occurring between the AnMMA aromatic side chains of the $AnMMA_{83}$ segment present in the diblock, which promotes chain immobility [31].

The obtained TGA results indicated that the $AEMA_x$-*b*-$AnMMA_y$ exhibited relatively higher thermal stability than the $LauMA_x$-*b*-$AEMA_y$ and $CbzEMA_x$-*b*-$AEMA_y$ diblock copolymers.

More precisely, the polymers started losing weight ~300 ^{o}C and decomposed losing most of their weight at around 450 ^{o}C (Figure 4.23).

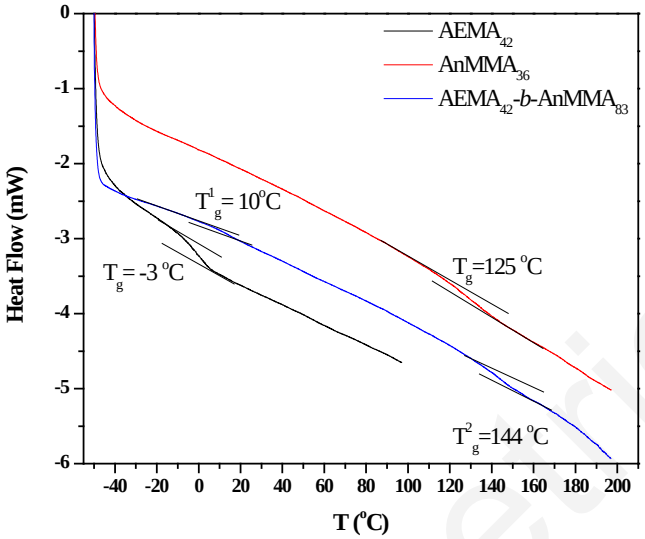

Figure 4.22: *DSC thermograms of the $AEMA_{42}$ homopolymer, the $AnMMA_{36}$ homopolymer and the $AEMA_{42}$-b-$AnMMA_{83}$ diblock copolymer.*

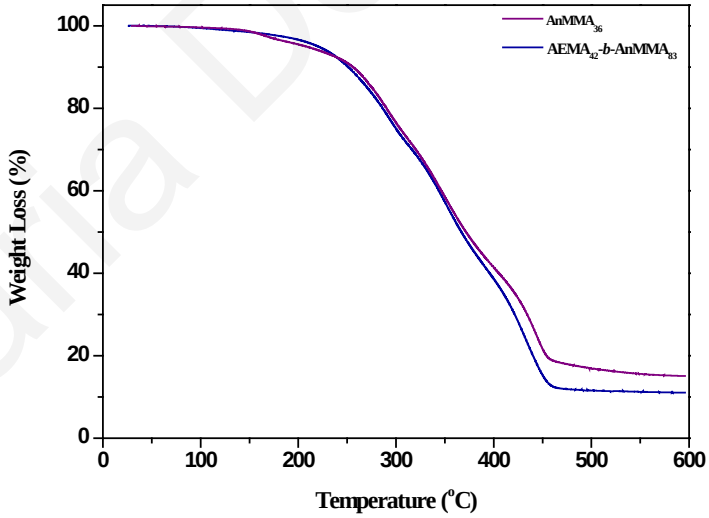

Figure 4.23: *TGA curves of the $AnMMA_{36}$ homopolymer and $AEMA_{42}$-b-$AnMMA_{83}$ diblock copolymer.*

4.1.3.3 $AEMA_x$-b-$AnMMA_y$/$Pd(^0)$ Micellar Nanohybrids

The $AEMA_x$-*b*-$AnMMA_y$/$Pd(^0)$ hybrid systems were fabricated in THF, in a similar way with the $CbzEMA_x$-*b*-$AEMA_y$/$Pd(^0)$ nanohybrids. THF is a non-selective solvent (i.e. a good solvent) for both, the AnMMA and AEMA block segments and therefore the $AEMA_x$-*b*-$AnMMA_y$ block copolymers exist only as unimers in this solvent. Micellization was induced, as in the case of carbazole-containing systems, upon addition of hydrazine monohydrate and the reduction of Pd(II) into $Pd(^0)$. The resulting polymer/$Pd(^0)$ micellar systems consisted of an $AnMMA_x$ corona and an $AEMA_y$/$Pd(^0)$ insoluble core. As can be seen in the UV-*vis* spectra, the complexation has an influence on the absorption spectra of the block copolymer (Figure 4.24). Particularly, a red shift of the π-π* band in the absorption spectra is observed upon complexation as similarly reported by other groups [156].

The D_Hs of the *$AEMA_x$-b-$AnMMA_y$/$Pd(^0)$* miceller nanohybrids were determined by DLS and it was found to range between 67-94 nm.

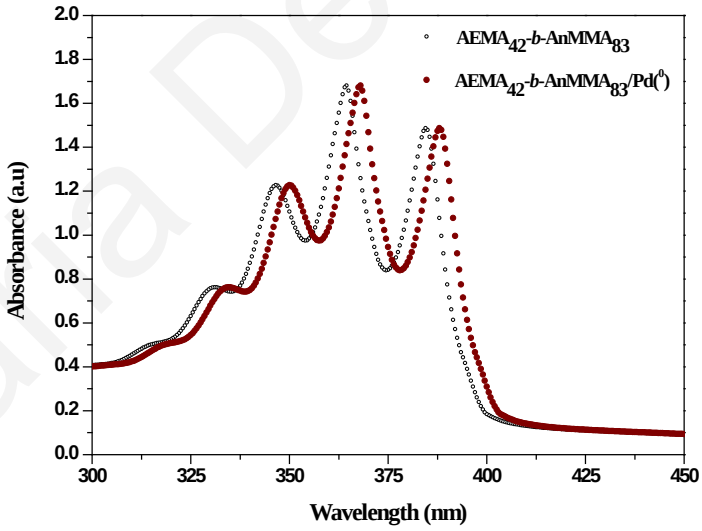

Figure 4.24: *UV-vis spectra of $AEMA_{42}$-b-$AnMMA_{83}$ and $AEMA_{42}$-b-$AnMMA_{83}$/$Pd(^0)$.*

Table 4.8: *Hydrodynamic diameters of $AEMA_x$-b-$AnMMA_y$ micelles generated in THF after the addition of $Pd(CH_3COO)_2$ followed by reduction.*

Experimental Structure	**$AEMA_{42}$-*b*-$AnMMA_{83}$**	**$AEMA_{42}$-*b*-$AnMMA_{113}$**	**$AEMA_{21}$-*b*-$AnMMA_{43}$**
D_H (nm) no Pd	unimers	unimers	unimers
D_H (nm) AEMA:Pd(^{0})	85	67	94

4.2 Applications

4.2.1 Fundamentals of Nonlinear Optics

In order to explain nonlinear effects, it is usually assumed that the nuclei and the electrons of the atoms form electric dipoles. The electromagnetic radiation interacts with these dipoles causing them to oscillate and act as new sources of electromagnetic radiation. As the intensity of radiation increases, the relationship between intensity and amplitude vibration becomes nonlinear resulting in the generation of harmonics of the frequency of the radiation emitted by the oscillating dipoles [157,158].

Nonlinearity in optics is manifested by changes in the optical properties (absorption coefficient, refractive index) of a material as the intensity of the input light is increased [158]. It involves the interaction of electromagnetic field in the material to produce new fields altered in phase, frequency, amplitude, or other propagation characteristics of the incident light [159].

The polarization induced in an atom or molecule upon interaction with an oscillating external electric field can be written as shown in Equation 2.14. The induced polarization is a vector related to the local electric-field (E_{local}) by the quantities α, β, γ, which are often referred to as the linear polarizability, quadratic hyperpolarizability and cubic hyperpolarizability, respectively. The β and γ terms describe a nonlinear response to the radiation field.

$$p = \alpha E_{local} + \beta E_{local}^2 + \gamma E_{local}^3 + \dots \quad (4.1)$$

In bulk samples the polarization per volume is considered, leading to the linear susceptibility $\chi^{(1)}$ and nonlinear susceptibilities $\chi^{(2)}$ (2^{nd} order) and $\chi^{(3)}$ (3^{rd} order) and is expressed as a power series in the field strength *E(t)* as follows [159,160,161]:

$$P(t) = \chi^{(1)} E(t) + \chi^{(2)} E^2(t) + \chi^{(3)} E^3(t) \quad (4.2)$$

4.2.1.1 Non Linear Optical Effects

4.2.1.1.a Saturable and reverse saturable absorption [162]

When a laser beam interact with a material, the absorption of the material is no more linear. i.e. it is not described anymore by the Beer-Lambert Law. Specifically, the absorption will be given in general by an equation of the form:

$$a = a_0 + \beta I \quad (4.3)$$

where α_0 and β are the linear and the non-linear absorption coefficient, respectively. Materials that are characterized by an intensity-dependent absorption are called non-linear absorbers. The non-linear absorption coefficient is associated with the imaginary part of the 3^{rd} order non-linear optical susceptibility $\chi^{(3)}$ which is in general a complex number. These two parts are linked with the following equation:

$$Im\ \chi^{(3)} = \frac{10^{-7} c^2 n_0^2 \beta}{96\pi^2 \omega} \quad (4.4)$$

Where c is the speed of light (in cm/sec), n_0 is the linear refractive index, β is the non-linear absorption coefficient (in cm/W) and ω is the angular frequency (in sec^{-1}).

The non-linear absorbers can be characterized by saturable absorption ($\beta<0$) and reverse saturable absorption ($\beta>0$) behaviour. In the former case, increase of the intensity of e.g. a laser beam transmitted through the sample results in increasing the transmittance of the sample

(at this particular wavelength), while in the latter case the sample transmittance decreases as the intensity of the laser beam increases.

The non-linear absorption can be described easily using a five-level system as shown in Figure 4.25. When the intensity of the incident electromagnetic radiation is high enough, the ground state becomes depleted and a sufficiently population is excited to the single state S_1. Before, the electrons relax back to the ground state, there is a possibility to absorb again and get excited to the higher single energy states (S_2 etc.). This last process is called "excited state absorption".

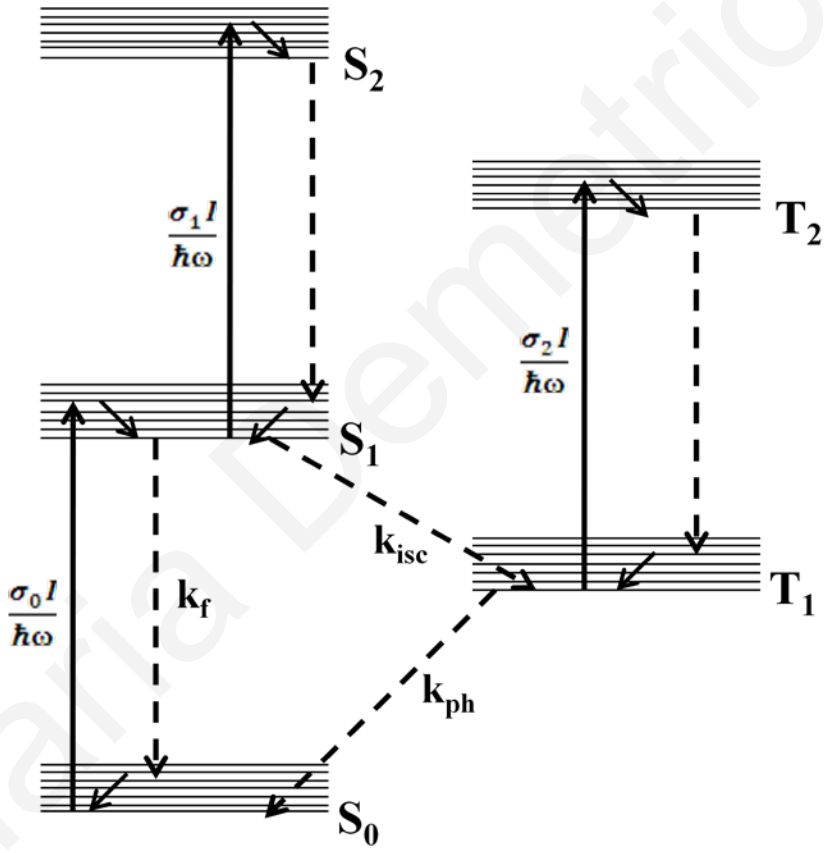

Figure 4.25: *Five-Level system.*

In general, the following processes can possibly occur after an electron is excited to the first energy state of a system:

- The electron is decayed to the ground state.
- The electron is excited through an intersystem crossing to a triplet state (k_{isc}).
- The electron can be further excited to an even higher single state.

The transmittance (i.e. the transparency) of the system is increased and the system acts as a saturable absorber, when the absorption cross-section of the excited state is smaller than that of the ground state. On the other hand, the material will operate as a reverse saturable absorber when (a) the excited state absorption cross-section is larger than that of the ground state; (b) the excited state absorption cross-section is sufficiently large so that the first excited state is saturated, (c) the relaxation from the higher energy states to the ground state must be fast enough, so as for absorption to take place again.

4.2.1.1.b Optical Limiting

Optical limiting is another interesting non linear optical effect. The optical limiters are used for the protection of sensitive detectors from intense laser radiation. Optical limiters are materials that strongly attenuate intense laser beams, while exhibiting high transmittance for low-intensity ambient light levels. As in the case of the materials exhibiting reverse saturable absorption behaviour, when the radiation passes through the material, a decrease of the transmission can occur as the laser intensity increases. These systems are of significant interest for the protection of human eyes, optical elements, or optical sensors from intense laser pulses, whereas another potential applicability is in the field of optical switching [162,163].

An ideal passive optical switch is a nonlinear optical device that is activated at a certain intensity or fluence threshold, whereupon the device becomes completely opaque. By contrast, an ideal optical limiter exhibits a linear transmission below threshold, but above threshold its output intensity is constant [164]. Under more realistic conditions, the limiter activation threshold is less well defined, and the output fluence will not be perfectly clamped at a constant value. The threshold should be such that the output intensity of the optical limiter does not exceed its destruction limit. A variety of nonlinear optical phenomena can be used to construct an optical limiter. These include absorptive processes such as reverse saturable absorption, two-photon absorption and nonlinear refractive processes such as self-focusing, self-defocusing and photorefraction and optically induced scattering [162,164].

In order for a material to be used as an optical limiter it must present the following characteristics: (a) Low light threshold, (b) satisfactory limiting efficiency in a wide range of laser intensity (resistance to laser-induced damage), (b) sensitive broadband response to long

and short pulses, (c) high linear transmission and (d) negligible scattering of the laser beam when this passes through the material [162,165].

4.2.1.1.c Self-focusing and Self-defocusing [162]

If an intense laser pulse propagates through a non-linear material, the refractive index of the material changes depending on the intensity of the laser pulse. The laser beam has a Gaussian spatial distribution.

In the center of the beam, where the intensity has a maximum, the material will also have a maximum refractive index. The refractive index is reduced when moving radial to the edges and the beam intensity exponentially decreases. Thus the material acts as a focusing lens at the point, where the beam is propagating through it, and has the ability to further focused the beam which causes the self-focusing effect. On the other hand, if the non linear refractive index is negative, then it will be increased when moving from the center to the edges of the beam. In this case the material acts as a defocusing lens resulting in defocusing of the transmitting beam (self-defocusing).

4.2.1.2 Nonlinear Optical Response of the LauMA$_x$-b-AEMA$_y$/Pd(^{0}) Hybrid Micellar Systems [145]

The nonlinear optical properties of the LauMA$_x$-*b*-AEMA$_y$/Pd(^{0}) hybrid micellar systems have been studied by means of the Z-scan technique, employing both visible (532 nm) and infrared (1064 nm) laser pulses as described in the experimental section. As already mentioned, these studies were performed in the Research Laboratory of Prof. S. Couris at ICE-FORTH, in Patras. For the measurements, different concentrations of Pd-containing micellar hybrid systems in *n*-hexane have been prepared. Subsequently, Z-scan measurements of these samples have been performed at various incident laser energies. The samples were placed into 1 mm thick quartz cells. The UV-Vis-NIR absorption spectra were measured regularly during the period of the experiments in order to ensure that no photo-degradation or any other modification of the complexes has occurred. In Figure 4.26, some typical absorption spectra of

the samples LauMA$_{75}$-*b*-AEMA$_{46}$/Pd(^{0}) and LauMA$_{120}$-*b*-AEMA$_{67}$/Pd(^{0}), having Pd concentration of 3.2 and 3 mM respectively are presented. As can be seen from these spectra, at 532 nm there was some sizeable linear absorbance, which reduced to almost zero at 1064 nm.

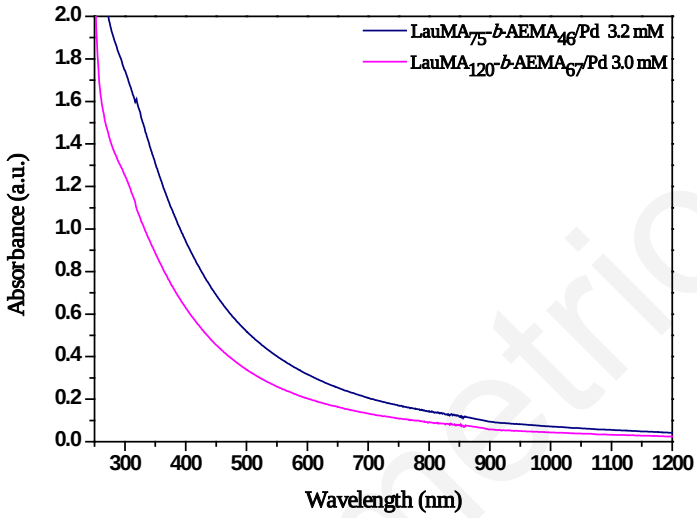

Figure 4.26: *Characteristic absorption spectra of the investigated systems.*

In order to account for contributions on the NLO response of the solutions arising either from the solvent and/or the polymers, the response of each component has been measured separately under identical conditions with those used for the measurements of the solutions. From these "control" measurements, it was found that *n*-hexane exhibited negligible nonlinear absorption but significant nonlinear refraction while polymer solutions in *n*-hexane did not exhibit any additional nonlinear optical response. Hence, the nonlinear optical response of *n*-hexane has been taken into account for the analysis of the experimental data.

Concerning the "open-aperture" Z-scans of the LauMA$_{75}$-*b*-AEMA$_{46}$/Pd(^{0}) micellar solutions, they have been found to exhibit a transmittance valley both at 532 and 1064 nm, indicative of reverse saturable absorption (RSA) like behaviour corresponding to positive nonlinear absorption coefficient β and consequently positive Im$\chi^{(3)}$. Moreover, as neither the neat *n*-hexane nor the polymers contribute to the nonlinear absorption, the observed nonlinear absorption has been unambiguously attributed to the Pd nanoparticles.

From the division of the "closed-aperture" Z-scans by the corresponding "open-aperture" ones, the "divided" Z-scans were obtained. These were found to exhibit a pre-focal valley

followed by a post-focal peak, suggesting self-focusing behavior of the solutions. From the "divided" Z-scans, the difference of the normalized transmission between the valley and the peak, i.e. the so-called ΔT_{p-v} parameter, was determined. Since the ΔT_{p-v} values of the solutions were found to be larger than those found for n-hexane, it was concluded that the Pd nanoparticles exhibited same sign refractive nonlinearity with that of the solvent (i.e. self-focusing). It has been also observed, that the ΔT_{p-v} parameter increased linearly with the incident laser energy as seen in Figure 4.27.

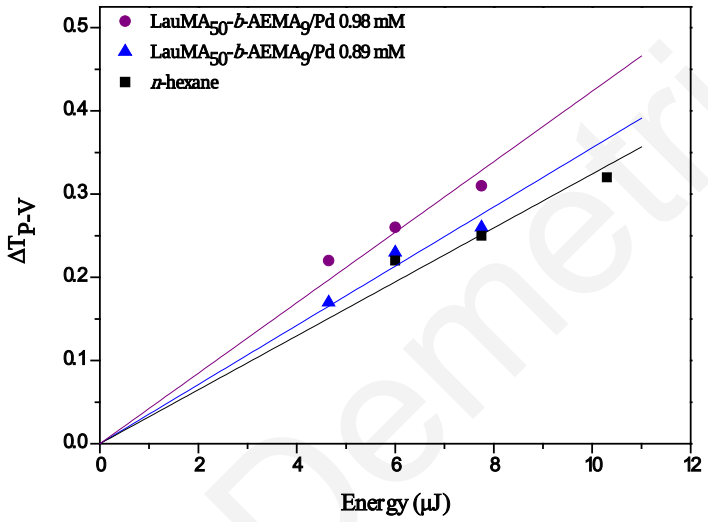

Figure 4.27: *ΔT_{p-v} values as a function of the incident laser energy for the LauMA$_{50}$-b-AEMA$_9$/Pd(^{0}) micellar system.*

The characteristic "open-aperture" and "divided" Z-scans of a LauMA$_{277}$-*b*-AEMA$_{81}$/Pd(^{0}) solution are presented as an example in Figure 4.28. The Z-scan curves (a) and (c) correspond to 532 nm excitation, while the curves (b) and (d) to 1064 nm excitation. In particular, figures (a) and (b) show the "open-aperture" Z-scans of a LauMA$_{277}$-*b*-AEMA$_{81}$/Pd(^{0}) system dissolved in *n*-hexane having a Pd concentration of 1.7 mM, while in Figures (c) and (d) the corresponding "divided" Z-scans are shown together with the neat *n*-hexane Z-scans obtained under identical experimental conditions. As can be easily seen from these curves, the nonlinear refraction of the solution (i.e. the ΔT_{p-v}) was larger than that of *n*-hexane since they both exhibit same sign Re$\chi^{(3)}$. The difference in the observed response was due to the presence of Pd(^{0}) NPs within the micellar systems, as polymers do not contribute to the nonlinearity.

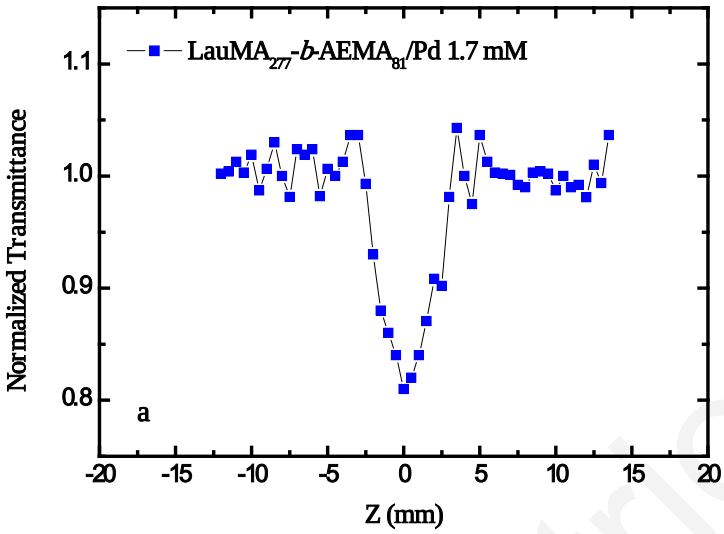

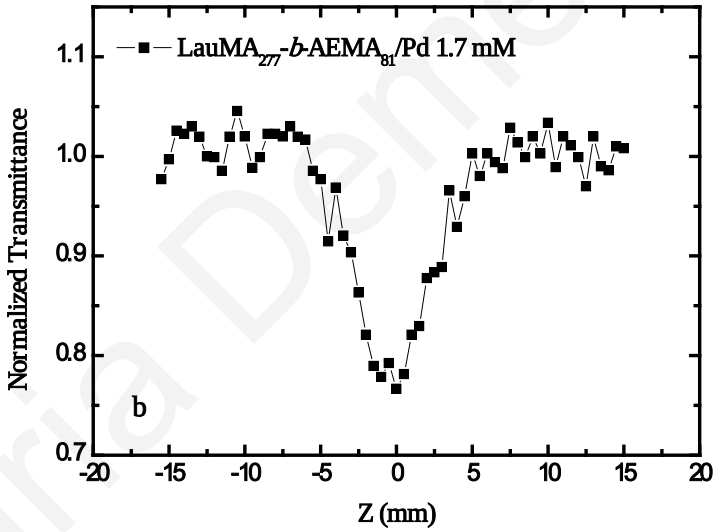

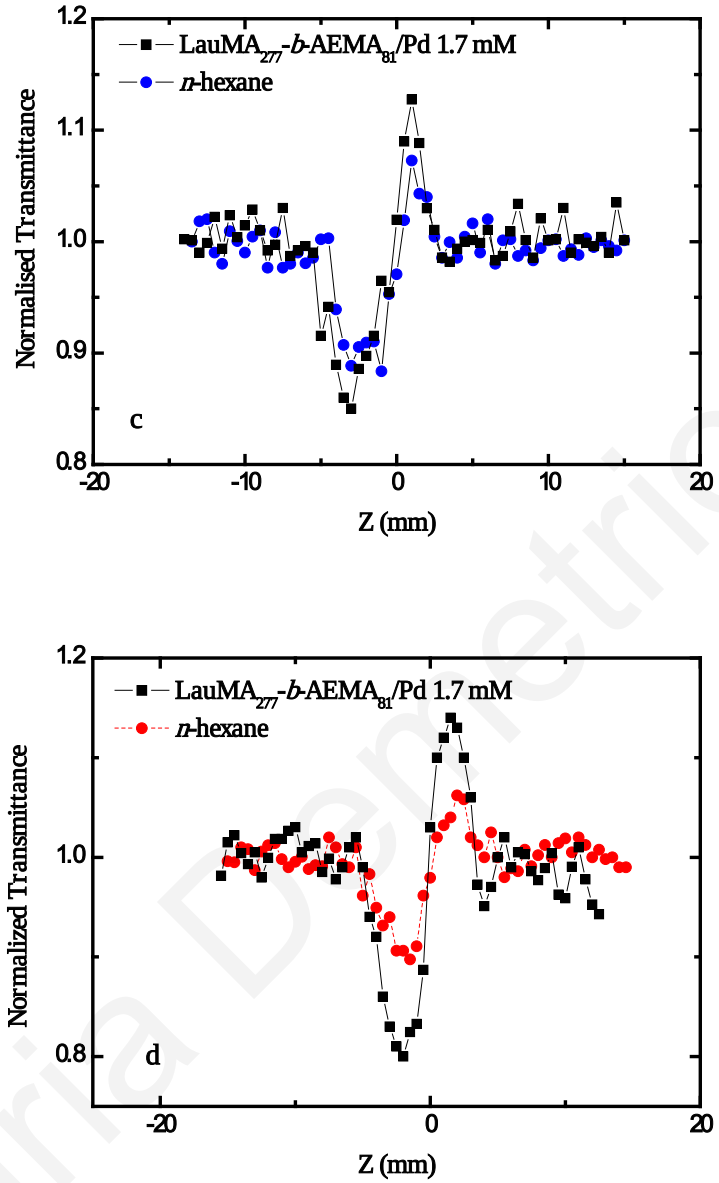

Figure 4.28: *"Open-aperture" (a, b) and divided (c, d) Z-scans of a LauMA$_{277}$-b-AEMA$_{81}$/Pd(^{0}) micellar systems having Pd(^{0}) concentration of 1.7 mM. The Z-scans (a, c) were obtained under 532 nm excitation while the Z-scans (b, d) under 1064 nm excitation.*

The determined Re$\chi^{(3)}$ and Im$\chi^{(3)}$ values of the samples as well as of the solvent (i.e. *n*-hexane) are presented in Table 4.9. In addition, the corresponding values obtained for CS_2, which was used for calibrating of the Z-scan apparatus, have been also included in the Table. From the obtained data, it becomes evident that the LauMA$_{75}$-*b*-AEMA$_{46}$/Pd(^{0}) and LauMA$_{120}$-*b*-

$AEMA_{67}/Pd(^0)$ systems were found to exhibit negligible nonlinear refraction, for both excitation wavelengths, while they exhibited measurable nonlinear absorption. In fact, the nonlinear absorption of these systems at 532 nm was found to be relatively larger than that measured at 1064 nm, following the decreasing trend of the linear absorption shown in the UV-Vis spectra (see Fig. 4.26) going from the visible to the near infrared. Concerning the $LauMA_{50}$-*b*-$AEMA_9/Pd(^0)$ and $LauMA_{277}$-*b*-$AEMA_{81}/Pd(^0)$ systems, the former was found to exhibit weak nonlinear absorption under 532 nm excitation and practically neglible nonlinear absorption at 1064 nm, while it was exhibiting nonlinear refraction at both excitation wavelengths and the latter system was found to exhibit both nonlinear refraction and absorption at both excitation wavelengths. In general, as can be seen from the values reported in Table 4.9, the various Pd-containing micellar nanohybrids were found to exhibit third-order nonlinear susceptibility values of similar magnitude, revealing a weak dependence upon the size of the micelles. Based on these findings, the studied systems can be distinguished in two classes: the $LauMA_{75}$-*b*-$AEMA_{46}/Pd(^0)$ and $LauMA_{120}$-*b*-$AEMA_{67}/Pd(^0)$ systems exhibiting nonlinear absorption and negligible nonlinear refraction and the $LauMA_{50}$-*b*-$AEMA_9/Pd(^0)$ and $LauMA_{277}$-*b*-$AEMA_{81}/Pd(^0)$ systems exhibiting both, nonlinear absorption and refraction. A possible explanation for this situation could be the different molar fraction of the AEMA ligating block (forming the micellar core) among these block copolymers. In fact, in the former systems (having diameters of 13 and 143 nm respectively), the molar fraction of the AEMA block was 0.15 and 0.23 respectively, while in the case of the latter two systems (corresponding to micelles having diameters of 21 and 36 nm respectively), the molar fraction of the AEMA block was 0.36 and 0.38. As previously mentioned, the relative sizes of the soluble and insoluble domains, together with the insoluble-soluble-ratio enforce the curvature of the assembly of block copolymers thus determining finally its shape. Specifically, the equilibration of the different interactions between the two blocks and the solvent determine the different micellar morphologies occuring e.g. spheres, cylinders, vesicles, disk like morphology etc. In that respect, the variation of the AEMA molar fraction could result in the formation of different shape micelles. Based on this, it is possible that the observed differences of the nonlinear optical response between the low and the high AEMA molar fraction systems could be because of the shape differences of these systems as visualized by AFM (Figure 4.10) i.e spherical ($LauMA_{50}$-*b*-$AEMA_9/Pd(^0)$ and $LauMA_{277}$-*b*-$AEMA_{81}/Pd(^0)$) *vs* elliptical ($LauMA_{120}$-*b*-$AEMA_{67}/Pd(^0)$ and $LauMA_{75}$-*b*-$AEMA_{46}/Pd(^0)$) micelles. Similar observations

concerning the effect of the NPs shape on their nonlinear optical response and the plasmon resonance characteristics have been reported by several groups [90,149,166,167]. For example, Murphy *et al.* [167] demonstrated that spherical NPs had single plasmon absorption band, while anisotropic nanorods had two principle plasmon absorption peaks; one at shorter wavelength corresponding to absorption and scattering of light along the short axis of the nanorod (transverse plasmon band), and the other band at longer wavelength corresponding to absorption and scattering of light along the long axis of the nanorod (longitudinal plasmon band).

Table 4.9: *Third-order nonlinear optical parameters of the $LauMA_x$-b-$AEMA_y$/$Pd(^0)$ hybrid micellar systems.*

Sample	**Size (nm)**	**Pd Content (mM)**	**1064 nm, 35 ps**		**532 nm, 35 ps**	
			Re$\chi^{(3)}$ (×10^{-13} esu)	**Im$\chi^{(3)}$ (×10^{-13} esu)**	**Re$\chi^{(3)}$ (×10^{-13} esu)**	**Im$\chi^{(3)}$ (×10^{-13} esu)**
$LauMA_{50}$-*b*-$AEMA_9$/$Pd(^0)$	13	1.23	0.12±0.03	-	0.17±0.04	0.06±0.02
		0.98	0.10±0.03	-	0.13±0.02	0.05±0.02
		0.89	-	-	0.10±0.01	0.03±0.01
$LauMA_{75}$-*b*-$AEMA_{46}$/$Pd(^0)$	21	3.2	-	0.11±0.04	-	0.13±0.02
		1.6	-	0.05±0.02	-	0.07±0.01
$LauMA_{120}$-*b*-$AEMA_{67}$/$Pd(^0)$	36	3.0		0.12±0.05	-	0.15±0.04
		1.5	-	0.05±0.02	-	0.08±0.02
$LauMA_{277}$-*b*-$AEMA_{81}$/$Pd(^0)$	143	1.7	0.14±0.05	0.07±0.02	0.11±0.03	0.09±0.03
		1.5	0.10±0.03	0.05±0.02	0.07±0.02	0.06±0.02
		1.0	-	0.04±0.01	0.03±0.01	0.04±0.01
		0.6	-	0.03±0.01	-	-
n-hexane			0.15±0.03	-	0.18±0.04	-
CS_2			5.2±0.3	-	8.4±0.4	-

For all systems studied it was found that both parts of the third-order susceptibility were linearly scaling upon Pd(^{0}) concentration. Figures 4.29-30 present the Re$\chi^{(3)}$ and Im$\chi^{(3)}$ of all investigated systems as a function of the Pd concentration under 532 and 1064 nm laser excitation.

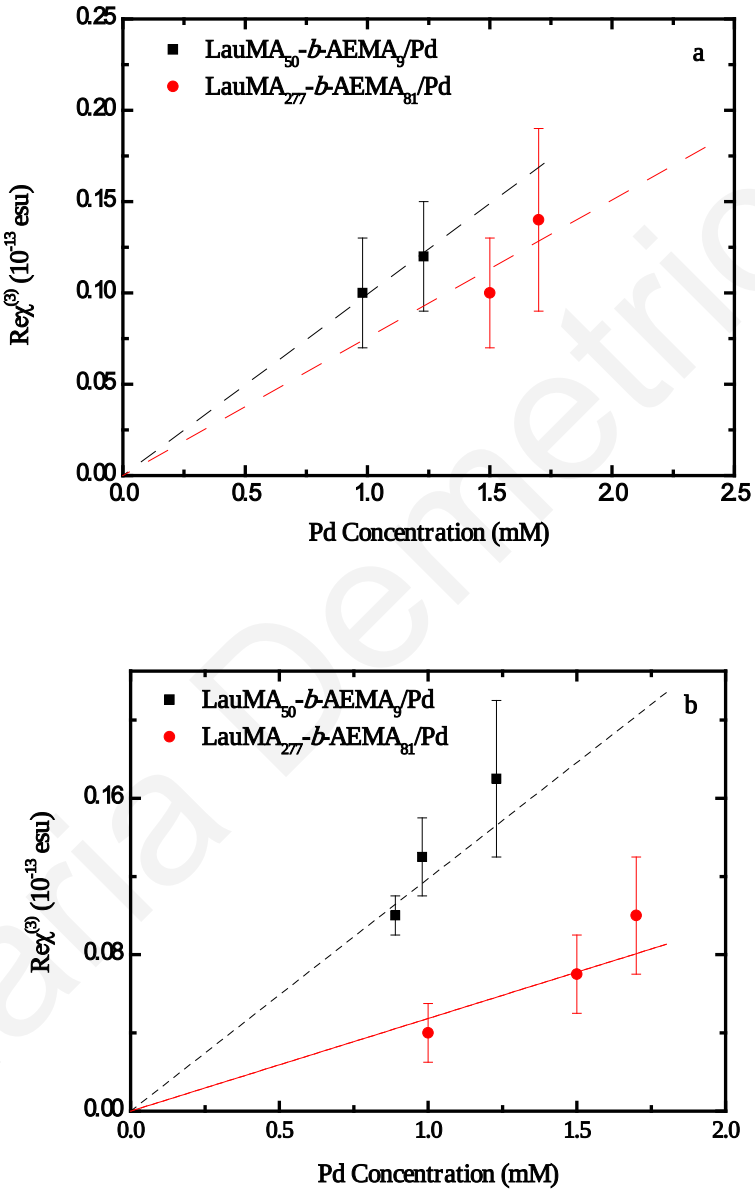

Figure 4.29: *Re$\chi^{(3)}$ values as a function of the Pd(^{0}) concentration under a) 1064 and b) 532 nm.*

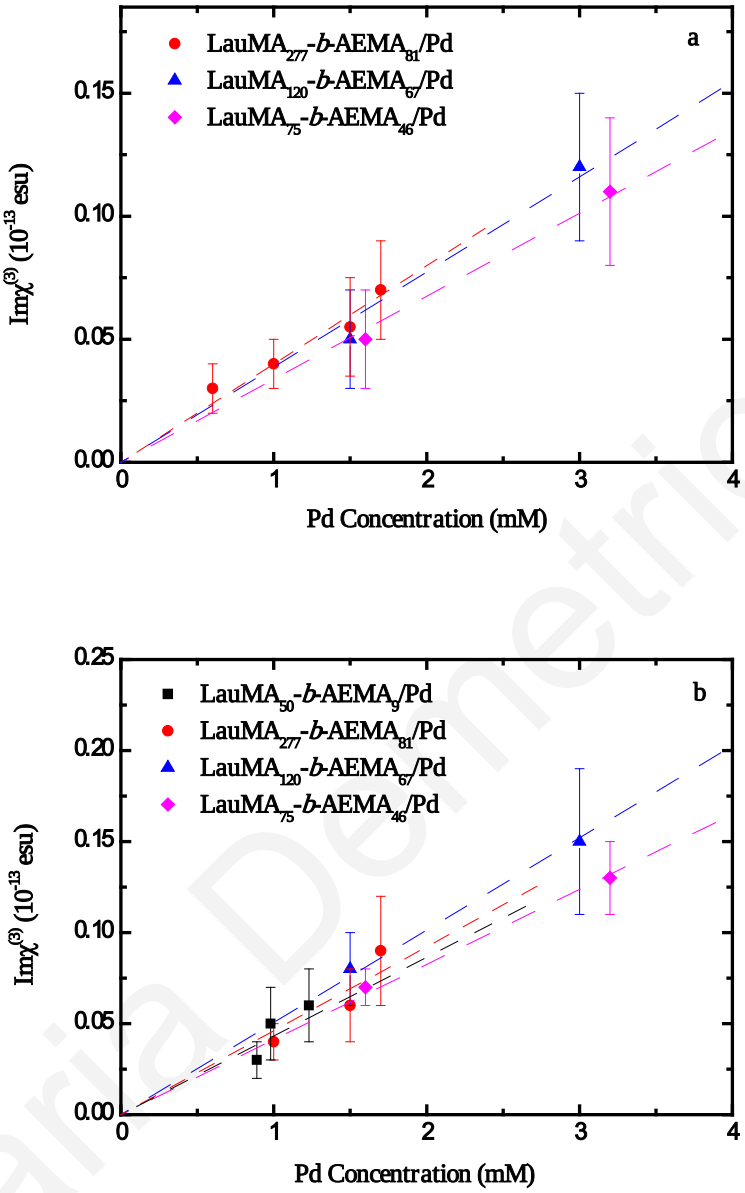

Figure 4.30: *Im$\chi^{(3)}$ values as a function of the Pd(^{0}) concentration under a) 1064 and b) 532 nm.*

4.2.1.3 Nonlinear Optical Response of the CbzEMA$_x$-b-AEMA$_y$/Pd(^{0}) Hybrid Micellar Systems [161]

The NLO response of the CbzEMA$_x$-*b*-AEMA$_y$/Pd(^{0}) systems has been investigated by means of the Z-scan technique for the systems CbzEMA$_{82}$-*b*-AEMA$_{47}$/Pd(^{0}) ([1:1] and [2:1]) and CbzEMA$_{104}$-*b*-AEMA$_{44}$/Pd(^{0}) ([1:1] and [2:1]). Similarly with the LauMA$_x$-*b*-AEMA$_y$/Pd(^{0}) hybrid systems, in order to obtain a full concentration dependence of the optical nonlinearity, several solutions of the synthesized CbzEMA$_{82}$-*b*-AEMA$_{47}$/Pd(^{0}) and CbzEMA$_{104}$-*b*-AEMA$_{44}$/Pd(^{0}) micellar systems with [AEMA:Pd(^{0})] molar ratios of [1:1] and [2:1] were prepared in THF. In Figure 4.31, the absorption spectra of the four investigated micellar systems loaded with different Pd(^{0}) concentrations are presented. As can be seen from Figure, the linear absorption of the samples was negligible at high wavelengths, while at smaller wavelengths it became sizeable. Another feature revealed from the acquired spectra is that in both cases (CbzEMA$_{82}$-*b*-AEMA$_{47}$/Pd(^{0}) and CbzEMA$_{104}$-*b*-AEMA$_{44}$/Pd(^{0})), the micellar systems containing a higher inorganic content (i.e. [AEMA]/[Pd(^{0})=1:1]), were characterized by an increased linear absorption compared to the lower inorganic content analogues. It should be also noted that the linear absorption from the copolymers that were used to encapsulate and stabilize the Pd nanoparticles began at approximately 350 nm.

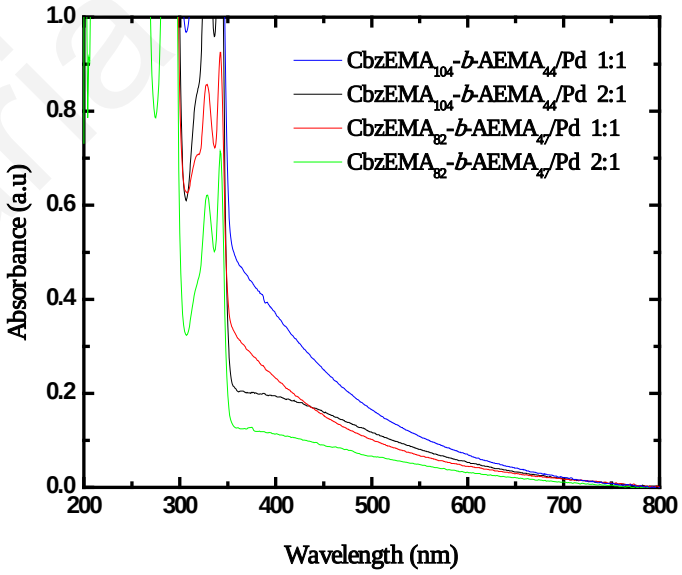

Figure 4.31: *Absorption spectra of CbzEMA$_{82}$-b-AEMA$_{47}$/Pd(^{0}) and CbzEMA$_{104}$-b-AEMA$_{44}$/Pd(^{0}) with molar ratios of AEMA units to metal ion [1:1] and [2:1].*

The samples were examined in a wide range of incident energies in order to obtain information regarding the nonlinear refraction and absorption of the investigated systems. Figure 4.32 presents the determined values of the ΔT_{p-v} parameter resulting from the "Divided" aperture Z-scan *vs* the incident energy of the laser pulse for the case of $CbzEMA_{104}$-*b*-$AEMA_{44}$/Pd(^{0}) [2:1] for both excitation wavelengths.

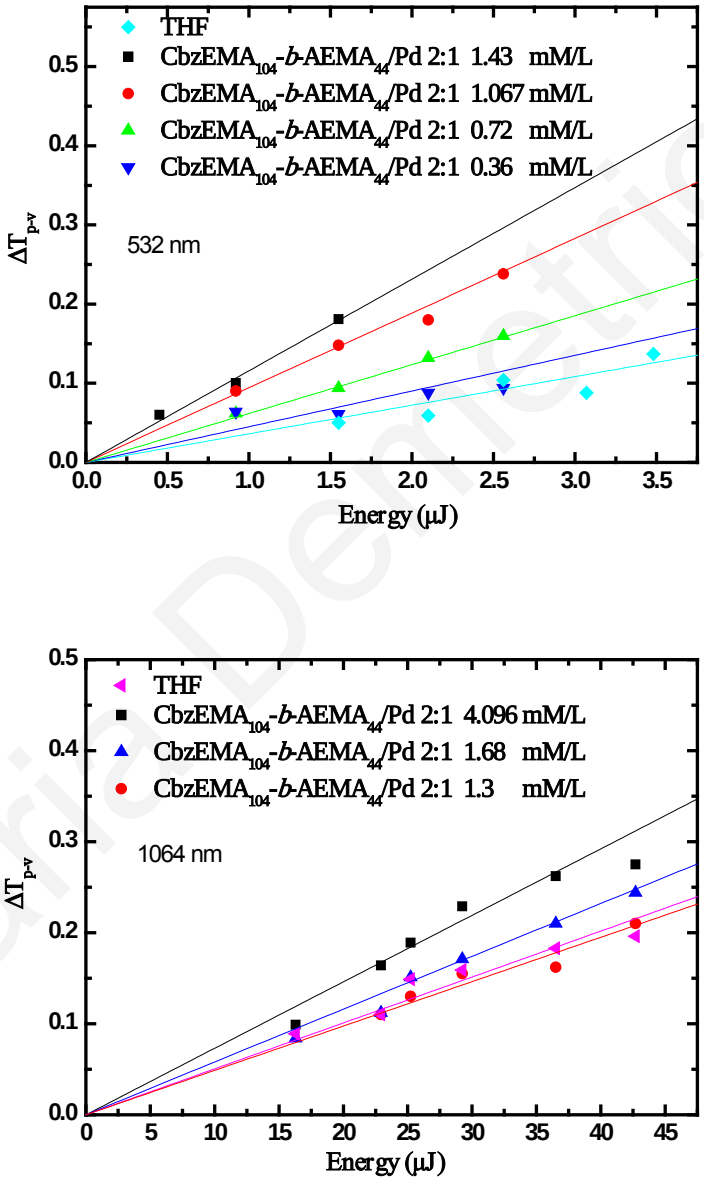

Figure 4.32: *ΔT_{p-v} values as a function of the incident laser energy for the $CbzEMA_{104}$-b-$AEMA_{44}$/Pd(^{0}) [2:1] micellar system under (a) 532 nm excitation and (b) 1064 nm excitation.*

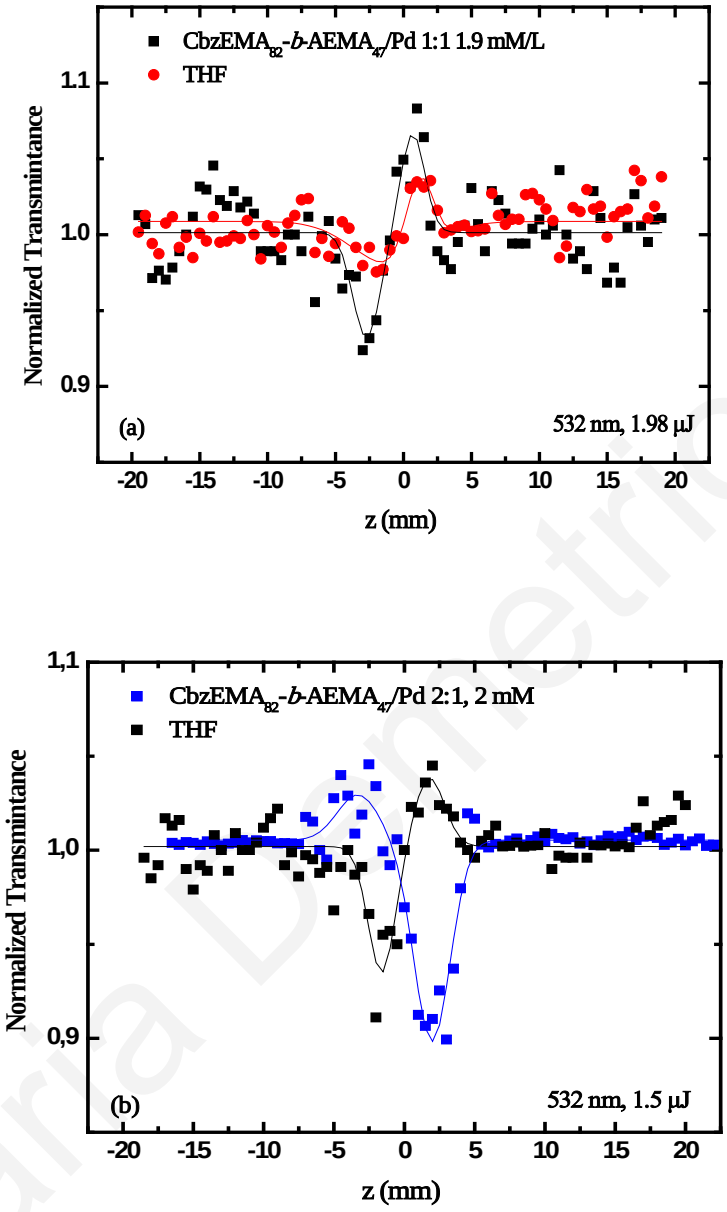

Figure 4.33: *Divided" apertures Z-scan traces for (a) CbzEMA$_{82}$-b-AEMA$_{47}$/Pd(^{0}) [1:1] system (positive nonlinear refraction) and (b) CbzEMA$_{82}$-b-AEMA$_{47}$/Pd(^{0}) [2:1] system (negative nonlinear refraction) under 532 nm excitation.*

As seen in the Figure 4.32, a good linear dependence of the signal recorded from the "Divided" Z-scan aperture with respect to the incident energy of the laser pulse exists. During the experiments it was found that the solvent used (THF) had significant contribution to the nonlinearity in both wavelengths. This contribution has been taken into account in order to

estimate the nonlinear refraction parameter γ' arising only from the micellar systems. The analysis of the obtained experimental data revealed that the values of ΔT_{p-v} of the investigated micellar systems were greater than the signals of the neat solvent. This result suggests that the samples have positive nonlinear refraction under both wavelengths and are behaving as a focusing lens. The only exception to this finding was the system CbzEMA$_{82}$-*b*-AEMA$_{47}$/Pd(^{0}) [2:1] that was found to exhibit negative nonlinear refraction when excited with a 532 nm irradiation as presented in Figure 4.33. In the same Figure, the characteristic Z-scan traces of the system CbzEMA$_{82}$-*b*-AEMA$_{47}$/Pd(^{0}) [1:1] obtained under 35 ps 532 nm excitation are also presented.

Regarding the nonlinear absorption of all micellar nanohybrids when those were excited with 35 ps laser pulses at 1064 nm, a positive nonlinear absorption was observed, demonstrating the potential use of these systems, at this particular wavelength, as optical limiters. On the contrary, when the investigation of the nonlinear optical properties was conducted at the visible region (532 nm), their behavior with respect to the nonlinear absorption was more complicated.

More specifically, from the acquired "Open" aperture Z-scan traces it has been found that the system CbzEMA$_{82}$-*b*-AEMA$_{47}$/Pd(^{0}) [1:1] exhibited positive nonlinear absorption, while the systems with a molar fraction of [2:1] presented a saturable absorber-like behavior. CbzEMA$_{104}$-*b*-AEMA$_{44}$/Pd(0) [1:1] had purely refractive nonlinearity and nonlinear absorption was not observed at least in the range of the incident intensities. This finding suggested that the nonlinear absorption of this particular micellar system was several orders of magnitude smaller than the nonlinear refraction. Figure 4.34 depicts characteristic "Open" aperture Z-scan traces for the CbzEMA$_{82}$-*b*-AEMA$_{47}$/Pd(^{0}) [1:1] and CbzEMA$_{82}$-*b*-AEMA$_{47}$/Pd(^{0}) [2:1] systems when excited with 532 nm, 35 ps. From the figure it becomes obvious that the two systems presented a different behavior for the same excitation wavelength and pulse duration.

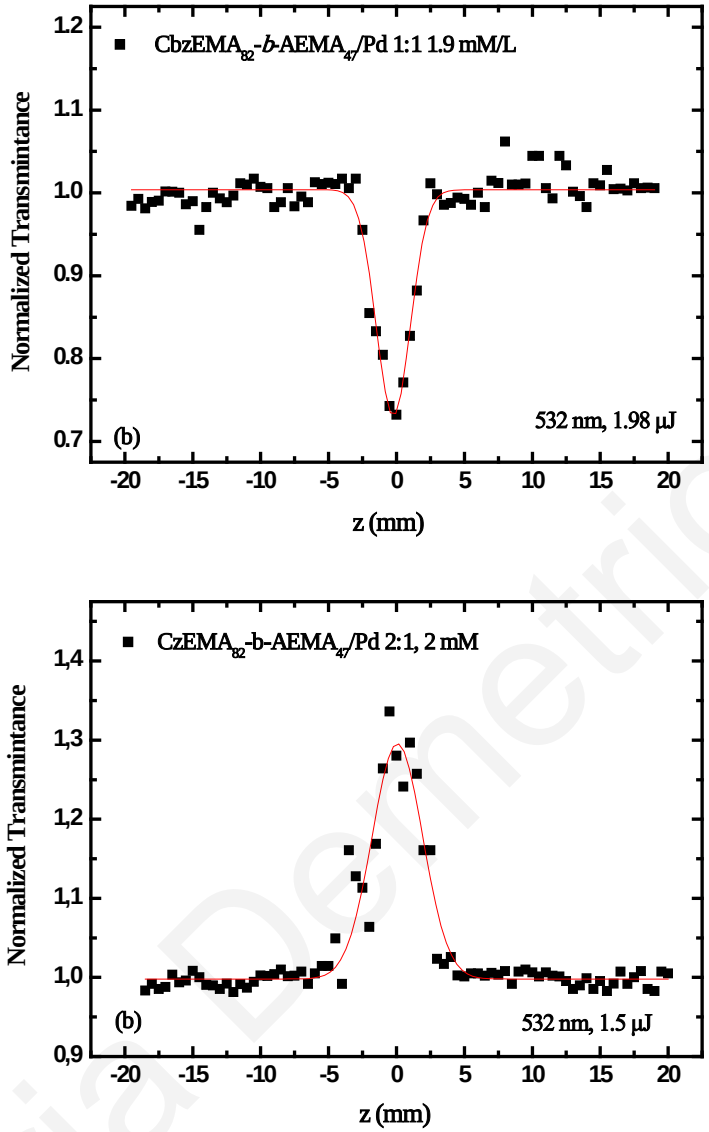

Figure 4.34: *"Open" aperture Z-scan traces, for the (a) CbzEMA$_{82}$-b-AEMA$_{47}$/Pd(^{0}) [1:1] and (b) CbzEMA$_{82}$-b-AEMA$_{47}$/Pd(^{0}) [2:1] micellar solutions having Pd(0) concentration of 1.9 mM and 2 mM respectively. The Z-scan traces (a, b) were obtained under 532 nm excitation.*

Regarding the solvent effect on the NLO response, it was observed that the solvent did not contribute to the nonlinear absorption of the investigated samples. Therefore, it may be concluded that the observed nonlinear absorption was only arising from the micellar systems. Under the same experimental conditions measurements were also carried out for the micellar solutions in the absence of metal nanoparticles i.e. only the CbzEMA$_x$-*b*-AEMA$_y$ block copolymers were present in solution. In this case no signal was recorded arising from block copolymer itself regarding nonlinear refraction or absorption.

In Table 4.9 the determined nonlinear optical parameters for all the investigated systems are presented, while for supplementary reasons the determined values for THF are also given. The γ' values for THF under 532 nm and 1064 nm excitation are $(2.1\pm0.2)\times10^{-19}$ and $(1.48\pm0.005)\times10^{-19}$ m^2/W respectively, which is in good agreement with other reports in the literature [168].

The results presented in the table show that the NLO response of the micellar systems depended on the molar ratio of polymer to metal as the systems with a ratio of [2:1] were found to exhibit saturable absorption under a 532 nm excitation. When the excitation wavelength of the laser was 1064 nm all systems had reverse saturable absorption and self-focusing action on the laser beam. In this case no particular correlation between the molar ratio and the NLO response could be found. It should be also noted that when the NLO properties of the systems were investigated at 1064 nm the magnitude of the response was one order of magnitude smaller than in the case where the investigation was carried out at 532 nm. It should be noted that under both excitation wavelengths the overall performance meaning the magnitude of $\chi^{(3)}$ of the systems is not affected by the polymer/metal molar ratio as all the systems exhibit similar response. The system with the greatest NLO response was CbzEMA$_{104}$-*b*-AEMA$_{44}$/Pd(^{0}) [1:1] when excited with 532 nm irradiation. The measured values of $\chi^{(3)}$ are $(2.27\pm0.43)\times10^{-13}$ esu when the concentration of Pd is 0.92 mM in the suspension.

It is noteworthy to mention at this point that the magnitude of Re$\chi^{(3)}$ was found to be in good agreement with recently reported values for the same wavelength regarding the LauMA$_x$-*b*-AEMA$_y$/Pd$^{(0)}$ systems [145]. In contrary, the determined values of $\chi^{(3)}$ when the investigation of the NLO response was conducted under 532 nm revealed that those systems had at least two orders of magnitude larger NLO response in comparison to LauMA$_x$-*b*-AEMA$_y$/Pd$^{(0)}$ systems [154]. Therefore, it is evident that by changing the chemical nature of the second block of the block copolymer which comprises the micellar corona, the NLO response differs. However, this must be verified by further experimental investigation in order to correlate the relation of the micellar corona to the NLO properties.

Table 4.10: *Third-order nonlinear optical parameters of the CbzEMA$_x$-b-AEMA$_y$/Pd(0) hybrid micellar systems.*

	532 nm, 35ps				1064 nm, 35ps			
	Conc. mM/L Pd	Re$\chi^{(3)}$ 10^{-14}esu	Im $\chi^{(3)}$ 10^{-14} esu	$\chi^{(3)}$ 10^{-12} esu	Conc. mM/L Pd	Re$\chi^{(3)}$ 10^{-14} esu	Im$\chi^{(3)}$ 10^{-14} esu	$\chi^{(3)}$ 10^{-14} esu
	1.89	14.7±1.4	6.5±0.9	16.1±1.6	6.48	4.9±0.02	8.2±1.6	9.5±1.6
CzEMA$_{82}$-*b*-	1.31	7.36±0.39	4.17±1.1	8.45±1.1	4.53	2.4±0.3	4.0±1.0	4.6±1.0
AEMA$_{47}$/Pd(^{0})	0.64	-	2.2±0.5	2.2±0.5	2.82	2.0±0.2	3.9±0.7	4.4±0.7
[1:1]					2.26	0.75±0.1	2.9±0.3	2.9±0.3
					1.68	-	2.5±0.8	2.5±0.8
CzEMA$_{82}$-*b*-								
AEMA$_{47}$/Pd(^{0})	2	-11.4±0.9	-5.6±0.6	12.6±1.1	4.17	1.9±0.2	5.0±0.4	5.3±0.5
	1.33	-6.8±0.5	-3.1±1.9	7.5±2.0	2.46	0.8±0.1	3.8±0.7	3.9±0.7
[2:1]	0.63	-6.5±0.4	- 1.4±0.7	6.7±0.1	1.49	0.2±0.1	2.6±0.4	2.6±0.4
CzEMA$_{104}$-*b*-	0.92	22.7±4.36	-	22.7±4.36	2.7	0.7±0.2	5.1±0.7	5.2±0.7
AEMA$_{44}$/Pd(^{0})	0.63	8.7±1.5	-	8.7±1.5	1.57	0.27±0.1	3.8±0.5	3.8±0.5
[1:1]	0.3	4.0±0.3	-	4.0±0.3	1.08	-	2.4±0.1	2.4±0.1
					0.71	-	1.9±0.1	1.9±0.1
CzEMA$_{104}$-*b*-	1.43	7.9±0.3	-3.4±1.6	8.64±1.6	4.096	1.2±0.1	6.1±0.9	6.2±0.9
AEMA$_{44}$/Pd(^{0})	1.067	5.02±0.33	-3±2	5.84±2.0	1.68	0.4±0.1	2.4±0.3	2.4±0.4
	0.72	1.8±0.4	-2.3±1.3	2.9±1.3	1.3	0.04±0.01	2.1±0.6	2.1±0.6
[2:1]	0.36	0.74±0.38	-1.34±0.68	1.5±0.7	0.794	-	1.3±0.4	1.3±0.4
THF		2.7±0.3		2.7±0.3		1.8±0.1		1.8±0.1

4.2.2 Metal Oxide Nanowire Growth

The fabrication of metal and semiconducting nanowires (NWs) has attracted considerable attention due to their potential applications arising from their one-dimensional nature and high surface-to-volume ratio. NWs are considered for providing functional diversification in integrated circuits via the integration of nanoscale devices such as nanowire LEDs, lasers, solar cells and sensors [169]. Controlling the size, shape, periodic arrangement and large-range ordering of the NWs is considered to be a key for the design and fabrication of addressable nanoscale devices and materials with specific function [170].

Many methods have been developed for the growth of NWs. Self-organized nanostructured templates offer a unique way to direct the spatial arrangement of nanomaterials in an ordered fashion. Therefore, the utilization of self-organized block copolymer nanostructures for the growth of NWs has been investigated. Ultrahigh-density NW arrays of Co and Cu have been generated by Thurn-Albrecht *et al* [171], with the use of self-assembled diblock copolymer templates, composed of poly(styrene) and poly(methyl methacrylate). By spin-casting the PS-*b*-PMMA solution, in toluene onto a conducting substrate, and then annealing the polymer film under an applied field, arrays of PMMA cylinders hexagonally packed in a PS matrix and parallel oriented to the field lines were formed. Afterwards, the PMMA domains were degraded and removed, resulting in to a nanoporous PS film which was further used for the NW growth. Crossland *et al.* [172] used a nanoporous poly(4-fluorostyrene) template, which was prepared by the electric field alignment of poly(4-fluorostyrene)-*b*-poly(D,L-lactide) (PFS-*b*-PLA) block copolymer thin films followed by mild degradation of the polylactide phase using dilute aqueous base solution, for the electrochemical growth of copper oxide (CuO) NWs. After the electrochemical growth, the template was removed by simple dissolution of the poly(4-fluorostyrene) and freestanding CuO NWs were obtained.

NWs can also be grown by the vapour liquid solid mechanism (VLS) which requires a metal nanoparticle as a catalyst. Therefore, controlling the size, shape and periodic arrangement of the metal catalyst is of key importance for the growth of nanowires and nanoscale devices with specific functions [173]. As previously mentioned, amphiphilic block copolymers are considered to be a powerful tool for the formation of stabilized MNPs within well-defined nanostructured domains, providing control of nanoparticle growth and hence of the morphological characteristics of the NWs [174]. The use of polymer-metal nanohybrids for

the development of nanowires is limited. Lu *et al* [175] have produced a monolayer of gold-containing micelles formed by the self-assembly of polystyrene-*b*-poly(2-vinylpyridine) block copolymers. Highly ordered and uniformly sized Au nanoparticles have been generated after oxygen plasma treatment used to remove the BC template. They have demonstrated that the obtained Au nanoparticles are excellent catalysts for growing silicon (Si) nanowires *via* the VLS mechanism. Specifically, highly populated, evenly distributed small-diameter (8 nm ± 0.3nm) Si nanowires of uniform size have been synthesized. Moreover, Hwang *et al.* [176] have reported the growth of single crystal ZnO NWs with diameter and length of 20-30 nm and 3-5 μm, respectively. The growth was performed on a Si substrate by controlling the area density of the catalytic Au nanoparticles reduced from $HAuCl_4.3H_2O$ in the P4VP core of PS-*b*-P4VP copolymer micelles. This was achieved by blending a solution of PS-*b*-PAA and Au loaded PS-*b*-P4VP micelles and spin coating on the substrate, in order to avoid both the formation of hybridized micelles and intermicelle diffusion of the metal nanoparticles, thereby controlling the area density of the NPs.

In this work the use of methacrylate-based polymers for the encapsulation of MNPs is considered to be advantageous since these systems are directly compatible with PMMA used in conventional lithographic Si integrated circuit processing.

4.2.2.1 LauMA$_x$-b-AEMA$_y$/Pd(^{0}) and LauMA$_x$-b-AEMA$_y$/Au Micellar Nanohybrids as Nanocatalysts for β-Ga$_2$O$_3$ Nanowire Growth **[177]**

The smallest (LauMA$_{50}$-*b*-AEMA$_9$/Pd(^{0})) and the largest (LauMA$_{277}$-*b*-AEMA$_{81}$/Pd(^{0})) micellar systems combined with either Pd(^{0}) or Au were selected for performing the NW growth. While the sizes and morphological characteristics of the Pd(^{0}) encapsulated within the LauMA$_x$-*b*-AEMA$_y$ systems were determined by TEM (Fig. 4.11), the diameter of the encapsulated Au NPs in the LauMA$_{50}$-*b*-AEMA$_9$ and LauMA$_{277}$-*b*-AEMA$_{81}$ systems, were determined by UV-*vis* based on the Surface Plasmon Resonance (SPR) band. Assuming a spherical morphology, the Au NP diameters were determined to be ~13 and 100 nm respectively [178]. Figure 4.35 shows the UV-*vis* spectra of the two systems recorded in *n*-hexane.

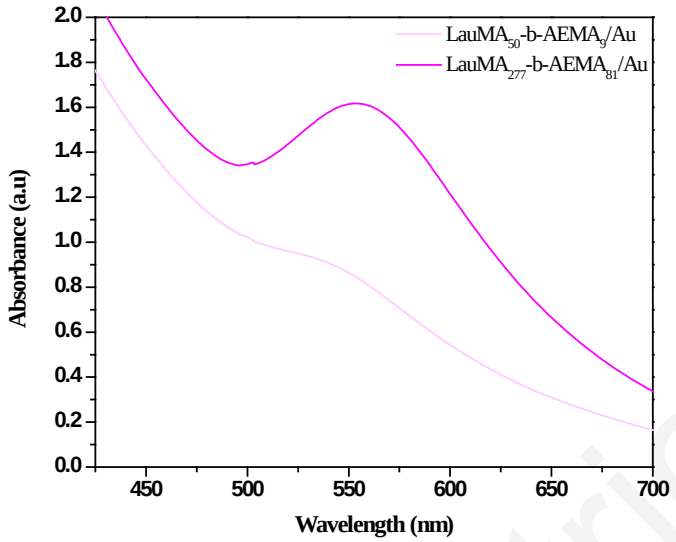

Figure 4.35: *Absorption spectra of the two different Au-containing micellar systems recorded in n-hexane: (i) LauMA$_{50}$-b-AEMA$_9$/Au and (ii) LauMA$_{277}$-b-AEMA$_{81}$/Au.*

Ga_2O_3 NWs were previously grown on a Si (001) substrate, with diameters of 50 nm and lengths of several tens of μm, using a thin layer of 0.7 nm Au as a catalyst. Similarly, in the present work *β*-Ga_2O_3 NWs with diameters of few tens of nm and lengths > 10 μm were obtained *via* drop casting of the LauMA$_{277}$-b-AEMA$_{81}$/Au micellar solution (polymer concetration = 1790 mg/L) on Si (001) (CVD677). In Figure 4.36, the SEM images of the *β*-Ga_2O_3 NWs grown by using either a thin Au layer or LauMA$_{277}$-b-AEMA$_{81}$/Au as catalyst are presented. The SEM image in Figure 4.36 (b) demonstrates the successful use of these micellar nanohybrids as nanocatalysts for β-Ga_2O_3 NW growth. The crystalline phase of the NWs was confirmed by XRD. As seen in the XRD spectrum (Figure 4.37) the peaks correspond to the monoclinic crystal structure of *β-Ga_2O_3* are present.

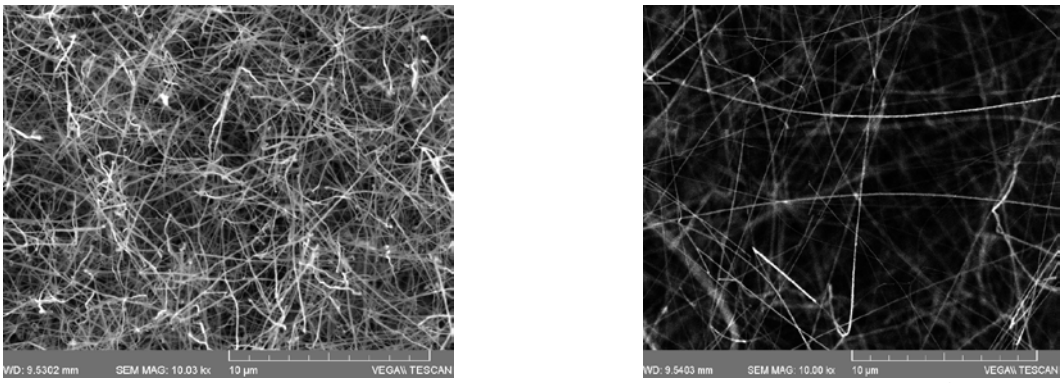

(a) **(b)**

Figure 4.36: *(a) SEM image of β-Ga_2O_3 NWs obtained on Si (001) coated with a layer of 0.7 nm Au (b) Similar β-Ga_2O_3 NWs obtained on Si(001) using Au NPs embedded inside the $LauMA_{277}$-b- $AEMA_{81}$ micelles (polymer concentration=1790 mg/l).*

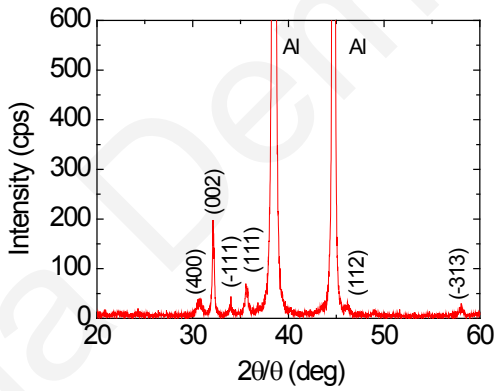

Figure 4.37: *XRD of the β-Ga_2O_3 NWs obtained on Si (001) using $LauMA_{277}$-b-$AEMA_{81}$/Au as nanocatalysts.*

In contrast to the above, the use of $LauMA_{50}$-*b*-$AEMA_9$/Pd(^{0}) or $LauMA_{50}$-*b*-$AEMA_9$/Au micellar solution spin-coated on Si (001) (Table 3.5), leads to the growth of much more complex nanostructures, such as unusual necklace like nanostructures and ultrathin rectangular plate like nanostructures (Figure 4.38). No systematic trend in the morphology of these complex nanostructures was observed by increasing the spin coating speed or by changing the polymer concentration in the range 696-11400 mg/l as listed in Table 3.5 (Experimental section). However a further reduction in the polymer concentration leads to the disappearance

of these complex nanostructures and appearance of short β-Ga_2O_3 nanobelts instead. β-Ga_2O_3 nanobelts were also observed in the case where the growth was carried out on plain Si (001) and Si (001)/$LauMA_{277}$ -b- $AEMA_{81}$.

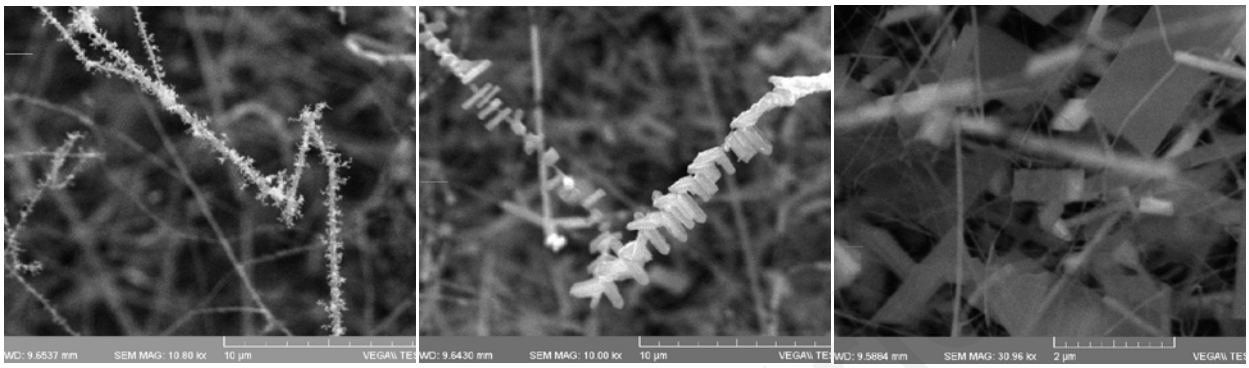

Figure 4.38: *Morphologies of β-Ga_2O_3 NWs obtained by using $LauMA_{50}$-b-$AEMA_9$/Au and $LauMA_{50}$-b-$AEMA_9$/Pd nanocatalyst systems (SEM images).*

In an effort to evaluate the effect of a porous template on the NW assembly, $LauMA_{277}$ -b-$AEMA_{81}$/Au solution was spin coated onto a porous alumina template followed by NW growth. As seen in Figure 4.39, short β-Ga_2O_3 nanorods were obtained which are partially oriented suggesting that the use of these nanohybrids in conjunction with nanostructured templates is an effective way for the directed assembly of semiconductor NWs.

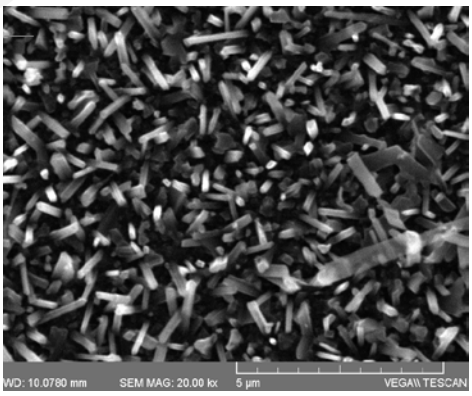

Figure 4.39: *SEM image of β-Ga_2O_3 NWs obtained on a porous alumina template using $LauMA_{277}$ -b- $AEMA_{81}$/Au (polymer concentration=11400 g/L).*

Photoluminescence spectroscopy was employed to evaluate the optical properties of the NWs. The PL spectra of the β-Ga_2O_3 NWs grown using the polymer-based nanohybrids as catalyst was less broad and blue shifted, as shown in Figure 4.40 (b), in contrast to the broad-symmetric PL observed in the case of the β-Ga_2O_3 NWs grown using a thin layer of Au in Figure 4.40 (a). This blue shifting is attributed to quantum confinement.

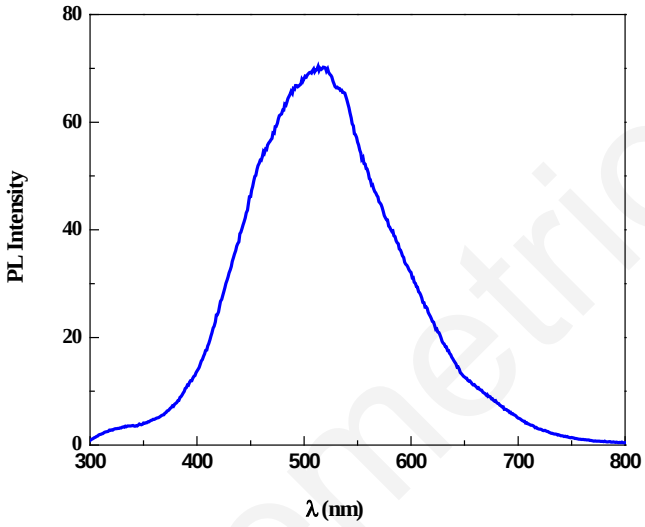

(a)

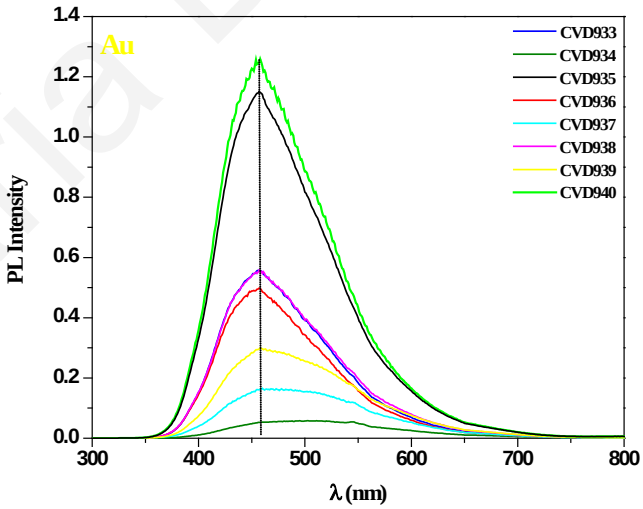

(b)

Figure 4.40: *Photoluminescence of the β-Ga_2O_3 NWs obtained on Si (001) using the (a) 0.7 nm Au thin layer and (b) the $LauMA_{50}$-b-$AEMA_9$/Au as nanocatalyst.*

Additionally, ZnO NWs were also grown using the smallest nanohybrid system $LauMA_{50}$-b-$AEMA_9$/Au. In contrast to β-Ga_2O_3 NWs grown under the same experimental conditions, the obtained ZnO NWs did not exhibit complex nanostructures. The ZnO NWs were short with well defined facets and a hexagonal crystal structure (Figure 4.41).

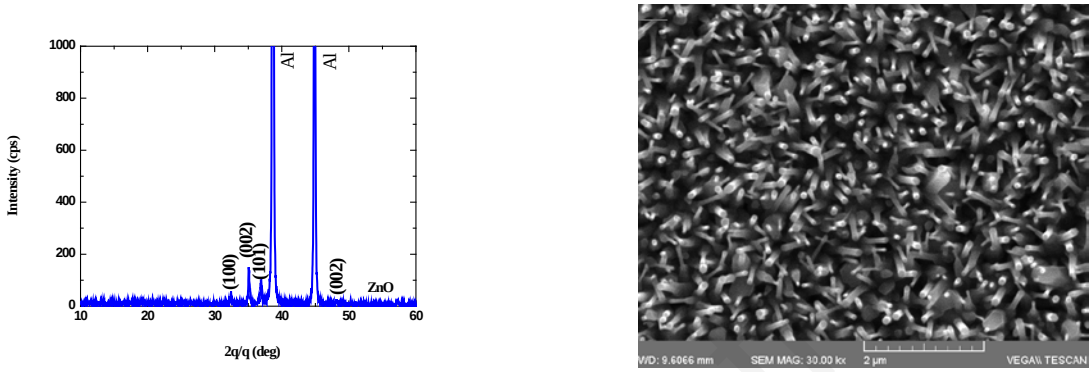

(a) **(b)**

Figure 4.41: *(a) XRD spectrum of the ZnO NWs obtained with $LauMA_{277}$-b-$AEMA_{81}$ on Si(001). (b) SEM image of ZnO NWs obtained using $LauMA_{50}$-b-$AEMA_9$/Au nanocatalyst.*

4.2.3 Fluorescence Sensing

The anthracene-containing polymers were also evaluated towards their ability to act as effective dual chemosensors (i.e. amino- and metal ion sensors) in organic media. This unique capability derives from the combination of a fluorescent group (anthracene) with a metal ion ligating group (β-ketoester) within the same system. More precisely, electron donating groups such as amines located in the proximity of anthracene moieties result in a drastic decrease in the fluorescence intensity of anthracene due to electron transfer phenomena occurring between the lone electron pair of the amines and the photoexcited anthracene units [179]. Moreover, the presence of metal cations was found to significantly affect the fluorescence signal of the anthracene moieties. Numerous examples appear in the literature describing the chemo-sensing ability of small molecules combining a fluorescent group with a metal binding moiety [180]. Currently, the design and synthesis of polymer-based metal ion sensors combining fluorescent and metal-chelating groups presents high interest. Polymer-based metal ion sensors have been reported by various groups [181]. However, most of the developed systems

are homopolymers characterized by a structural complexity and demanding synthetic methodologies towards their preparation. In the present work a simple and cost-effective synthetic approach involving a controlled radical polymerization process was employed towards this purpose.

4.2.3.1 Fluorescence sensing towards amines

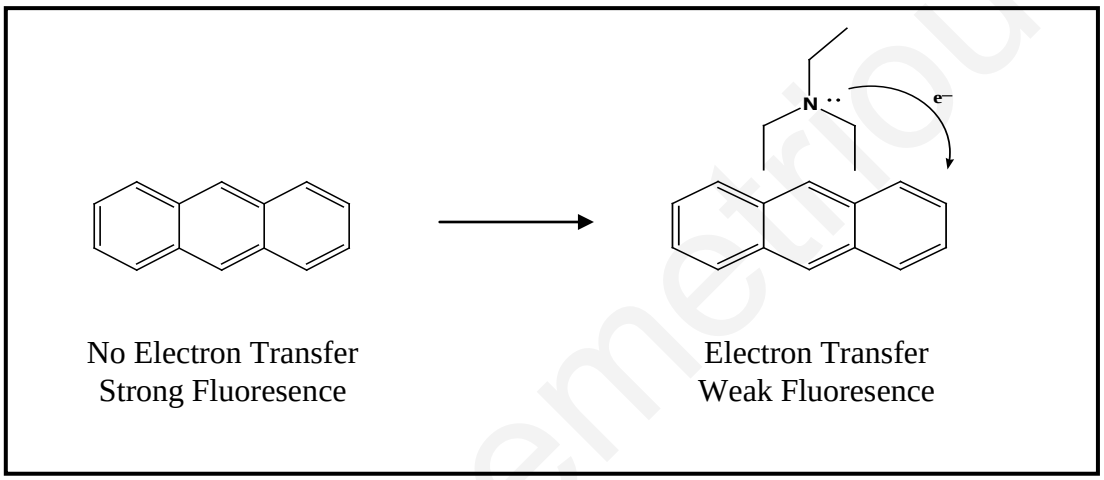

Figure 4.42: *Schematic representation of the electron transfer mechanism between athracene and amine moieties.*

In this work, the $AnMMA_{36}$ and $AEMA_{42}$-*b*-$AnMMA_{83}$ systems were examined towards their ability to act as macromolecular sensors for triethylamine in organic solvents. For this purpose, the fluorescence intensity of a polymer solution (polymer concentration based on anthracene groups) was monitored in the presence of various concentrations of triethylamine (ranging from 3.6 mM to 1 M). The presence of Et_3N at a much higher concentration compared to the concentration of the anthracene moieties (10^{-4} M) within the polymers renders the electron transfer possible (Figure 4.42). As seen in Figure 4.43, an increase in the amount of the amine present in solution caused a significant decrease in the fluorescence intensity.

It should be noted that the possibility of electron transfer from the anthracene groups to chloroform molecules is not possible [182]; hence the fluorescence quenching is because of the electron transfer of the electron lone pair of triethylamine to the anthracene moieties.

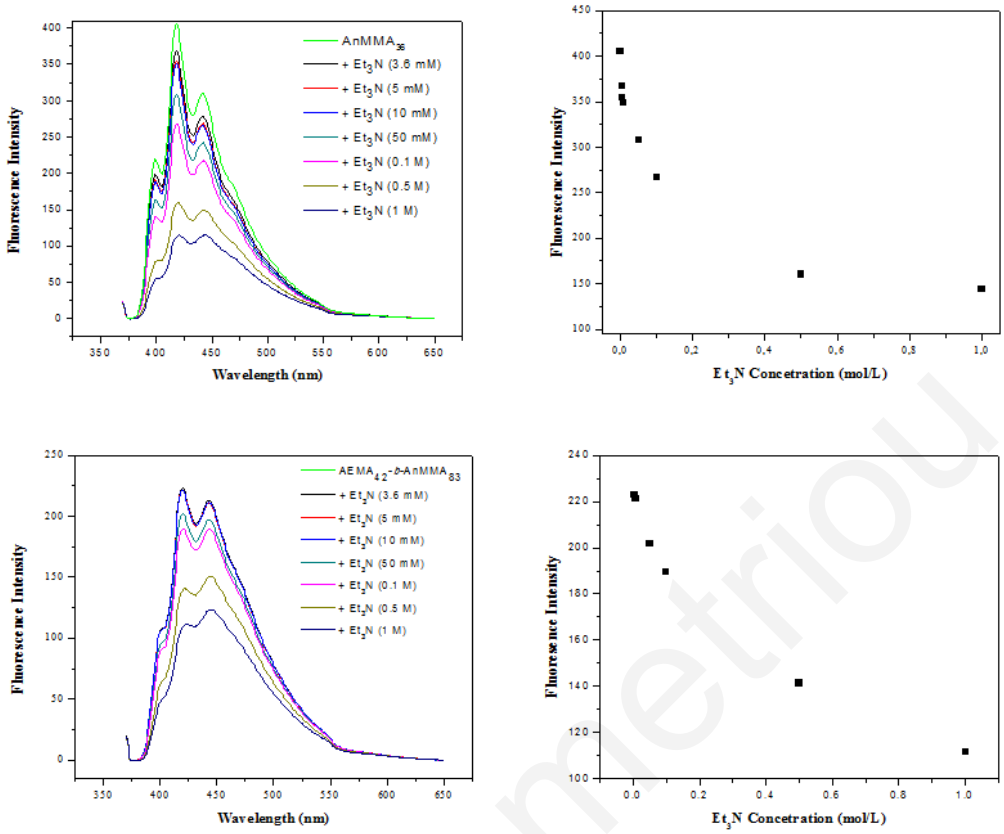

Figure 4.43: *(a) $AnMMA_{36}$ and (b) $AEMA_{42}$-b-$AnMMA_{83}$ fluorescence spectra recorded in chloroform in the presence of different quencher (Et_3N) concentrations, ranging from 3.6 mM to 1 M.*

4.2.3.2 Fluorescence sensing towards metal ions

As shown previously, block copolymers bearing *β*-ketoester groups within their structure are capable of complexing and solubilizing different metal-ion salts in organic media. As aforementioned, the *β*-ketoester moiety exists in two tautomeric forms (the keto and the enol) which are in equilibrium. For these systems, the ^1H NMR spectra recorded in $CDCl_3$ (an example is presented in Figure 4.21) showed that the keto tautomer is the dominant one.

The ability of the $AEMA_x$-*b*-$AnMMA_y$ diblock copolymers towards metal ion sensing (Fe(III)) has been investigated in chloroform. Chloroform is a common solvent for AEMA and AnMMA blocks and hence the polymer exists only as unimers in solution. Upon $FeCl_3.H_2O$ addition in the solution, a colour change was observed within a few seconds from light yellow to deep wine red, caused by the complex formation between the Fe(III) ion and the β-ketoester

groups. Presumably, as shown in Figure 4.44, the octahedral structure of the ferric salt is preserved and only the four water molecules adjacent to the iron atoms are replaced by two keto tautomeric *β*-ketoester ligands. Figure 4.45 presents the UV-Vis spectrum of the $AEMA_{42}$-*b*-$AnMMA_{83}/FeCl_3.6H_2O$ complex in chloroform. In the spectrum, the signal appearing at 550 nm confirmed the complex formation [15].

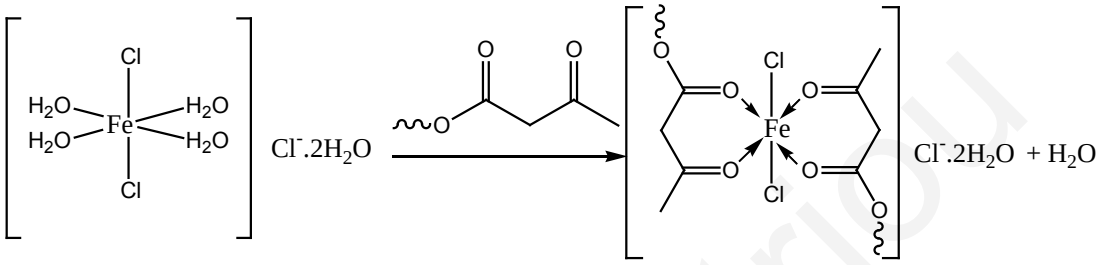

Figure 4.44: *Substitution of "L" type of ligand molecules (H_2O) in $FeCl_3{\cdot}6H_2O$ by the "keto" form of the β-ketoester group.*

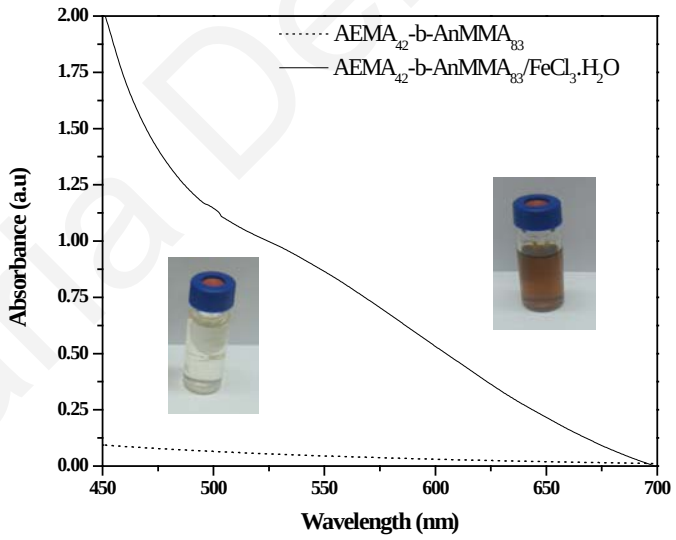

Figure 4.45: *UV-Vis spectrum of the $AEMA_{42}$-b-$AnMMA_{83}$ /$FeCl_3.6H_2O$ complex formed by the keto form of the β-ketoester ligands in chloroform.*

It must be noted that chloroform is a good solvent for the $FeCl_3.6H_2O$ salt and in an excess, chloroform favors de-complexation. This was indicated by a colour change of the solution upon dilution, from wine red to yellow/orange (colour of $FeCl_3{\cdot}6H_2O$ in $CHCl_3$).

It is noteworthy to emphasize at this point the importance of the use of a block copolymer structure towards Fe(III) sensing in this particular solvent, since, as previously demonstrated [15], complexation of $FeCl_3.6H_2O$ performed in chloroform using poly(butyl methacrylate)-*block*-poly((2-acetoacetoxy)ethyl methacrylate) ($BuMA_x$-*b*-$AEMA_y$), revealed that the coordination of the Fe(III) onto the $AEMA_y$ segment reduced its solubility in that particular solvent. The latter resulted to the formation of aggregates consisting of a poly(AEMA)-metal ion core and a poly(BuMA) corona. Therefore, it is expected that in the case of a random copolymer consisting of AnMMA and AEMA units, the complexation of Fe(III) ions with the latter will cause the destabilization of the random copolymer chains in solution due to the fact that these are not capable of self-organizing into soluble core-shell micellar nanostructures.

Based on the above, it was expected that in the case of the $AEMA_x$-*b*-$AnMMA_y$/Fe(III) systems, micellar nanostructures would be generated in solution, consisting of a poly(AEMA)-Fe(III) core. It is assumed that this self-organized micellar nanoenvironment leads to the confinement of the complexed transition metal ion and of the fluorescent moieties within nanosized domains, reinforcing the interaction between the two, thus promoting chelation enhanced fluorescence quenching.

Figure 4.46 presents the fluorescence quenching curves recorded in chloroform at 368 nm excitation wavelength (λ_{exc}) as a function of the concentration of the Fe(III) salt. As seen in the graphs, a drastic decrease in the fluorescence intensity was observed upon complexation. As expected, the quenching effect on the anthracene chromophore was further enhanced upon increasing the salt concentration in the system. These results are in agreement with similar observations reported by other groups [183] and have been attributed to the presence of unpaired d electrons in transition metal ions that can effectively quench the anthryl chromophore. According to Buruiana et al. [182] the quenching processes that can take place in anthracene-containing systems may involve different quenching mechanisms namely excimer or exciplex formation, metal-π complex, electron transfer and energy transfer. Paramagnetic metal ions such as Fe(III) (d^5) possessing unpaired d electrons, when present at high concentrations lead to an effective quenching of the anthracene fluorescence. The possible quenching mechanism in the $AEMA_x$-*b*-$AnMMA_y$/Fe(III) systems may involve the energy transfer from the singlet excited-state anthracene chromophores to the low-lying half-filled 3d orbitals of the Fe(III) paramagnetic cation [184]. Furthermore, the decrease in the fluorescence intensity was accompanied by a blue shifting in the spectrum. Blue shifts in the

fluorescence spectra were previously observed upon complexation of Fe^{3+} as well as other metal ions including Pb^{2+}, Fe^{2+}, Cu^{+}, Sb^{3+} and lanthanides with polymers [185].

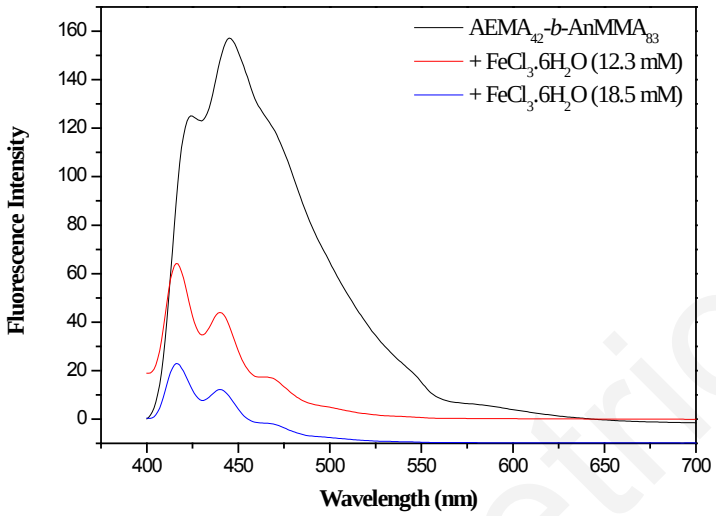

Figure 4.46: *$AEMA_{42}$-b-$AnMMA_{83}$ fluorescence spectra recorded in chloroform in the presence of different quencher ($FeCl_3.6H_2O$) concentrations (12.3 mM and 18.5 mM).*

SUMMARY AND OUTLOOK

In the present work, three families of well-defined, functional diblock copolymers were synthesized for the first time *via* RAFT polymerization. All diblock copolymers were based on a ligating block segment, possessing β-ketoester functionalities, therefore the differentiation of the three families has been provided by changing the chemical nature of the second block segment. A series of well-defined LauMA$_x$-*b*-AEMA$_y$ (4 in total), CbzEMA$_x$-*b*-AEMA$_y$ (4 in total), AEMA$_x$-*b*-AnMMA$_y$ (3 in total) diblock copolymers of various chemical compositions, were successfully prepared by RAFT and characterized by employing various characterization methods. SEC and ^{1}H NMR was employed for determining their molecular characteristics and TGA and DSC for obtaining information in regards to their thermal properties.

The aggregation behavior of the LauMA$_x$-*b*-AEMA$_y$ diblock copolymers was investigated in *n*-hexane, a selective solvent for the LauMA$_x$ block by DLS. These systems are capable of forming micellar nanomorphologies, consisting of a LauMA$_x$ solvating corona and an AEMA$_y$ core, in *n*-hexane. By varying the block lengths of the two segments within the block copolymer, micelles of tunable diameters were obtained (ranging from 37-181 nm). The above-mentioned diblock copolymer micelles have been employed for the first time as nanocontainers for the encapsulation and stabilization of Pd MNPs in organic media, towards the fabrication of polymer-metal micellar hybrid systems. The presence of strong *β*-ketoester ligands in the diblock copolymers allowed the stabilization of the Pd MNPs by the complexation of Pd(II) ions with the *β*-ketoester moieties followed by the reduction of the Pd(II) ions to Pd(^{0}). In the case of the CbzEMA$_x$-*b*-AEMA$_y$ and AEMA$_x$-*b*-AnMMA$_y$ diblock copolymers, the micelle formation in THF, which is a non-selective solvent for the CbzEMA, AEMA and AnMMA block segments resulted upon the addition of Pd salt, followed by the reduction of Pd(II) ions into Pd(^{0}). The resulting polymer/Pd(^{0}) hybrid micelles consisted of a CbzEMA$_x$ or AnMMA$_y$ corona and an insoluble AEMA$_x$/Pd(^{0}) core.

All micellar nanohybrids were characterized by various techniques. DLS was employed for the determination of their D_Hs, while AFM and TEM for the visualization of their morphology and determination of the MNPs sizes. The D_Hs of the LauMA$_x$-*b*-AEMA$_y$/Pd(^{0}) micellar

nanohybrids ranged from 21 to 143 nm, the D_Hs of the CbzEMA$_x$-*b*-AEMA$_y$/Pd(^{0}) depending on metal loading ranged from 70-115 nm while the D_Hs of the AEMA$_x$-*b*-AnMMA$_y$/Pd(^{0}) systems were found to range between ~ 70 - ~ 95 nm. Depending on the block length within the diblock copolymers, micellar hybrids of tunable diameters and with different shapes can be obtained leading to control over the NP size and shape.

The Z-scan technique was employed for the measurement of the NLO absorption and refraction of the hybrid systems as well as the determination of the third-order nonlinear susceptibility $\chi^{(3)}$ in the visible (532 nm) and in the infrared (1064 nm). The effect of different parameters characterizing the hybrid systems (e.g. the size of the macromolecular aggregates, the chemical structure and molecular characteristics of the block copolymers) on the NLO response was also evaluated. At this point, it is worthy to note that to the best of our knowledge, there is no example appearing in the literature describing the NLO response of Pd NPs encapsulated in amphiphilic block copolymer micelles. The LauMA$_{75}$-*b*-AEMA$_{46}$/Pd(^{0}) nanohybrid systems exhibit low NLO response (10^{-15}-10^{-14} esu), with similar magnitude of NLO response in the visible and in the infrared. Additionally, their NLO response was not found to be size dependent. In contrast, the CbzEMA$_x$-*b*-AEMA$_y$/Pd(^{0}) hybrid systems exhibit large NLO response (~10^{-11}-10^{-12} esu), with a significantly higher NLO response in the visible than in the infrared and larger NLO refraction than NLO absorption, while their NLO response was found to depend on the nanoparticle size.

The smallest and the largest LauMA$_x$-*b*-AEMA$_y$ diblock copolymers were also used for the encapsulation and stabilization of Au NPs in *n*-hexane. The resulting micellar nonohybrids were characterized by UV-*vis* for the determination of Au NPs size (13 nm and 100 nm). It was demonstrated that the hybrid systems based on lauryl-containing polymers and Pd(^{0}) or Au NPs can be effectively used as nanostructured catalysts for the growth of thin semiconductor metal-oxide nanowires (β-Ga_2O_3 or ZnO NWs) either on a Si (001) substrate or on a porous alumina membrane.

Moreover, the anthracene-containing polymers were evaluated toward their ability to act as effective dual chemosensors (i.e. amino- and metal ion sensors) in organic media. More precisely, the fluorescence intensity of both, the AnMMA$_x$ homopolymers and the AnMMA$_x$-

b-$AEMA_y$ diblock copolymers in solution exhibited a significant decrease in the presence of triethylamine. Moreover, the presence of iron (III) cations were also found to significantly affect the fluorescence signal of the anthracene moieties when those were combined in a block copolymer structure with the AEMA units, due to complex formation occurring between the *β*-ketoester groups of the $AEMA_x$ segment and the cations.

Future work could include:

(a) The fabrication of polymer-metal nanohybrid nanostructured thin films and the investigation of their NLO properties. This might create the possibility of designing a device that can act as an optical limiter. Furthermore, NLO theoretical investigation analysis for extracting information regarding the relation of the chemical nature of the micellar corona to the NLO response can be also carried out.

(b) The methacrylate-based MNPs can be patterned *via* electron beam lithography and used for metal oxides NWs selective growth at specific sites.

(c) The Pd-containing micellar nanohybrids can be evaluated towards their catalytic properties and their further use in nanocatalysis.

REFERENCES

[1] V. Rotello, *Nanoparticles – Building Blocks for Nanotechnology* **2004**, Springer.

[2] C.Muller, M. G. Nijkamp, D. Vogt, *European Journal of Inorganic Chemistry* **2005**, 20, 4011.

[3] H. Schlaad, T. Krasia, *Macromolecules* **2001**, 34, 7585.

[4] N. Savage, M. S. Diallo, *Journal of Nanoparticles Research* **2005**, 7, 331.

[5] J. Pyun, *Polymer Reviews* **2007**, 47, 231.

[6] (a) L. A. Harris, J. D. Goff, A. Y. Carmichael, J. S. Riffle, J. J. Harburn, T. G. St. Pierre, M. Saunders, *Chemistry Materials* **2003**, 15, 1367. (b) S. P. Leary, C. Y. Liu, M. L. I. Apuzzo, *Neurosurgery* **2006**, 58, 1009.

[7] (a) H. Zhao, E. P. Douglas, B. S. Harrison, K. S. Schanze, *Langmuir* **2001**, 17, 8428. (b) W. Cheng-Chien, C. An-Liu,C. I-Han, *Journal of Colloid Interface Science* **2006**, 293, 421.

[8] (a) J. Chai, D. Wang, X. N. Fan, J. M. Buriak, *Natural Nanotechnology* **2007**, 2, 500. (b) S. Krishnamoorthy, C. Hinderling, H. Heinzelmann, *Materials Today* **2006**, 9, 40.

[9] D. M. Schaadt, B. Feng, E. T. Yu, *Applied Physics Letters* **2005**, 86, 063106-1-3.

[10] Z. Tian, W. Huang, D. Xiao, S. Wang, Y. Wu, Q. Gong, W. Yang, J. Yao, *Chemical Physics Letters* **2004**, *391*, 283.

[11] (a) R. B. Grubbs, *Journal of Polymer Science: Part A: Polymer Chemistry* **2005**, 43, 4323. (b) R. B. Grubbs, *Polymer Reviews* **2007**, 47, 197.

[12] R. Shenhar, T. B. Norsten, V. M. Rotello, *Advanced Materials* **2005**, *17*, 657.

[13] S. Förster, M. Antonietti, *Advanced Materials* **1998**, 10, 195.

[14] R. C. Mehrotra, B. Bohra, D. P. Gaur, *Metal β-Diketonates and Allied Derivatives* **1978**, Academic Press, New York.

[15] T. Krasia, H. Schlaad, *ACS Symposium Series* **2006**, 928, 157.

[16] B. Erman, M. M. Demir, M. A. Gulgun, Y. Z. Menceloglu, S. S. Abramchuk, E. E. Makhaeva, A. R. Khokhlov, V. G. Matveeva, M. G. Sulman, *Macromolecules* **2004**, 37, 1787.

[17] R. A. Ganeev, *Journal of Optics A: Pure and Applied Optics* **2005**, 7, 717.

[18] E. Xenogiannopoulou, K. Iliopoulos, S. Couris, T. Karakouz, A. Vaskevich, I. Rubinstein, *Advanced Functional Materials* **2008**, 18, 1281.

[19] E. Xenogiannopoulou, P. Aloukos, S. Couris, E. Kaminska, A. Piotrowska, E. Dynowska, *Optics Communication* **2007**, 275, 217.

[20] D. Astruc, *Inorganic Chemistry* **2007**, 46, 1884.

[21] M. Yamauchi, H. Kitagawa, *Synthetic Metals* **2005**, 153, 353.

[22] Z. H. Chen, J. S. Jie, L. B. Luo, H. Wang, C. S. Lee, S. T. Lee, *Nanotechnology* **2007**, 18, 1.

[23] B. Sampedro, A. Hernando, *Physica Status Solidi* **2004**, 12, 3670.

[24] R. A. Ganeev, M. Suzuki, M. Baba, M. Ichihara, H. Kuroda, *Journal of Applied Physics* **2008**, 103, 063102.

[25] J. Ebothe, I. V. Kityk, G. Chang, M. Oyama, K. J. Plucinski, *Physica E* **2006**, 35, 121.

[26] H. Zeng, Y. Yang, X. Jiang, G. Chen, J. Qiu, F. Gan, *Journal of Crystal Growth* **2005**, 280, 516.

[27] (a)Y. Piao, Y. J. Jang, M. Shokouhimehr, I. S. Lee, T. Hyeon, *Small* **2007**, 3, 255. (b) M. A. R. Meier, M. Filali, J. F. Gohy, U. S. Schubert, *Journal of Materials Chemistry* **2006**, 16, 3001, (c) N. V. Semagina, A. V. Bykov, E. M. Sulman, V. G. Matveeva, S. N. Sidorov, L. V. Dubrovina, P. M. Valetsky, O. I. Kiselyova, A. R. Khokhlov, B. Stein, L. M. Bronstein, *Journal of Molecular Catalysis A: Chemical* **2004**, 208, 273, (d) D. M. Chernyshov, L. M. Bronstein, H. Börner, B. Berton, M. Antonietti, *Chemistry of Materials* **2000**, 12, 114.

[28] P. Alexandridis, *Current Opinion of Colloid Interface Science* **2000**, 5, 312.

[29] H. Wang, H. Wang, V. S. Urban, K. C. Littrell, P. Thiyagarajan and L. Yu, *Journal of the American Chemical Society* **2000**, 122, 6855.

[30] R. J. Spontak and P. Alexandridis, *Current Opinion of Colloid Interface Science* **1999**, 4, 140.

[31] H. R. Allcock, F. Lampe, J. E. Mark, *Contemporary Polymer Chemistry*, 3rd Edition, **2003**.

[32] A. Napoli, H. Bermudez and J. A. Hubbell, *Langmuir* **2005**, 21, 9149.

[33] Z. Chen, J. A. Kornfield, S. D. Smith, J. T. Grothaus and M. M. Satkowsi, *Science* **1997**, 277, 1248.

[34] J. A. Opsteen, J. Cornelisssen and J. C.M. van Hest, *Pure Applied Chemistry* **2004**, 76, 1309.

[35] A. Choucair and A. Eisenberg, *Journal of American Chemical Society* **2003**, 39, 11993.

[36] A. Choucair and A. Eisenberg, *European Physical Journal E* **2003**, 10, 37.

[37] I. C. Reynhout, J. J.L. M. Cornelisssen and R. J. M. Nolte, *Journal of the American Chemical Society* **2007**, 129, 2327.

[38] W. Loh, *Encyclopedia of Surface and Colloid Science*, **2002**, 802.

[39] K. J. Hanley and T. P. Lodge, *Macromolecules* **2000**, 33, 5918.

[40] S. Förster, M. Zisenis, E. Wenz and M. Antonietti, *Journal of Chemical Physics* **1996**, 104, 9956

[41] Z. Tuzar and P. Kratochvil, *Advances in Colloid Interface Science* **1976**, 6, 201.

[42] K. Yu and A. Eisenberg, *Macromolecules* **1996**, 29, 6359.

[43] Y. Jiang, T. Chen, F. Ye, H. Liang and A.-C. Shi, *Macromolecules* **2005**, 38, 6710.

[44] S. Förster and T. Plantenberg, *Angewandte Chemie International Edition* **2002**, 41, 688.

[45] X. Cao, G. Xu, Y. Li and Z. Zhang, *Journal of Physical Chemistry A* **2005**, 109, 10418.

[46] C.-Y. Lee, *NNIN REU Research Accomplishments* **2005**, 72.

[47] G. Riess, *Progress in Polymer Science* **2003**, 28, 1107.

[48] I. C. Riegel, D. Samios, C. L. Petholdz, A. Eisenberg, *Polymer* **2003**, 44, 2117.

[49] Y. He, Z. Li, P. Simone and T. P. Lodge, *Journal of the American Chemical Society* **2006**, 128, 2745.

[50] W. Zhang, L.Shi, Y. An, L. Gao, K. Wu, R. Ma, *Macromolecules* **2004**, 37, 2551.

[51] S. Glotzer, M. Horsch, C. R. Iacovella, Z. Zhang, E. Chan, X. Zhang, *Current Opinions in Colloid & Interface Science* **2005**, 10, 287.

[52] K. Matyjaszewski, M. Wei, J. Xia, N. E. McDermott, *Macromolecules* **1997**, 30, 8161.

[53] B. Chu, *Langmuir* **1995**, 11, 414.

[54] A.B.R. Mayer, J.E. Mark, *Polymer Communication*, **2000**, 1627.

[55] E. S. Tillman, N. D. Contrella, J. G. Leasure, *Journal of Chemical Education* **2009**, 86, 1424.

[56] Y. Guillaneuf, D. Gignes, S. R. A. Marque, P. Tordo, D. Bertin, *Macromolecular Chemistry and Physics* **2006**, 207, 1278.

[57] A. A. Akbar, M. Abbasian, *Iranian Polymer Journal* **2006**, 15, 583.

[58] C. J. Hawker, A. W. Bosman, E. Harth, *Chemical Reviews* **2001**, 101, 3661.

[59] J. Pyun, K. Matyjaszewski, *Chemistry of Materials* **2001**, 13, 3436.

[60] K. Matyjaszewski, S. M. Jo, H.-J. Paik, S. G. Gaynor, *Macromolecules* **1997**, 30, 6398.

[61] T. E. Patten, K. Matyjaszewski, *Advanced Materials* **1998**, 10, 901.

[62] D. A. Shipp, J.-L. Wang, K. Matyjaszewski, *Macromolecules* **1998**, 31, 8005.

[63] V. Lima, X. Jiang, J. Brokken-Zijp, P. J. Schoenmakers, B. Klumperman, R. Van der Linde, *Journal of Polymer Science Part A: Polymer Chemistry* **2005**, 43, 959.

[64] M. F. Cunningham, *Progress in Polymer Science* **2002**, 27, 1039

[65] S. Kanagasabapathy, A. Sudalai, B. C. Benicewicz, *Macromolecular Rapid Communications* **2001**, 22, 1076.

[66] R. T.A. Mayadunne, E. Rizzardo, J. Chiefari, J. Kristina, G. Moad, A. Postma, S. T. Thang, *Macromolecules* **2000**, 33, 243.

[67] G. Moad, R. T.A. Mayadunne, E. Rizzardo, M. Skidmore, S. T. Thang, *Macromolecular Symposium* **2003**, 192, 1.

[68] J. Chiefari, Y.K. Chong, F. Ercole, J. Kristina, J. Jeffery, Tam P.T. Le, R. T.A. Mayadunne, G. F. Meijis, C. L. Moad, G. Moad, E. Rizzardo, S. T. Thang, *Macromolecules* **1998**, 31, 5559.

[69] C. Barner-Kowollik, M. Bubavk, B. Charleux, M. L. Coote, M. Drache, T. Fukuda, A. Goto, B. Klumperman, A. B. Lowe, J. B. Mcleary, G. Moad, M. J. Monteiro, R. D. Sanderson, M. P. Tonge, P. Vana, *Journal of Polymer Science Part A: Polymer Chemistry* **2006**, 44, 5809.

[70] J. F. Quinn, L. Barner, C. Barner-Kowollik, E. Rizzardo and T. P. Davis, *Macromolecules* **2002**, 35, 7620.

[71] R. B. Zetterlund, K. Miyake, K. Goto, B. Yamada, *Journal of Polymer Science Part A: Polymer Chemistry* **2004**, 42, 2640

[72] (a) M. Stenzel-Rosenbaum, T. P. Davis, V. Chen and A. G. Fane, *Journal of Polymer Science: Part A: Polymer Chemistry* **2001**, 39, 2777. (b) G.Zheng andC. Pan, *Polymer* **2005**, 46, 2802.

[73] (a) J.-F. Lutz, N. Jahed, K. Matyjaszewski, *Journal of Polymer Science: Part A: Polymer Chemistry* **2004**, 42, 1939. (b) M. A. Pinto, R. Li, C. D. Immanuel, P. A. Lovell, F. J. Schork, *Journal of American Chemical Society* . (c) C.-D. Vo, J. Rosselgong, S. P. Armes and N. C. Billingham, *Macromolecules* **2007,** *40*, 7119.

[74] (a) T. C. Krasia, C.S. Patrickios, *Macromolecules* **2006**, 39, 2467. b) M. Achilleos, T. C. Krasia, C.S. Patrickios, *Macromolecules* **2007**, 40, 5575.

[75] R. T. A. Mayadunne, E. Rizzardo, J. Chiefari, Y. Kwong Chong, G. Moad and S. H. Thang, *Macromolecules* **1999**, 32, 6977.

[76] S. Perrier, C.Barner-Kowollik, J.F. Quinn, P.Vana and T. P. Davis, *Macromolecules* **2002**, 35, 8300.

[77] S. Kanagasabapathy, A.Sudalai, B. C. Benicewicz, Macromol. *Rapid Communications* **2001**, 22, 1076.

[78] N. Gaillard, A. Guyot and J.Claverie, *Journal of Polymer Science: Part A: Polymer Chemistry* **2003**, 41, 684.

[79] Y. Luo, X. Liu, *Journal of Polymer Science: Part A: Polymer Chemistry* **2004**, 42, 6248.

[80] T. Krasia, R. Soula, H. G. Börner, H. Schlaad, *Chemimal Communications* **2003**, 4, 538.

[81] J. M. Campelo, D. Luna, R. Luque, J. M. Marinas and A. Romero, *ChemSusChem*, **2009**, 2, 18.

[82] A. Meristoudi, S. Pispas, N. Vainos, *Journal of Polymer Science: Part B: Polymer Physics*, **2008**, 46, 1515.

[83] M. Antonietti, E. Wenz, L. Bronstein and M. Seregina, *Advanced Materials* **1995**, 7, 1000.

[84] S. Klingelhofer, W. Heitz, A. Greiner, S. Oestreich, S. Förster and M. Antonietti, *Journal of the American Chemical Society* **1997**, 10116.

[85] S. Sidorov, L. Bronstein, P. Valetsky, J. Hartmann, H. Colfen, H. Schnablegger and M. Antonietti, *Journal of Colloid and Interface Science* **1999**, 212, 197.

[86] M. M. Demir, M. A. Gulgun, and Y. Z. Menceloglu, B. Erman, S. S. Abramchuk, E. E. Makhaeva, A. R. Khokhlov, V. G. Matveeva and M. G. Sulman, *Macromolecules*, **2004,** *37*, 1787.

[87] J. E. Munoz, J.Cervantes, R. Esparza, G. Rosas, *Journal of Nanoparticles Research*, **2007**, 9, 945.

[88] R. Reisfeld, T. Saraidarov, V. Levchenko, *Optica Applicata* **2008**, 38, 83.

[89] K. Siskova, J.´ Pfleger, M. Prochazka, *Applied Surface Science* **2009**, 256, 2979.

[90] (a) A. Fukuoka, A. Sato, K.-Y. Kodama, M. Hirano, S. Komiya, *Inorganic Chimica Acta* **1999**, 294, 266. (b) M. G. Guzmαn, J. Dille, S. Godet, *World Academy of Science, Engineering and Technology* **2008**, 43, 357. (c) P.-C. Lee, D. O. Kim, T.-H. Han, S.-J. Kang, L. S. Pu and J.-D. Nam, *Macromolecular Research* **2009**, 17, 187. (d) S. Panigrahi, S. Kundu, S. K. Ghosh, S. Nath and T. Pal, *Journal of Nanoparticle Research* **2004**, 6, 411.

[91] (a) D. Wostek-Wojciechowska, J. K. Jeszka, C. Amiens, B. Chaudret, P. Lecante, *Journal of Colloid and Interface Science* **2005**, 287, 107. (b) M.A. Dominguez-Crespo, E. Ramirez-Meneses, V. Montiel-Palma, A.M. Torres Huerta, V. Montiel-Palma, H. Dorantes Rosales, *International Journal of Hydrogen Energy* **2009**, 34, 1664.

[92] M. Harada, K. Saijo, N. Sakamoto, *Colloids and Surfaces A: Physicochemical and Engineering Aspects* **2009**, 349, 176.

[93] J. Zhang, Y. Gao, R. A. Alvarez-Puebla, J. M. Buriak, H. Fenniri, *Advanced Materials*, **2006** 18, 3233.

[94] C.E. Allmond, A.T. Sellinger, K. Gogick, J.M. Fitz-Gerald, *Applied Physics A: Materials Science & Processing*, **2007**, 86, 477.

[95] L. N. Nikitin, A. Yu. Vasilkov, A. R. Khokhlov, V. M. Bouznik, *Doklady Physical Chemistry*, **2008**, 422, 256.

[96] A. Y. Baranchikov, V. K. Ivanov, Y. D Tretyakov, Russian Chemical Reviews **2007**, 76, 133.

[97] (a) L. D. Pachon, G. Rothenberg, *Applied Organometallic Chemistry* **2008**, 22, 288. (b) A. Roucoux, *Topics In Organometallic Chemistry, Surface and Interfacial Organometallic Chemistry and Catalysis* **2005**, 16, 261.

[98] I. Haas, A. Gedanken, *The Royal Society of Chemistry* **2008**, 1795.

[99] S. Nath, S. Jana, M. Pradhan, T. Pal, *Journal of Colloid and Interface Science* **2010**, 341, 333.

[100] M. Seregina, L. Bronstein, O. A. Platonova, D. M. Chernyshov, P.M. Valetsky, J. Hartmann, E. Wenz, and M. Antonietti, *Chemistry of Materials* **1997**, *9*, 923.

[101] W. Li, Q.X. Jia, H.-L. Wang, *Polymer Communication* **2006**, 47, 23.

[102] A.B.R. Mayer, J.E. Mark, *Polymer Comminication* **2000**, 1627.

[103] I. W. Hamley, *AngewandteChemie* **2003**, 42, 1692.

[104] (a) D. Astruc, *Nanoparticles and Catalysis*, Wiley, **2008**. (b) R. B. Grubbs, *Polymer Reviews* **2007**, 47, 197.

[105] S. Papp, R. Patakfalvi, I. Dékány, *Croatica Chemica Acta* **2007**, 80, 493.

[106] A.B.R. Mayer, *Polymer for Advamced Technologies* **2001**, 12, 96.

[107] K.H.J. Buschow, R. Cahn, B. Ilschner ,E. Kramer, S. Mahajan, P. Veyssiere, *Encyclopedia of Materials: Science and Technology*, Elsevier, **2001**.

[108] K.J. Watson, J. Zhu, S. T. Nguyen, C. A. Mirkin, *Pure and Applied Chemistry* **2000**, 72, 67.

[109] R. B. Grubbs, *Journal of Polymer Science: Part A: Polymer Chemistry* **2005**, 43, 4323.

[110] A. B. R. Mayer, J. E. Mark, *Colloid Polymer Science* **1997**, 275, 333.

[111] L. M. Bronstein, D. M. Chernyshov, I. O. Volkov, M. G. Ezernitskaya, P. M. Valetsky, V.G. Matveeva, E. M. Sulman, *Journal of Catalysis* **2000**, 196, 302.

[112] (a) P. Papaphilippou, L. Loizou, N. C. Popa, A. Han, L. Vekas, A. Odysseos, T. Krasia-Christoforou, *Biomacromolecules* **2009**, 10, 2662. (b) M. E. Gindy, A. Z. Panagiotopoulos, R. K. Prud'homme, *Langmuir* **2008**, 24, 83.

[113] M. Arruebo, R. Fernández-Pacheco, M. R. Ibarra, J. Santamaría, *Nanotoday* **2007**, 2, 22.

[114] N. Nasongkla, E. Bey, J. Ren, H.Ai, C. Khemtong, J. S. Guthi, S.-F. Chin, A. D. Sherry, D. A. Boothman, J. Gao, *Nano Letters* **2006**, 6, 2427.

[115] D. Kim, *Journal of American Chemistry Society* **2007**, 129, 7661.

[116] J. H. Park,Y.T. Lim, O. Park, J. K. Kim, J. W.Yu, Y. C. Kim, *Chemistry of Materials* **2004,** *16*, 688.

[117] W. J. E. Beek, M. M. Wienk, R. A. J. Janssen, *Advance Functional Materials* **2006**, 16, 1112.

[118] K. Iliopoulos, D. Athanasiou, A. Meristoudi, N. Vainos, S. Pispas, S. Couris, *Physica Status Solidi* **2008**, 205, 2635.

[119] K. Tsuchiya, S. Nagayasu, S. Okamoto, T. Hayakawa, T. Hihara, K. Yamamoto, I. Takumi, *Optics Express* **2008**, 16, 5362.

[120] Manual of Polymer Standards Service (PSS), SEC Equipment.

[121] T. Krasia, Ph.D. Thesis, University of Potsdam, **2003**.

[122] D. Buzatu, O. Annunziattaa, E. Petrescub, C. Popac, F. D. Buzatud, *Journal of Optoelectronics and Advanced Materials* **2005**, 7, 3161.

[123] J. Holoubek, Journal of Quantitative Spectroscopy & Radiative Transfer **2007**, 106, 104.

[124] Organic Chemistry (7th International Edition), J. McMurry, Brooks/Cole Publishing Company, **2007**.

[125] (a) *«Σύγχρονες μέθοδοι στη χημική ανάλυση», Pecsok, Shields, Cairns, McWilliam, Δεύτερη έκδοση.*

(b) www.oswego.edu/~kadima/.../**FLUORESCENCE_SPECTROSCOPY**_08.pdf

[126] "*Characterization techniques of materials"*, MMK 554, Dr. Theodora Kyratsi, 2008.

[127] "*Characterization methods of polymers and colloids*", MMK 551, Dr. Theodora Krasia-Christoforou.

[128] "*Differential Scanning Calorimetry"*, H. K. D. H. Bhadeshia, University of Cambridge, Materials Science and Metallurgy.

[129] B. Ruozi, G. Tosi, E. Leo, M. A. Vandelli, *Talanta* **2007**, 73, 12.

[130] H. N. Pishkenari, N. Jalili, A. Meghdari, *Mechatronics* **2006**, 16, 655.

[131] K. Oikawa, H. Kimb, N. Watanabe, M. Shigeno, Y. Shirakawabe, K. Yasuda, *Ultramicroscopy* **2007**, 107, 1061.

[132] I. Janossy, T. I. Kosa, *Physical Review E* **2004**, 70, 052701.

[133] Y. Song, B. Bhushan, *Ultramicroscopy* **2007**, 107, 1095.

[134] "*Transmission Electron Microscopy and Diffractometry of Materials*", B. Fultz, J. M. Howe, Springer, **2007**.

[135] H. H. Huang, F. Q. Yan, Y. M. Kek, C. H. Chew, G. Q. Xu, W. Ji, P. S. Oh, S. H. Tang, *Langmuir* **1997**, 13, 172.

[136] A. J. Kiran, N. S. Rai, D. Udayakumar, K. Chandrasekharan, B. Kalluraya, R. Philip, H. D. Shashikala, A.V. Adhikari, *Materials Research Bulletin* **2008**, 43, 707.

[137] T. He, Y. Cheng, Y. Du, Y. Mo, *Optics Communications* **2007**, 275, 240.

[138] M. Sheik-Bahae, A. A. Said, T. H. Wei, D. J. Hagan, E. W. Van Stryland, *IEEE Journal of Quantum Electronics* **1990**, 26, 760.

[139] T. P. T. Le, G. Moad, E. Rizzardo, S. Thang, S. H. PCT. Int. Appl. WO 9801478 A1 980115, **1998**.

[140] (a) S. Ito, S. Ohmori and M. Yamamoto *Macromolecules* **1992**, 25, 185. (b) T. Krasia, C. S. Patrickios, *Polymer* 2002, 43, 2917. (c) F.-S. Du, Z.-C. LI, W. HONG, Q.-Y. GAO, F.-M. LI, *Journal of Polymer Science: Part A: Polymer Chemistry* **2000**, 38, 679.

[141] J. S. Hargreaves, S. E. Webber, *Macromolecules* **1984**, 17, 235.

[142] M. Demetriou, T. Krasia-Christoforou, *Journal of Polymer Science: Part A: Polymer Chemistry* **2008**, 46, 5442.

[143] S. S. Rogers, L. Mandelkern, *Journal of Physical Chemistry* **1957**, 61, 985.

[144] I. K. Varma, M. V. Nair, V. K. Karan, D. S. Varma, *Thermochimica Acta* **1989**, 142, 189.

[145] K. Iliopoulos, G. Chatzikyriakos, M. Demetriou, T. Krasia-Christoforou, S. Couris, *Optical Materials* **2011**, 33, 1342.

[146] A. Halperin, *Macromolecules* **1987**, 20, 2943.

[147] M. M. Dell' Anna, P. Mastrorilli, A. Rizzuti, G. P. Surana, C. F. Nobile, *Inorganica Chimica Acta* **2000**, 304, 21.

[148] L. M. Bronstein, S. N. Sidorov, A. Y. Gourkova, P. M. Valetsky, J. Hartmann, M. Breulmann, H. Gölfen, M. Antonietti, *Inorganica Chimica Acta* **1998**, 280, 348.

[149] R. Sigel, T. Krasia-Christoforou, I. Below, H. Schlaad, *Macromolecules* **2009**, 42, 4257.

[150] M. Demetriou, G. Chatzikyriakos, I. Papagiannouli, T. Krasia-Christoforou, S. Couris, **2011**, submitted.

[151] (a) R. Rutkaite, G. Buika, J. V. Grazulevicius, *Polymer Bulettin* **2001**, 46, 59, (b) R. Rutkaite, G. Buika, N. Kreiveniene, J.V. Grazulevicius, *Polymer Degradation and Stability* **2002**, 78, 143, (c) P. Zhao, Q.-D. Ling,W.-Z. Wang, J. Ru, S.-B. Li, W. Huang, *Journal of Polymer Science: Part A: Polymer Chemistry* **2007**, 45, 242.

[152] H. Zhao, E. P. Douglas, B. S. Harrison, and K. S. Schanze, *Langmuir* **2001,** *17*, 8428.

[153] M. Demetriou, T. Krasia-Christoforou, *Journal of Polymer Science: Part A: Polymer Chemistry* **2012,** *in press*.

[154] G. Moad, E. Rizzardo, S. H. Thang, *Australian Journal of Chemistry* **2005**, 58, 379.

[155] A. I. Buzin, M. Pyda, P. Costanzo, K. Matyjaszewski, B. Wunderlich, *Polymer* **2002**, *43*, 5563.

[156] U.S. Schubert, C. Eschbaumer, P. Andres, H. Hofmeier, C.H. Weidl, E. Herdtweck, E. Dulkeith, A. Morteani, N.E. Hecker, J. Feldmann,, *Synthetic Matals* **2001**, 121, 1249.

[157] D. Mohanta, A. Choudhury, *Optical Materials* **2006**, 29, 342.

[158] W. Nie, *Advanced Materials* **1993**, 5, 520.

[159] D. J. Wiliams, *Angewante Chemie International Edition* **1984**, 23, 690.

[160] C. Samyn, T. Verbiest, A. Persoons, *Macromolecular Rapid Communications* **2000**, 21, 1.

[161] S. Jacobson, P. Landi, T. Findakly, J. Stamatoff, H. Yoon, *Journal of Applied Polymer Science* **1994**, 53, 649.

[162] K. Illiopoulos, Ph.D. Thesis, University of Patras, **2009**.

[163] S. M. O'Flaherty, R.Murphy, S.V. Hold, M. Cadek, J. N. Coleman, W. J. Blau, *Journal of Physical Chemistry B* **2003**, 107, 958.

[164] L. W. Tutt, T. F. Boggess, *Progress in Quantum Electronic* **1993**, 17, 299.

[165] R. C. Hollins, *Current Opinion in Solid State and Materials Science* **1999**, 4, 189.

[166] K. I. Kelly, E. Coronado, L. L. Zhao, G. C. Schatz, *The Journal of Physical Chemistry B* **2003**, 107, 668.

[167] C. J. Murphy, T. K. Sau, A. M. Gole, C. J. Orendorff, J. Gao, L. Gou, S. E. Hunyadi, T. Li, *The Journal of Physical Chemistry B* **2005**, 109, 13857.

[168] R. L. Sutherland with contributions by D. G. McLean and S. Kirkpatrick, Handbook of nonlinear optics **2003** (2nd edition, New York, NY: Marcel Dekker).

[169] (a) A. W. Fahmi, H.-G. Braun, M. Stamm, *Advanced Materials* **2003**, 15, 1201. (b) S.-W. Chang, V. P. Chuang, S. T. Boles, C. A. Ross, C. T. Thompson, *Advanced Functional Materials* **2009**, 19, 2495.

[170] H. J. Fan, P. Werner, M. Zacharias, *Small* **2006**, 2, 700.

[171] T. Thurn-Albrecht, J. Schotter, G. A. Kästle, N. Emley, T. Shibauchi, L. Krusin-Elbaum, K. Guarini, C. T. Black, M. T. Tuominen, T. P. Russell, *Science* **2000**, 290, 2126.

[172] E. J. W. Crossland, S. Ludwigs, M. A. Hillmyer, U. Steiner, *Soft Matter* **2007**, 3, 94.

[173] J. Peng, C. Mao, J. Kim, D. H. Kim, *Macromolecular Rapid Communication* **2009**, *30*, 1857.

[174] R. Shenhar, T. B. Norsten, V. M. Rotello, *Advanced Materials* **2005**, *17*, 657.

[175] J. Q. Lu, S. S. Yi, *Langmuir* **2006**, 22, 3951.

[176] W. Hwang, J.-H.Choi, T. H. Kim, J. Sung, J.-M. Myoung, D.-G. Choi, B.-H. Sohn, S. S. Lee, D. H. Kim, C. Park, *Chemistry of Materials* **2008,** *20*, 6041–6047.

[177] M. Zervos, M. Demetriou, T. Krasia-Christoforou, A. Othonos, R. P. Turcu, *RSC Advances* **2011**, submitted.

[178] (a) M.-Q. Zhu, L.-Q. Wang, G. J. Exarhos, A. D. Q. Li, *Journal of the American Chemical Society* **2004**, 126, 2656. (b) F. Toderas, M. Baia, D. Maniu, S. Astilean, *Journal of Optoelectronics and Advanced Materials* **2008**, 10, 2282.

[179] J.-M. Kim, T.-E. Chang, D. K. Han, K.-D. Ahn, *Journal of Photopolymer Science and Technology* **2000**, *13*, 273.

[180] (a) R. Corradini, C. Paganuzzi, R. Marchelli, S. Pagliari, A. Dossena, A. Duchateau, *Journal of Inclusion Phenomena and Macrocyclic Chemistry* **2007**, *57*, 625. (b) J. H. Chang, Y. Jeong, Y.-K. Shin, *Bulletin of the Korean Chemistry Society* **2003**, *24*, 119. (c) M. A. Clark, K. Duffy, J. Tibrewala, S. J. Lippard, *Organic Letters* **2003**, *5*, 2051.

[181] (a) C.Yanga, T. S. Lee, *Molecular Crystals and Liquid Crystals* **2000**, 349, 283. (b) Z. Chen, C. Xue, W. Shi, F.-T. Luo, S. Green, J. Chen, H. Liu, *Analytical Chemistry* **2004**, *76*, 6513. (c) H.-W. Wang, Y.-J. Cheng, C.-H. Chen, T.-S. Lim, W. Fann, C.-L. Lin, Y.-P Chang, K.-C. Lin, T.-Y. Luh, *Macromolecules* **2007**, 40, 2666. (d) S. W. Thomas III, G. D. Joly, T. M. Swager, *Chemical Reviews* **2007,** 107, 1339.

[182] E. C. Buruiana, M. Olaru, B. C. Simionescu, *European Polymer Journal* **2007**, *43*, 1359.

[183] L. Miao, X. Liu, Q. Fan, W. Huang, ***Progress in Chemistry*** **2010**, ***22***, **2338.**

[184] H. Weizman, O. Ardon, B. Mester, J. Libman, O. Oren Dwir, Y. Hadar, Y. Chen, A. Shanzer, *Journal of American Chemical Society* **1996**, 118, 12368.

[185] (a) L. Prodi, F. Bolletta, M. Montalti, N. Zaccheroni, *Coordination Chemistry Reviews* **2000**, 205, 59. (b) B. Wang, M.R. J. Wasielewski, *American Chemical Society* **1997**, 119, 12.